NANYANG TECHNOLOGICAL UNIVERSITY

SYNTHESIS, CRYSTAL STRUCTURES AND OPTICAL PROPERTIES OF RARE EARTH SILICATE OXYAPATITE

SHEN YIQIANG

SCHOOL OF MATERIALS SCIENCE AND ENGINEERING

2012

SYNTHESIS, CRYSTAL STRUCTURES AND OPTICAL PROPERTIES OF RARE EARTH SILICATE OXYAPATITE

SHEN YIQIANG

School of Materials Science and Engineering

A thesis submitted to the Nanyang Technological University in partial fulfillment of the requirement for the degree of Doctor of Philosophy

2012

Acknowledgements

First of all, I would like to thank my supervisor Prof. Dong Zhili for his guidance on the research directs and his patience and encouragement. Thanks to Prof. Boey, Prof. Ma and Prof. Subbu for creating such a good research environment in our school. Thanks to Prof. Alfred Tok, Prof. Tang Dingyuan and Prof. Sun Handong for valuable suggestions. Also Thanks to my TAC members Prof. Gan Chee Lip and Prof. Alex Yan for their instructions on my thesis.

I want to express my gratitude to Dr. Zhang Jian and Dr. Zhang Tianshu for their precious and constructive advices on my research works. Also I am very grateful to have good friends like Song Xiaochao, Lu Jie, Sun Ting, Yang Kai and Chen Rui *etc.* who are all research students here. Moreover, thanks to all the technicians in FACTS, inorganic and organic service labs for their good managements of the labs and equipments.

Last but not least, I want to thank my parents for their endless love that I will remember forever.

Abstract

The silicate oxyapatite materials are known for their structural flexibilities, high melting temperatures and good chemical stabilities. Therefore, various applications for this group of materials have been explored. In the present work, synthesis methods, crystal structures and the optical properties including potential optical applications of silicate oxyapatite $Sr_2Y_8(SiO_4)_6O_2$ based materials are studied.

Pure $Sr_2Y_8(SiO_4)_6O_2$ powders are synthesized by both solid state reaction and sol-gel method. The crystal structure characterizations of $Sr_2Y_8(SiO_4)_6O_2$ show that its symmetry belongs to $P6_3/m$. The general formula of silicate oxyapatite materials is $A^I_4A^{II}_6(SiO_4)_6O_2$ and in the current case, half of A^I sites are occupied by Sr^{2+} while the other half of A^I sites and all the A^{II} sites are filled by Y^{3+}.

The crystal structures and the photoluminescent properties of Eu^{3+} doped $Sr_2Y_8(SiO_4)_6O_2$ with different Eu^{3+} concentrations are investigated. The XRD and Rietveld refinement revealed that most Eu^{3+} cations entered A^I sites in low europium concentration ($x = 0\sim0.5$). At increased Eu^{3+} concentration ($x > 0.5$), Eu^{3+} cations also occupy A^{II} sites but the preference to the A^I sites still maintained. Photoluminescent properties vary with Eu^{3+} concentrations according to photoluminescent spectra. $Sr_2Y_6Eu_2(SiO_4)_6O_2$ from sol-gel method appears to be the one with the strongest emission in nearly pure red color, whose intensity is comparable to commercial fluorescent lamp phosphor $Eu:Y_2O_3$, demonstrating potential as a red phosphor for the white LEDs.

The translucent silicate oxyapatite $Sr_2Y_8(SiO_4)_6O_2$ ceramic with a low porosity of about 0.7% is successfully fabricated by employing the spark plasma sintering. The total forward transmittance is about 52% but the in-line transmittance is much lower. Calculation reveals that influence of residual pores on the in-line transmittance is more significant than that of the birefringence effect.

Though previous studies of translucent ceramics fabricated by spark plasma sintering with luminescent properties are limited, the translucent Ce^{3+} doped $Sr_2Y_8(SiO_4)_6O_2$ ceramics with different Ce^{3+} concentration are fabricated by spark plasma sintering in this work and their photoluminescent properties are studied. The energy transfer process between Ce^{3+} cations at A^I and A^{II} is revealed.

TABLE OF CONTENTS

Chapter 1 Introduction

1.1 Background

As a subgroup of apatite materials, the series of silicate oxyapatite materials usually adopt $P6_3/m$ symmetry with the general formula $A^I{}_4A^{II}{}_6(SiO_4)_6O_2$, where A^I and A^{II} are two cationic sites with Wycoff symbol 4f and 6h respectively. This series of materials is known for its structural flexibility, the high melting point and the good chemical stability.[1,2] Therefore, various of applications for silicate oxyapatite materials have been explored.

Beside the application as the electrolyte in the solid state fuel cell, the silicate oxyapatites also have great potential in luminescent applications. The red emissions of Eu^{3+} doped silicate oxyapatites were first reported by Isaacs in 1973,[3] whose work suggested the silicate oxyapatites could be a host lattice for the luminescent materials such as phosphors. Due to the complicated crystal structures, many studies were followed to discuss the relationship between activator dopants such as rare earth cations and the crystal structure. Blasse investigated the luminescent properties of several Eu^{3+} doped silicate oxyapatites and studied the occupancy preference between A^I and A^{II} sites,[4] and the author concluded that the A^{II} site tends to accommodate cations with higher charge and/or smaller radius to compensate the local charge. Lin and Su found that Eu^{3+} occupied two cationic sites simultaneously after analyzing high resolution photoluminescence spectra of three silicate oxyapatites, $MY_8(SiO_4)_6O_2:Eu^{3+}$ (M = Mg, Ca, Sr). This phenomenon was attributed to the compromise of the size effect proposed by Felsche[5] and the charge compensation effect proposed by Blasse.[6] However, all these studies were only focused on the spectral analysis and did not use other materials characterization techniques such as X-ray diffraction and Rietveld refinement. For industrial applications, one silicate oxyapatite $Ba_2La_8(SiO_2)_6O_2$ doped with Eu^{2+} and

Mn^{2+} was patented as a yellow-green phosphor for the use in fluorescent lamps with an effective excitation at 254 nm.[7] Moreover, Tb^{3+} doped $Sr_2Gd_8(SiO_4)_6O_2$ was proposed to be a potential candidate of green phosphor for the plasma display panels (PDP) due to its excitation at vacuum ultraviolet region.[8] However, the utilization of the red emission from Eu^{3+} doped silicate oxyapatites as practical phosphor is limited. Also very few studies explore the applications of silicate oxyapatite materials in the white LED, which emerges as a hot topic for new generation of lighting.[9] Other than application in phosphors, silicate oxyapatites are also applied to other luminescent-related field such as scintillators and lasers. Silicate oxyapatites $Ln_{9.33}(SiO_4)_6O_2$ (Ln = Gd, Yb, La and Lu) doped with Ce^{3+} alone or co-doped with Tb^{3+} were patented as scintillators for X-ray and gamma ray by Francois *et al.*[10] Steinbruegge *et al.* [2] tested various silicate oxyapatite single crystals and suggested that these materials could be excellent laser hosts for Nd^{3+} and Ho^{3+}. Druon *et al.* [11, 12] fabricated Yb^{3+} doped $Sr_2Y_8(SiO_4)_6O_2$ transparent single crystals to generates ultrashort laser with a 94-femtosecond pulse duration.

Both the scintillators and laser media requires the light transmittance of the materials and silicate oxyapatites have been fabricated in a single crystalline form as reported in previous studies. As the single crystal growth process is costly and time consuming, the transparent or translucent ceramic has emerged as an alternative with lower cost, more time-efficiency and other merits.[13, 14] The major challenge in the process of fabricating transparent ceramics is to minimize the light scattering centers, mainly due to residual pores and birefringence effect.[15] In fact, it is difficult to fabricate the materials with non-cubic structures into highly transparent ceramics because the birefringence effect derived from the anisotropic optical properties is intrinsic and inevitable. Therefore, ceramic forms of non-cubic structured materials are seldom used as laser media which require high transparency. However, the transparency requirement for scintillators is less rigid and translucent ceramic form of $Lu_2SiO_5:Ce^{3+}$ (LSO:Ce) with a monoclinic symmetry

was fabricated and tested for both X-ray and gamma ray.[16, 17] The light yields of polycrystalline LSO:Ce in both X-ray and gamma ray tests were comparable to these of LSO:Ce single crystals, demonstrating the potential of the transparent/translucent ceramics applied as scintillators.

1.2 Objectives and hypothesis

The objectives of this thesis are to study the relationship between the crystal structure of silicate oxyapatite $Sr_2Y_8(SiO_4)_6O_2$ and the luminescent properties after rare earth doping and furthermore, explore the potential of this material in applications of phosphors and scintillators.

The electronic structures of free rare-earth cations are constant and have been thoroughly studied in physics. However, the electronic structures of rare earth cations would deviate from those in free states when rare earth cations are accommodated in some host lattices. The interpretation of the relationship between the host lattice and the electronic structures of rare earth cations is an interesting topic and would enrich the research in material science. The photoluminescent properties of rare earth doped materials can reflect the features of crystal structures, so most of previous studies about the relationship between the silicate oxyapatite crystal structure and the photoluminescent properties focus on the interpretation of the photoluminescence spectra first and then predicting the crystal structure. In fact, it is more convincible to resolve the crystal structure which is the origin of the photoluminescent properties at the first place by X-ray diffraction, Rietveld refinement and electron microscope, and then analyze the photoluminescent properties based on the crystal structures. Therefore, in the current study, pure $Sr_2Y_8(SiO_4)_6O_2$ is synthesized and the crystal structure is determined by the characterization tools at first. After that, the crystal structures of rare earth Eu^{3+} doped $Sr_2Y_8(SiO_4)_6O_2$ are analyzed by considering the pure $Sr_2Y_8(SiO_4)_6O_2$ as the initial

structural model. Later, the photoluminescence spectra of Eu^{3+} doped $Sr_2Y_8(SiO_4)_6O_2$ are analyzed based on the crystal structure results.

Various Eu^{3+} doped molybdates and tungstates materials have been investigated as a promising red phosphor in white LED due to the high emission with excitation of Eu^{3+} 4*f* levels at near UV region and its good chemical stability.[18-22] However, very few studies on Eu^{3+} doped silicate oxyapatite as a white LED phosphor material have been reported. Since previous studies has shown that Eu^{3+} doped silicate oxyapatites can generate red emission[3] as displayed in the photoluminescence spectra, and moreover, two cationic sites for Eu^{3+} exhibits different photoluminescence properties,[4] it is likely that the photoluminescent properties of this materials group can be tuned to be suitable for white LED application through varying the cation site occupancies. This project will cover the investigation of relationships between apatite crystal structure with different cation site occupancies and the photoluminescent properties, and exploration of potential applications of Eu^{3+} doped silicate oxyapatite as a red phosphor in white LED.

The acceptable light transmittance is prerequisite for the application of scintillator. Since translucent ceramic form of $Lu_2SiO_5:Ce^{3+}$ (LSO:Ce) with a non-cubic symmetry was investigated and demonstrated the feasibility as a scintillator,[16, 17] it is also possible to produce translucent ceramics of silicate oxyapatite $Sr_2Y_8(SiO_4)_6O_2$ by suppressing the porosity and the pore size. In order to understand the light scattering effects by pores and birefringence more specifically, Mie theory will be employed to analyze the transmittance. After obtaining the translucent ceramic of $Sr_2Y_8(SiO_4)_6O_2$, Ce^{3+} cation will be used as the activator, the same as in LSO:Ce, and Ce^{3+} doped translucent $Sr_2Y_8(SiO_4)_6O_2$ ceramics will be fabricated. As one of three important processes in the scintillation, the photoluminescent process in these ceramics will be studied.

1.3 Scope

There are seven chapters in this thesis with this introduction as chapter 1.

Chapter 2 is a brief literature review. First, the silicate oxyapatite structures are generally described and the synthesis methods of silicate oxyapatite materials are summarized. Then, the general mechanism of luminescence and its applications is discussed, followed by presenting the silicate oxyapatites' applications in luminescence-related fields. Finally, the developments of transparent ceramics as well as the processing methods are introduced.

Chapter 3 focuses on synthesis of pure $Sr_2Y_8(SiO_4)_6O_2$ by modified solid state reaction and sol-gel methods. The crystal structure of the as-obtained pure powders is characterized by X-ray diffraction, Rietveld refinement and high resolution transmission electron microscopy. Moreover, a systematic study of the reported silicate oxyapatite materials is conducted to interpret the structural evolution. A new term of effective ionic radius is introduced and its relationships with lattice constants and twist angles are analyzed.

Chapter 4 analyzes the crystal structures of $Sr_2Y_8(SiO_4)_6O_2$ and the photoluminescent properties with different Eu^{3+} doping concentrations. Moreover, Eu^{3+} doped samples synthesized by solid state reaction and sol-gel method are compared. The color purity and the intensity of the red emission of Eu^{3+} doped $Sr_2Y_8(SiO_4)_6O_2$ is explored for the potential application in white LEDs.

Chapter 5 demonstrates the process of fabricating translucent ceramic of $Sr_2Y_8(SiO_4)_6O_2$ by spark plasma sintering from the powders obtained from solid state reaction. The ceramics with complete and incomplete condensation are fabricated, and their microstructures and transmittances are investigated. The Mie scattering theory is used to analyze the influence of the pore and birefringence on the light transmittance.

Chapter 6 investigates the photoluminescent properties of translucent ceramics of Ce^{3+} doped $Sr_2Y_8(SiO_4)_6O_2$, which is crucial for the understanding of scintillators properties. Moreover, the energy transfer process between Ce^{3+} cations at different sites in the samples is revealed and studied by photoluminescence spectra and the decay profiles.

Chapter 7 is the conclusions and the suggestions for future research.

1.4 References

1. M. G. Zuev, A. M. Karpov & A. S. Shkvarin, (2010). Synthesis and Spectral Characteristics of $Sr_2Y_8(SiO_4)_6O_2$:Eu Polycrystals. *Journal of Solid State Chemistry*, 184 (1), 52-58.
2. K. B. Steinbruegge, T. Henningsen, R. H. Hopkins, R. Mazelsky, N. T. Melamed, E. P. Riedel & G. W. Roland, (1972). Laser Properties of Nd^{3+} and Ho^{+3} Doped Crystals with Apatite Structure. *Applied Optics*, 11 (5), 999-1012.
3. T. J. Isaacs, (1973). Study of Eu^{3+} Fluorescence in Some Silicate Oxyapatites. *Journal of the Electrochemical Society*, 120 (5), 654-656.
4. G. Blasse, (1975). Influence of Local Charge Compensation on Site Occupation and Luminescence of Apatites. *Journal of Solid State Chemistry*, 14 (2), 181-184.
5. J. Felsche, (1972). Rare-Earth Silicates with Apatite Structure. *Journal of Solid State Chemistry*, 5 (2), 266-275.
6. J. Lin & Q. Su, (1994). A Study of Site Occupation of Eu^{3+} in $ME_2Y_8(SiO_4)_6O_2$ (ME=Mg, Ca, Sr). *Materials Chemistry and Physics*, 38 (1), 98-101.
7. G. A. Sigai & M. N. Alexander, (1988). Yellow Green Barium Lanthanum Silicate Oxyapatite Phosphor, a Fluorescent Lamp Containing the Same, and a Method thereof. *US Patent,* 4748391.
8. A. Yamane, T. Kunimoto, K. Ohmi, T. Honma & H. Kobayashi, (2006). Luminescent Properties of Tb-activated Rare-Earth Oxyapatite Silicate $MLn_4Si_3O_{13}$ (M=Ca, Sr, Ln=La, Gd). *Physica Status Solidi C*, 3 (8), 2705-2708.
9. D. A. Steigerwald, J. C. Bhat, D. Collins, R. M. Fletcher, M. O. Holcomb, M. J. Ludowise, P. S. Martin & S. L. Rudaz, (2002). Illumination with Solid State Lighting Technology. *IEEE Journal of Selected Topics in Quantum Electronics*, 8 (2), 310-320.
10. B. Francois, M. Navizet, J. C. Rebreyend & C. Wyon, (1991). Monocrystals of Silicates of Lanthanides Usable as Scintillators for the Detection of X and Gamma Radiation. *US Paten,* 4988882.
11. F. Druon, F. Balembois & P. Georges, (2000). Generation of 90-fs Pulses From a Mode-locked Diode-pumped Yb^{3+}:$Ca_4GdO(BO_3)_3$ Laser. *Opictics Letters*, 25 (6), 423-435.
12. F. Druon, S. Chenais & F. Raybaut, (2002). Apatite-structure Crystal, Yb^{3+}:$SrY_4(SiO_4)_3O$, for the Development of Diode-pumped Femtosecond Lasers. *Optics Letters*, 27 (21), 1914-1916.
13. V. Lupei, A. Lupei & A. Ikesue, (2004). Single Crystal and Transparent Ceramic Nd-doped Oxide Laser Materials: a Comparative Spectroscopic Investigation. *Journal of Alloys and Compounds*, 380 (1-2), 61-70.
14. L. Mezeix & D. J. Green, (2006). Comparison of the Mechanical Properties of Single Crystal and Polycrystalline Yttrium Aluminum Garnet. *International Journal of Applied Ceramic Technology*, 3 (2), 166-176.
15. R. Apetz & M. P. B. van Bruggen, (2003). Transparent Alumina: A Light-Scattering Model. *Journal of the American Ceramic Society*, 86 (3), 480-486.
16. A. Lempicki, C. Brecher, H. Lingertat, S. R. Miller, J. Glodo & V. K. Sarin, (2008). A Ceramic Version of the LSO Scintillator. *IEEE Transactions on Nuclear Science*, 55 (3), 1148-1151.
17. D. J. Wisniewski, L. A. Boatner, J. S. Neal, G. E. Jellison, J. O. Ramey, A. North, M. Wisniewska, A. E. Payzant, J. Y. Howe, A. Lempicki, C. Brecher & J. Glodo, (2008). Development of Novel Polycrystalline Ceramic Scintillators. *IEEE Transactions on Nuclear Science*, 55 (3), 1501-1508.
18. Y. S. Hu, W. D. Zhuang, H. Q. Ye, D. H. Wang, S. S. Zhang & X. W. Huang, (2005). A Novel Red Phosphor for White Light Emitting Diodes. *Journal of Alloys and Compounds*, 390 (1-2), 226-229.

19. Y. C. Chang, C. H. Liang, S. A. Yan & Y. S. Chang, (2010). Synthesis and Photoluminescence Characteristics of High Color Purity and Brightness $Li_3Ba_2Gd_3(MoO_4)_8:Eu^{3+}$ Red Phosphors. *Journal of Physical chemistry C*, In press.
20. Z. Xu, C. Li, G. Li, R. Chai, C. Peng, D. Yang & J. Lin, (2010). Self-Assembled 3D Urchin-Like $NaY(MoO_4)_2:Eu^{3+}/Tb^{3}+$ Microarchitectures: Hydrothermal Synthesis and Tunable Emission Colors. *Journal of Physical chemistry C*, 114 (6), 2573-2582.
21. Z. L. Wang, H. B. Liang, L. Y. Zhou, H. Wu, M. L. Gong & Q. Su, (2005). Luminescence of $(Li_{0.333}Na_{0.334}K_{0.333})Eu(MoO_4)_2$ and Its Application in Near UV InGaN-Based Light-emitting Diode. *Chemical Physics Letters*, 412 (4-6), 313-316.
22. L. Zhou, L. G. Yi, R. F. Sun, F. Z. Gong & J. H. Sun, (2008). A Potential Red Phosphor $Na_{0.5}Gd_{0.5}MoO_4:Eu^{3+}$ For Light-Emitting Diode Application. *Journal of the American Ceramic Society*, 91 (10), 3416-3418.

Chapter 2 Literature Review

2.1. Apatite structures

2.1.1 General description of apatite structure

Apatite is a group of common minerals. The natural apatite minerals not only exist in the rocks[1] but also make up of our teeth and bones.[2, 3] One common example of an apatite is calcium phosphate, having groups like hydroxyapatite, fluorapatite and chlorapatite with the end-members $Ca_{10}(PO_4)_6OH_2$, $Ca_{10}(PO_4)_6F_2$ and $Ca_{10}(PO_4)_6Cl_2$ respectively. Due to its superior biocompatibility, apatite is synthesized and widely used in biomedical applications such as a coating to promote the bone growth and a filler to replace the amputated bone.[4] Moreover, the apatite structure is known for the large tolerance of the ionic substitutions. The calcium cation can be substituted by large trivalent (Y^{3+}, La^{3+} and Ce^{3+}, *etc.*), divalent (Ca^{2+}, Sr^{2+} and Pb^{2+}, *etc.*) or monovalent (Li^{+}, Na^{+} and K^{+}, *etc.*) cations, the phosphate cation can be replaced by highly charged small cations (As^{5+}, V^{5+} and Si^{4+}, *etc.*) and the ligand groups normally are halides, OH^{-} or O^{2-}.[5-7] The ion substitutions lead to numerous derivatives with apatite structure, combined with significant stability and durability. This feature of the compounds with apatite structure leads to great potential in the environmental remediation, for example, immobilization of harmful metals from the incinerators, nuclear wastes and the contaminated water and soils.[8-15] Due to the crystal structural complexity and the necessity to reveal the mechanisms of the apatite-structured compound in the biomedical and environmental applications, the variants of the apatite structure draw much attention in the field of crystal chemistry and crystallography. The crystal structural details and the evolution of the apatite-structured compounds have been intensively studied and the group of apatite is expanded to all the compounds with apatite structure rather than several natural apatite

minerals. The crystal structure of $Ca_{10}(PO_4)_6F_2$ was investigated and the symmetry was first determined to be $P6_3/m$ by Naray-Szabo.[16] Elliot covered a wide range of cation-substituted apatites and described their structures, including the ones with lower symmetries than $P6_3/m$.[17] The author also summarized the synthesis methods, crystal growth and various physical properties. Later, White and Dong [18] studied the structural derivation of apatite from two aspects. One is substituting the cation in aristotype Mn_5Si_3 and inserting anions, the other is hexagonal anion networks. The twist angle φ obtained from the crystal structures turns out to be an important parameter, since it varies linearly as a function of the average ionic radius. This research also indicates that the most of the apatite structures adopt $P6_3/m$ symmetry while some of them have lower symmetries such as $P6_3$ and $P\bar{3}$. The general formula of apatite with $P6_3/m$ symmetry is $A^I{}_4A^{II}{}_6(BO_4)_6X_2$, where A^I and A^{II} are two distinct crystallographic sites with Wycoff symbols 4f and 6h respectively.

2.1.2 Silicate oxyapatite

Silicate oxyapatites are known for its high melting point (~2000 ºC) and chemical stabilities above 1000 ºC.[19,20] Due to the unique crystal structure and high chemical stability, silicate oxyapatites were intensively studied and applied in the solid state fuel cell (SOFC) as alternatives to the traditional electrolyte yttria-stabilized zirconia (YSZ).[21-24] The silicate oxyapatite acts as an oxygen anion conductor with high electric conductivities and lower working temperatures, demonstrating the potential of application. Moreover, the silicate oxyapatite has prospect in the biomedical industries because it was patented recently as bone biomaterials with promising biocompatibility and the physical properties in the orthopedic surgeries.[25] Beside these two applications, rare earth doped silicate oxyapatites are attractive in optical investigations about lasers, phosphors and scintillators, which will be discussed in the next section.

All the properties of the silicate apatite are related to their crystal structures. For instance, the performance of the phosphors is determined by the energy levels of the doped rare earth elements and the atoms in the crystal structure will interact with rare earth atom and induce the difference from the energy levels at the free ion state.[26] The duration of the laser pulse in the solid state ultrafast laser system is influenced by the structural disorder in the way that the more disordered the structure is, the shorter laser pulse can be generated.[27] Hence, the crystal structure of the silicate apatite becomes an interesting topic and many research works have been done.[28-31]

The general formula is $A^{I}_4A^{II}_6(SiO_4)_6O_2$ with $P6_3/m$ symmetry. As shown in Figure 2-1, the structure consists of three types of cation-centered polyhedra: Si−O tetrahedra, A^{I}−O and A^{II}−O polyhedra. The Si−O tetrahedra, which are isolated from each other, act as important bridges to connect A^{I}−O and A^{II}−O polyhedra and construct the hexagonal channel along the *c* axis. In the A^{I}−O polyhedra, the central A^{I} site with a local symmetry of C_3 is coordinated with nine oxygen atoms, forming a tricapped trigonal-prismatic geometry. The twist angle φ is obtained from this polyhedron. The A^{II} site is coordinated by seven oxygen atoms and result in irregular polyhedra with pentagonal bipyramidal geometry. Each A^{II}−O polyhedron contains one interesting oxygen atom which is closely bonded to A^{II} atom and does not belong to any Si−O tetrahedron. Therefore, it is called free oxygen, marked as O4 with Wycoff symbol 2a, and many unique properties of apatite can be ascribed to it. Felsche [28] studied series of rare earth silicate oxyapatite compounds like $RE_{9.33}(SiO_4)_6O_2$, $LiRE_9(SiO_4)_6O_2$, $NaRE_9(SiO_4)_6O_2$ and $(Mg, Ca, Sr, Ba)_2RE(SiO_4)_6O_2$ (RE: La → Lu) and tried to explicit the structural evolution by focusing on the influence of the ionic radius of the rare earth elements on unit cell dimensions. The author suggested that the 6h (A^{II}) position in the apatite with $P6_3/m$ symmetry tends to accommodate smaller cations because of its smaller volume as compared to that of the 4f (A^{I}) position. Moreover, the study shows that lattice parameter *a* is more dependent on

the variation at the 6h (A^{II}) position since this position has more tight bonds in [*hk*0] directions. Masubuchi *et al.* [30] studied the crystal structure of $RE_{9.33}(SiO_4)_6O_2$ and $Sr_2RE_8(SiO_4)_6O_2$ (RE=La, Nd) by neutron powder diffraction and related the structural features, especially the anisotropic displacement parameters of the oxygen O4 in the channel, to the ionic conductive properties. The author found that the cation-deficient apatite enhanced the anisotropic displacement of O4 along the *c* axis, leading to a high ionic conductivity.

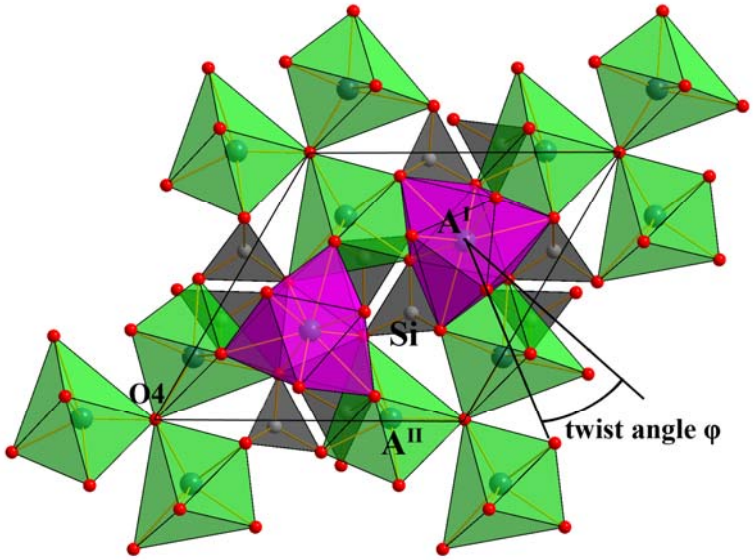

Figure 2-1 Crystal structure of silicate oxyapatite. The gray, pink and green polyhedra represent for Si−O tetrahedra, A^I−O and A^{II}−O polyhedra respectively. This structure is reproduced by using the crystal structure data of $NaY_9(SiO_4)_6O_2$ provided by Redhammer and Roth [31].

2.1.3 Synthesis method of silicate oxyapatite

Various synthesis methods of silicate oxyapatites have been reported so far. Yao *et al.* synthesized lanthanum silicate oxyapatite $La_{9.33}(SiO_4)_6O_2$ by precipitation method.[32] Since it is difficult to introduce silicon sources for precipitation, sodium silicate ($Na_2O{\cdot}nSiO_2$, $n \approx 3.2$) was used and modified by a cationic exchange resin to eliminate the sodium ion. And then the silicon source was mixed with $La(NO_3)_3$ solution

stoichiometrically and precipitated by $(NH_4)_2CO_3$. The precipitates were washed several times before drying and heating. Although the XRD results seem promising, it is difficult to guarantee the silicon source is still stoichiometric after washing because theoretically it cannot be precipitated by $(NH_4)_2CO_3$. Besides, it is easy to introduce impurities with the residual sodium species.

Hydrothermal synthesis as a common wet chemistry method was applied to synthesize silicate oxyapatite $KNd_9(SiO_4)_6O_2$ by Haile *et al.* [33] KOH, K_2CO_3 and $K_2B_4O_7$ were used as mineralizer and $4K_2O{-}Nd_2O_3{-}17SiO_2$ glass was the precursor in the reaction. It showed that high synthesis temperature, high pressure and long reaction time were favored to produce well crystallized $KNd_9(SiO_4)_6O_2$, typically a temperature of 500 °C, a pressure of 1400 bar and a duration of ten days. However, the low yield and the long reaction time limit the application of this hydrothermal method.

Most methods utilized to massively synthesize silicate oxyapatite without introducing foreign ions are solid state reaction and sol-gel method. Solid state reaction is the most common method used to synthesize oxides materials not only oxyapatites. Usually the reactant oxides are mixed first and then heated to certain temperature to form the desired phase according to the phase diagram. Repeated heating can also be performed to ensure the phase purity.

Sol-gel method is a way to obtain atomic-scaled homogeneity and widely used in synthesis of various oxides. Generally metal alkoxides are used in the synthesis and for the silicates like in our case, the silicon alkoxides play a crucial role in the sol-gel synthesis. When the silicon alkoxides dissolved in water, the hydrolysis process happens and the alkoxy group would be substituted by hydroxyl group as:

$$Si(OR)_4 + H_2O \rightarrow HO\text{-}Si(OR)_3 + ROH \qquad \text{Equation 2-1}$$

where $Si(OR)_4$ is the silicon alkoxide and R is the ligand such as alkyl. The substitution is not limited to one ligand group, so more generally

$Si(OR)_4 + nH_2O \rightarrow Si(OR)_{4-n}(OH)_n + nROH$ Equation 2-2

Subsequently, condensation process would occur between the hydrolyzed molecules, for example:

$(OR)_3Si\text{-}OH + HO\text{-}Si(OR)_3 \rightarrow (OR)_3Si\text{-}O\text{-}Si(OR)_3 + H_2O$ Equation 2-3

This condensation process continues and results in large molecules with polymerized network structure.[34, 35] In order to synthesize silicate oxyapatite, other metal cations to occupy the A^I and A^{II} sites are also needed. Generally metal salt are used as the metal sources.[36-40] The metal cations are seldom involved in the hydrolysis and condensation reactions and they are linked to the polymer networks by ion pairing as proposed by Sanchez and McCormick.[41] Celerier *et al.* have demonstrated a classic procedure to synthesize silicate oxyapatite with metal salts, lanthanum hexahydrate nitrate $La(NO_3)_3 \cdot 6H_2O$.[36] Lanthanum salt was mixed with appropriate water, ethanol and acetic acid. Acetic acid was the catalyst. When lanthanum salt is totally dissolved, stoichiometric amount of tetraethyl orthosilicate (TEOS) added followed by stirring. After obtaining the transparent solution, the mixture was kept at 80 °C overnight and then the gel obtained. The gel was calcined at 600 °C to burn out the organic species and the as-calcined product was heated to the phase formation temperature of the lanthanum apatite.

2.2 Luminescence and luminescence-related applications of silicate oxyapatites

2.2.1 Introduction of the luminescence mechanisms

Luminescence is a phenomenon whereby a substance is excited electronically by a certain external energy and then the excitation energy is released in the form of light, where the concept light does not only refer to the visible light but also the one in near-infrared and near-ultraviolet regions.[42] Therefore, the luminescent materials can be considered as energy converters and they can be categorized by the form of the excitation energy. For instance, the one excited by photon with emission at different energy is regarded as photoluminescent material and the one excited by cathode ray is cathodoluminescent material. Conventionally the solid luminescent material can also be termed as phosphor. However, phosphor is not clearly defined and usually represents the luminescent materials in powder form rather than single crystal, thin film or organic molecule. Most of the phosphors consist of two parts: the activators which are always the transitional metals or rare earth elements provide the desired electronic structures; and the host materials that separate the activators and modify their electronic structures.

The mechanism how the phosphors work includes two processes, excitation and emission. The configurational coordinate diagram is the most-widely used model to elaborate these processes by considering the vibrations between the activator cation and the ligand. The vibrational motion between the activator and the ligand is assumed to be harmonic, and therefore the energy of this system as a function of the distance R can be expressed as $E = \frac{1}{2}k(R - R_0)^2$ where R_0 is the equilibrium distance of the harmonic vibration system and k is the force constant. By defining the x axis as the distant R and the

y axis as the energy *E*, the configurational coordinate diagram describes this parabolic relationship (Figure 2-2).

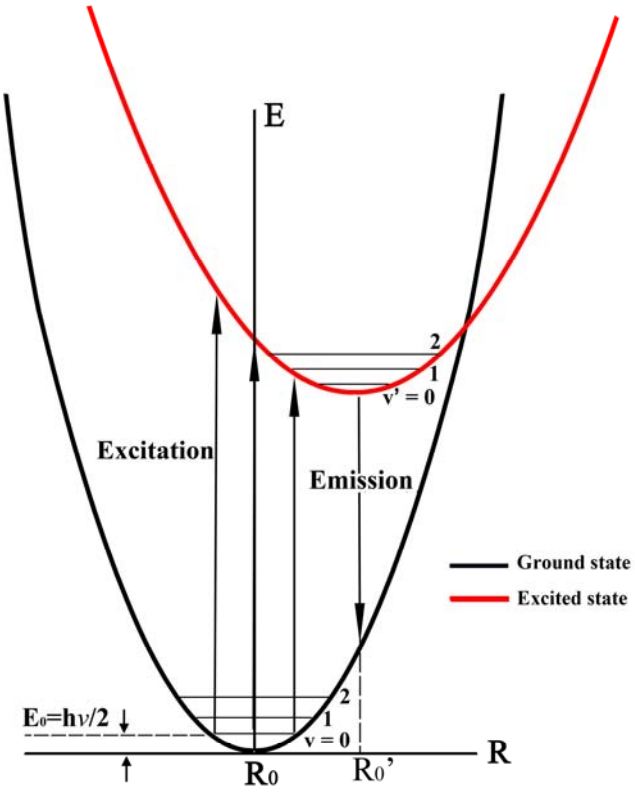

Figure 2-2 Illustration of the configurational coordinate.

In fact both ground and excited states can be described by the expression. However the values *k* and R_0 in these two states are different since the chemical bond is changed when the activator is promoted from the ground state to the excited state. Here we use *k'* and R_0' to represent these values for the excited state, distinguishing from those for the ground state *k* and R_0. The value ΔR defined as $|R_0 - R_0'|$ is a qualitative measure of the variation between the ground and the excited states. The quantum mechanics solution for energy in this harmonic oscillator model is $E_v = (\mathrm{v} + \frac{1}{2})h\nu$, where v = 0, 1, 2… and ν is the frequency of the vibration.[43] Moreover, the wave function of these discrete energies can also be obtained. The highest probability for the energy with v = 0 (E_0) occurs at $R = R_0$ while those for other energies with higher v values appear at the edges of the parabola. In

the configurational coordinate diagram, an electronic transition can be described as the vertical transition between the states, without any variation in x axis. Because the x axis represents the displacement of nuclear and the motion of nuclei is much slower than that of electron, it is reasonable to presume that the nuclei keep still when the electronic transition occurs. In the excitation process, the most probable transition is the vertical one from the lowest ground state (E_0) at R_0 to the edge of the parabola of excited state. Meanwhile the transitions from E_0 at $R > R_0$ and $R < R_0$ would also take place but with lower probabilities, resulting in a broad band in the spectrum. The emission process can be described in a similar way, with the origin at lowest excited state (E_0') at R_0' and the end at the edge of the parabola of ground state. The process that the excited electron transfers from the R_0 position to R_0' called relaxation. The energy difference between the maximum values of the excitation and emission is defined as Stokes shift. The configurational coordinate diagram can explain the width of the bands in the spectra well and it is obvious that the spectral band becomes narrow peaks when $\Delta R = 0$ and the width as well as the Stokes shift will be enhanced by larger value of ΔR. Beside the energy and its distribution of electronic transition discussed above, the intensity of the electronic transition is another important parameter and governed by the selection rules. There are two major selection rules: one is the spin selection rule that forbids the transition between different spin states; the other is the parity selection rule that forbids the transition between levels with the same parity, e.g. transitions within the *f* shell.[26] However, the selection rules are not so rigid and they will be relaxed when the activators are influenced by the host lattice through crystal field or electron-vibration coupling. Therefore, electronic transitions within 4*f* shell of rare earth elements are observed. [44, 45] These transitions appear as sharp peaks in the spectra due to $\Delta R = 0$ and the peak intensities have been theoretically studied by Ofelt and Judd.[46, 47] For example, the transitions within the 4*f* levels of Eu^{3+} are forbidden by the selection rules but in real cases, Eu^{3+} always

emit light in orange-red region [48, 49] due to the influence of the host lattice. The electric-dipole $^5D_0$-$^7F_2$ transition of Eu^{3+} is a classic demonstration to the relaxation of selection rules. This transition is hypersensitive to the inversion center and strictly forbidden if Eu^{3+} occupies a site with inversion center, whereas it will relax and gain high intensity when the symmetry of Eu^{3+} position is lower.[50].

As mentioned the interaction between the activator and the host lattice is more than just the relaxation of the selection rules,the covalency between the activator and its surrounding would induce changes of the electronic structure. Higher covalency tends to reduce the interaction between the electrons and result in the red shift of the transition energy, which is known as nephelauxetic effect.[51] The crystal field of the host lattice will also affect the electronic structure of activator significantly by lowering its center and splitting the energy levels.[52] Moreover, the electrons of the ligand may be transferred to the excited state of the activator after absorbing energy, resulting in the charge transfer band (CTB) [26] in the excitation spectrum.

The electronic transition related to one luminescent center is discussed above. But in practical situations the energy is not so localized and the interaction among multiple luminescent centers always occurs, leading to the process called energy transfer. Generally the energy transfer can be expressed as:

$$D^* + A \rightarrow D + A^* \qquad \text{Equation 2-4}$$

where D and A denote as energy donor and acceptor respectively, the asterisk * means the excited state. Dexter concludes that the energy transfer rate W_{et} can be described as:

$$W_{et} = \frac{2\pi}{\hbar}\left|\left\langle D^*, S\left|H_{DS}\right|D, S^*\right\rangle\right|^2 \int g_D(E) g_s(E) dE \qquad \text{Equation 2-5}$$

Where the matrix element presents the interaction between the initial and final state with the operator H_{DS}, the integral part represents the spectral overlap and $g(E)$ is the normalized optical line shape. This function illustrates that the energy transfer requires both the spectral overlap and the interaction between the donor and acceptor. There are

two kinds of physical interactions: one is mulitipole interaction and the other is exchange interaction. The multipole interaction performs as the donor induces a multipole (dipole, quadrupole…) oscillation on the acceptor without any physical contact between two parts. In the exchange interaction, the excited electron at D* is transferred to A* and meanwhile the ground electron at A travels to D. This process indicates that the exchange interaction requires not only the spectral overlap but also the orbital overlap of these atoms. The energy transfer is an interesting physics phenomenon and a lot of studies have focused on it. By considering the 3D environment, Blasse has calculated the expression of the energy transfer rate for both multipole and exchange interactions.[53] Moreover, the energy transfer also has important practical significance. The understanding of energy transfer explains the concentration quenching phenomenon that the emission intensity of phosphor becomes lower with high concentration of activator cations.[54] Energy transfer can also be used to improve the luminescent performance. Mn^{2+} doped $BaMgAl_{10}O_{17}$ cannot be excited effectively under short ultraviolet light (250~270 nm) to emit green light. But after co-doped with Eu^{2+}, this material has a high light output under 250~270 nm excitation since Eu^{2+} cations absorb the excitation energy and transfer to Mn^{2+}.[55]

2.2.2 Applications of luminescent materials

The understanding of the mechanism how the luminescent materials works would guide its applications. Luminescent materials are widely used for display and lighting. The most common application of phosphors in display industries is the color television. The phosphors in cathode-ray tubes are excited by beams of fast electrons, also known as cathode rays, and emit primary colors to form images on the screen.[56] In the lighting industries, phosphors are widely used such as fluorescent lamps and white LEDs. The fluorescent lamps usually utilize the discharge of the mercury vapor as the excitation source, which are ultraviolet lights at 254 and 185 nm for the lamp filled with low

mercury pressure and an additional 365 nm radiation for the one with high mercury pressure.[57] Therefore, phosphors used in the fluorescent lamps need to convert these radiations with high quantum efficiency and be stable in the mercury environment. For the daily lighting use, the emission of the phosphors also has to mimic the natural white light. It was predicted that high efficacy (100 lm/W) and excellent imitation of the natural light (CRI 80-85) can be obtained by mixing three phosphors emitting primary colors.[58] After this prediction, several suitable phosphors emerged, for example, Eu^{3+} doped Y_2O_3 as the red phosphor, Eu^{2+} doped $BaMgAl_{10}O_{17}$ as the blue phosphor and Tb^{3+} doped $CeMgAl_{11}O_{19}$ as the green phosphor.[57, 59] Recently, with the breakthrough of the high efficient GaN-based light emitting diodes (LEDs), the solid state lighting become possible and LEDs emitting white light are considered as a potential candidate to replace the incandescent and fluorescent lamps.[60-62] The white LEDs provide a great opportunity to reduce the energy consumption. The U.S. Department of Energy predicts the luminous efficacy of white LEDs by 2015 should reach an industrial applicable value of 137 lm/W.[60] If all the lighting is performed by this kind of white LEDs, it would save about 1000 trillion W·h/year and reduce carbon emission by about 200 million tons world widely.[61] As compared to the fluorescent lamps, white LEDs are mercury free and more environmental friendly. Moreover, the compact size and long lifetime are also advantages of the white LEDs over the traditional lamps.[62] The emissions of semiconductor diodes are usually in near-UV or blue region. In order to produce the white light, phosphors are needed to convert the emission from the diode chips to desired wavelengths. So far, the most commercialized white LEDs are made of GaN based blue chip and yellow YAG:Ce^{3+} phosphor.[63, 64] Part of the blue light emitted from the GaN is absorbed by YAG:Ce^{3+} and converted into yellow light. After blending the yellow light from phosphor and the blue light from the chip, white light is generated. However, due to lack of the red component in the emitting lights, color render index of this type of white LEDs is low,

leading to the appearance of objects under the illumination unnatural. An alternative way to fabricate the white LEDs is to combine a near-UV InGaN-GaN chip with blue, green and red phosphors.[65, 66] Currently the commercially applicable phosphors are $Y_2O_2S:Eu^{3+}$ as the red phosphor, $ZnS:Cu^{+}/Al^{3+}$ as the green one and $BaMgAl_{10}O_{17}:Eu^{2+}$ as the blue one. However, the efficiency of $Y_2O_2S:Eu^{3+}$ red phosphor is eight times lower than the other two phosphors.[67] Other than the lower efficiency, the sulfide based phosphor also has a poor chemical stability. Therefore, a novel red phosphor which can be effectively excited at the near UV region is needed to improve the performance of the white LEDs.

2.2.3 Luminescence studies and applications of silicate oxyapatite

The red emissions of Eu^{3+} doped silicate oxyapatites were reported by Isaacs in 1973,[68] indicating the silicate oxyapatites could be a host lattice for the luminescent materials. Since then a lot of research about luminescent materials with silicate oxyapatite structures have been done. As introduced above, two distinct cationic sites exist in the structure of silicate oxyapatite, which would affect the activators differently. Therefore, it is meaningful to study how these two crystallographic sites induce different energy levels of the activators. Meanwhile, the electronic transitions of some activator cations such as Eu^{3+} are hypersensitive to the surrounding environments and can be used as the structural probe, so it is also possible to determine the local structures around the cations and the site occupancies by interpreting the spectral properties. Blasse investigated the luminescent properties of several Eu^{3+} doped silicate oxyapatites and studied the occupancy preference between 4f (A^{I}) and 6h (A^{II}) sites.[69] The author concluded that the local charge compensation governs the occupancy trend. Since the free oxygen closely bonded to A^{II} site cannot be included into any of Si−O tetrahedra, it is underbonded according to Pauling's rules, and therefore the A^{II} site tends to accommodate cations with higher charge and/or smaller radius to compensate this underbonded oxygen. Taking

$LiLa_9(SiO_4)_6O_2$ for example, the trivalent La^{3+} is expect to enter A^{II} site due to its higher charge compared to Li^+ and if part of La^{3+} is substitute by Eu^{3+}, Eu^{3+} will also occupy A^{II} because of its smaller radius (r_{Eu3+} = 0.95 Å, r_{La3+} = 1.03 Å, both with CN = 6). Comparing this theory of site occupancy with the one proposed by Felsche [28] as mentioned above, it is found that sometimes these two theories agree with each other such as Eu^{3+} enter A^{II} after replacing La^{3+} in $LiLa_9(SiO_4)_6O_2$. However, contradictions between both theories occasionally happen. For instance, smaller Li^+ should occupy smaller A^{II} site in $LiLa_9(SiO_4)_6O_2$ according to Felsche's theory rather than A^I site as concluded by Blasse. By analyzing high resolution photoluminescence spectra of three silicate oxyapatites, $MY_8(SiO_4)_6O_2:Eu^{3+}$ (M = Mg, Ca, Sr), Lin and Su found Eu^{3+} occupying two cationic sites simultaneously and they attributed this phenomenon to the compromise of the size effect proposed by Felsche and the charge compensation effect proposed by Blasse.[70] All these studies were only focused on the spectral analysis and did not use other materials characterization techniques such as X-ray diffraction and Rietveld refinement. Moreover the relationships between the crystal structure and spectral properties of other activators were also reported. For example, Tb^{3+} and Ce^{3+} doped deficit silicate oxyapatites $Ln_{9.33}(SiO_4)_6O_2$ (Ln = Gd, La) also showed characteristics of two crystallographic sites in the spectra.[71] Pr^{3+}, Dy^{3+} and Pb^{2+} doped silicate oxyapatites were also reported.[72-74] More practically, some applications of the phosphor with silicate oxyapatite structures have been discovered. Eu^{2+} and Mn^{2+} doped $Ba_2La_8(SiO_2)_6O_2$, which can be excited effectively at 254 nm, was patented as a yellow-green phosphor for the fluorescent lamp.[75] Tb^{3+} doped $Sr_2Gd_8(SiO_4)_6O_2$ was proposed to be a potential candidate of green phosphor for the plasma display panels (PDP) due to its excitation at vacuum ultraviolet region.[76] Although lots of studies about Eu^{3+} doped silicate oxyapatites have been conducted, most of them used Eu^{3+} as the structural probe and the

utilization of the red emission was limited. Also few studies explore the applications in the white LED which emerges as a hot topic for new generation of lighting.

Not only limited to the application of lighting phosphor, silicate oxyapatites are also applied in other luminescent-related field such as scintillators and lasers. Scintillator is important in detection of high energy photon, such as X-ray and gamma ray, and high energy particle like neutron and α particles.[77] It absorbs these radiations and subsequently converts them to UV-visible light which is easier to detect and collect using photomultipler or photodiodes. Hence, scintillators are widely applied in biomedical diagnostics, for example, as detectors in the PET machine, and high energy physics like electromagnetic calorimeters.[78-80] Transparency is required for scintillators because it helps to deliver the converted UV-visible light to the detectors efficiently.[81] Silicate oxyapatites $Ln_{9.33}(SiO_4)_6O_2$ (Ln = Gd, Yb, La and Lu) doped with Ce^{3+} alone or co-doped with Tb^{3+} were patented as scintillators for X-ray and gamma ray by Francois *et al*.[82] The silicate apatite structure demonstrated high stability over large temperature range and lower segregation of the activators. These scintillators were all transparent single crystals grown by Czochralski method.

Steinbruegge *et al.* [20] tested various silicate oxyapatite single crystals and suggested that these materials are excellent laser hosts for Nd^{3+} and Ho^{3+} in 1973. Druon *et al.* [83, 84] have fabricated Yb^{3+} doped $Sr_2Y_8(SiO_4)_6O_2$ transparent single crystal by Czochralski method. It generates infrared pulsed laser of 1070 nm wavelength with 94-femtosecond duration after applying it as the activator crystal inside the laser chamber. The development of those ultrafast lasers is meaningful in both fundamental research and industrial applications such as time resolved spectroscopy, refractive surgery, bio-imaging and the nano-machining.[27] A host lattice with disorder crystal structure is favored in the ultrafast laser, because the disorder structure tends to broaden the activator's energy

levels and produce shorter laser pulse.[85, 86] Therefore, $Sr_2Y_8(SiO_4)_6O_2$, where two cations distributed in two crystallographic sites, was chosen as the host lattice.

2.3 Transparent/translucent ceramic

2.3.1 Introduction of transparent/translucent ceramic

The above introduction about the application of lasers and scintillators indicates that the single crystals of silicate oxyapatites with high transparency are useful. All these silicate oxyapatite single crystals were grown by the Czochralski method. In fact, many other single crystals such as rare earth doped Lu_2SiO_5 [87, 88] and YAG [89-91] have been grown and studied and used in lasers and scintillators. Czochralski method grows single crystal from the melt with desired constitutes. A seed crystal will be introduced to the melt to promote the nucleation and as it spins and lifts slowly, cylindrical single crystal with high transparency can be obtained. Nevertheless, there are some inevitable shortcomings of this method. First of all, the whole growth process goes under the environment with extreme high temperature (above 2000˚C). It requires not only a large amount of energy to maintain this environment but also expensive equipments that can stand with high temperature, for example, the iridium crucible as the container for the melts. Moreover, the method is time-consuming. Usually the growth rate is about millimeters per hour or even slower. Therefore, it takes about days even several weeks to grow a single crystal to a desired size. Last but not least, the compositional variation in the single crystal will occur due to different solubilities of the elements in the solid and liquid phases. Taking YAG:Nd^{3+} for example, the segregation coefficient for Nd^{3+} is about 0.2 which means its solubility in liquid is four times higher than that in solid. Subsequently, more Nd cations exist in the melt than the solid crystal during the growth process. The segregation effect not only leads to chemical inhomogeneity but also limits the doping concentration, for example, maximum Nd^{3+} about 1 at% in YAG:Nd^{3+}.[92]

Most of these disadvantages can be overcome by transparent polycrystalline ceramics. Transparent polycrystalline ceramics consist of tightly compacted grains, usually in

micrometer scale, with random orientations. Since the crystallization from the melt liquid is avoided, the segregation effect is much less important and the doped concentration can reach higher, for example, up to 9 at.% Nd^{3+} in YAG:Nd^{3+},[93] and the chemical homogeneity still maintains. The production procedures are more effective than single crystal growth both in time and cost aspects. Moreover, the optical, mechanical and thermal properties of the transparent ceramics are comparable, if not superior, to the single crystal counterpart.[92, 94] Another important advantage of transparent ceramics is that tailored shape and different composites can be achieved by the ceramic processing techniques.[95] Therefore, various materials have been fabricated into transparent/translucent ceramics and various applications of them have been discovered not only as lasers crystals and scintillators. Transparent ceramic $Y_3Al_5O_{12}$:Nd^{3+} laser was first produced by Ikesue [96] and later the optical performance of this type of solid state laser was improved and comparable to the single crystal counterpart.[97] Scintillator materials such as Lu_2SiO_5:Ce^{3+} [98] and $(Gd,Y)_2O_3$:Eu^{3+} [99] were also fabricated into transparent ceramic forms and demonstrated excellent scintillation performances. Moreover, transparent or translucent polycrystalline alumina was used as the envelope in high-pressure sodium and metal-halide lamps due to its high resistance to thermal shock and corrosive vapor.[100] In addition, aluminum oxynitride (ALON) and $MgAl_2O_4$ are the candidates for the transparent armor mostly because of their superior mechanical properties.[101]

For wide band-gap oxides, the energy required to overcome the band-gap is much larger than the energy of visible light. So the absorption of visible light can be neglect and the transmittance (I/I_0) of ceramics can be expressed as:[102]

$$I/I_0 = (1-R)^2 \exp(-C_{sca}\, t) \qquad \text{Equation 2-6}$$

where I is the intensity of transmitted light, I_0 is the intensity of incident light, R is the reflectivity, C_{sca} is the effective scattering coefficient, and t is the thickness of the sample. The absorption coefficient, C_{sca}, can be given as

$$C_{sca} = C_{im} + C_{op} \qquad \text{Equation 2-7}$$

Where C_{im} is the scattering terms due to structural inhomogeneity such as pores and second phase, C_{op} is the scattering terms due to optical anisotropy.[103] Usually the ceramic is not transparent because when the light goes through, light would be scattered mainly at four places such as pores, grain boundaries, second-phase inclusions and rough surface (Figure 2-3).[104] For the purpose of obtaining ceramic with high light transmittance, these light scattering effects in the ceramic should be avoided or eliminated.

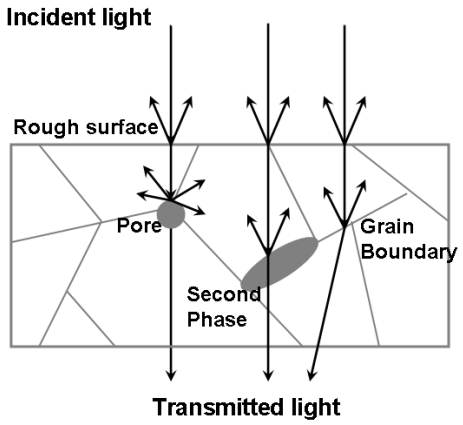

Figure 2-3 Light scattering inside the ceramic.

Scattering by the residual pores inside the ceramic body is considered as the main cause of the reduction of transparency and Peelen and Metselaar [105] studied light scattering effect by pores in high-density ceramics. First, based on the Mie theory, the authors calculated the light transmittance as a function of porosity with a fixed and distributed pore radius respectively. After that, they compared the calculations with the experimental data obtained from conventional sintered and hot pressed alumina and good agreements between calculated and experimental results were achieved. At last, the author

concluded that it is possible to obtain highly transparent ceramics by reducing the porosity and the pore size. Advanced sintering techniques are necessary to obtain highly condensed ceramics with low porosity and small pore size.

To discuss the light scattering effect by grain boundaries, some preliminary knowledge should be proposed. First, light reflection and refraction will occur at the interface of mediums with different refractive indexes. Second, non-cubic crystal structures have anisotropic optical properties and the refractive indexes are different in the various crystallographic directions. Last, polycrystalline ceramics consist of many small random-orientated crystallites. So in non-cubic structured ceramics, the light will be scattered at grain boundaries if the neighbor crystallites are not aligned in the same optical axis. This type of scattering becomes dominant when the porosity and pore size are very small. Apetz and van Bruggen studied fully dense α-alumina and discussed the effect of grain size on grain boundary scattering.[104] Based on the Mie theory and Rayleigh-Gans-Debye theory, they established a model by assuming that the fully dense alumina ceramic microstructure exist as mono-dispersed spheres (with a diameter d and refractive index n_2) randomly distributed in matrix with refractive index n_1. The *d* value equals to the mean grain size, n_1 and n_2 are the refractive index of α-alumina from different optical axis.

$$T = (1-R) \exp(-3\pi^2 d \Delta n^2 t/2\lambda^2) \qquad \text{Equation 2-8}$$

Where *T* is in-line transmission, *R* is the reflection fraction, *d* is the grain size, t is the thickness of the sample, λ is the wavelength of light and $\Delta n = |n_1 - n_2|$. The calculation shows that the transmittance increases exponentially with the decrease of grain size in dense alumina ceramics. Moreover, the calculated curve is verified by experimental data.

Surface roughness can be minimized by polishing the sample surfaces and the second-phase inclusions can be eliminated by modified the synthesis process to produce high pure raw ceramic powder.

The requirement of transparency varies for different applications. In order to obtain high laser efficiency, the transparency of the polycrystalline ceramic should meet strict requirement and be comparable to that of single crystals. The porosity inside the ceramic body should be reduced to the order of ppm.[96, 106] Moreover, all the host lattices for the laser application such as yttrium aluminum garnet ($Y_3Al_5O_{12}$ or YAG),[96, 107] Y_2O_3,[108, 109] Sc_2O_3,[110] Lu_2O_3 [111] and $Y_3(Sc_{0.5}Al_{0.5})_2O_{12}$ [112] have cubic symmetry to reduce the birefringence effect and further increase the transparency. For the ceramics used as scintillators whose functions are to stop the external radiation and transport the converted light, the requirement of transparency is less rigid. Ceramic form of $Lu_2SiO_5:Ce^{3+}$ (LSO:Ce) with relative density about 99% was fabricated and tested for both X-ray and gamma ray.[98, 113] LSO has a crystallographic symmetry of monoclinic. The optical anisotropic properties and the higher porosity reduce the transparency dramatically and resulted in a translucent rather than transparent ceramic. However, the light yields of polycrystalline LSO:Ce in both X-ray and gamma ray tests were comparable to those of LSO:Ce single crystals, which demonstrates their potential applications as scintillators.

2.3.2 Sintering methods

The sintering method is crucial for the fabrication of pore-free ceramics. With the help of pressure and heating, hot pressing (HP) and hot isostatic pressing (HIP) are promising ways to produce transparent ceramics. Y_2O_3 [114] and Sc_2O_3 [115] transparent ceramic was fabricated by hot pressing decades ago and many other oxides like ZrO_2, MgO and YAG [116-119] have been made to transparent form by HP and HIP. In 1995, the first Nd^{3+} doped YAG ceramic for laser was fabricated by vacuum sintering method [96] and since then, vacuum sintering have been intensively studied to produce different kind of transparent ceramics with high optical qualities.[108-112] More recently the spark plasma sintering (SPS) attracted much attention. The schematic apparatus of SPS is shown in Figure 2-4. The

sample is placed inside a graphite die, and then aligned into the apparatus with external pressure. During the SPS process, the pulsed DC current directly passes through the graphite die and, therefore, the heat is generated internally while in conventional sintering the heat is applied externally. The most unique property of SPS is ultra-high heat rate (up to 1000 k/min) and it can minimize the coarsening effect which will reduce the driving force [120] for densification. Fast heat can also suppress the grain growth and reduce the light scattering at grain boundaries.[121] Undoubtedly, time-efficiency can also be improved by fast sintering. Moreover, as mentioned above, the internal heat source results in an even temperature distribution in the sample. In addition, pressure applied during sintering may enhance the densification by sliding of the particles.[120] Some studies also suggested that the electric-field assisted sintering would affect the mass transfer mechanism and, further, the densification process.[122,123]

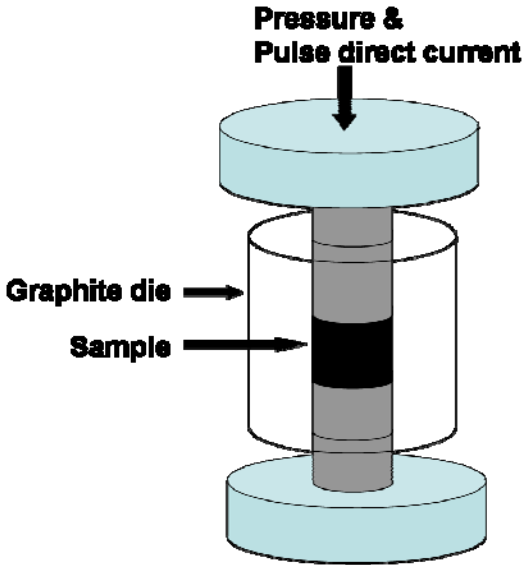

Figure 2-4 Set-up of the spark plasma sintering.

Various highly dense or even transparent ceramics are synthesized by spark plasma sintering. R. Chaim and his colleagues [124] used pure commercial nanocrystalline YAG powder as starting material and after SPS they obtained transparent YAG ceramic with density up to 99.8%. The authors didn't give any evaluation of the optical properties but

they proposed a mechanism of the densification during SPS. At the temperature range 1250℃-1400℃, the SPS induces the powder surface temperature as high as the melting point of YAG and liquid layers form at the particles' surfaces. Nanoparticles rotate and slide in present of external pressure and liquid phase, resulting in rapid densification with suppressed grain growth. After that, slow densification with fast curvature driven grain growth occur in 1400℃-1500℃. R. Chaim also synthesized transparent MgO by spark plasma sintering [120] in a lower temperature (700℃-800℃) than vacuum sintering (up to 1600℃). Final transparent pellet has grain sizes range between 30 nm and 63 nm with porosity as low as 0.35% and pore size up to 100 nm. The maximum in-line transmission is 45% with incident wavelength 700 nm. Not only cubic structured materials like YAG and MgO but also non-cubic structured materials are fabricated into ceramics with high transparency by SPS. The α-alumina belongs to hexagonal crystal structure and its transparent ceramic is fabricated in SPS by B. Kim and his colleagues.[121] The authors used commercial α-alumina powder and heated the powder at 1150℃ under pressure of 80 MPa in SPS apparatus. Slow heating rate is chosen as 25℃/min from 600℃-1000℃ and followed by 8℃/min to 1150℃. Ultimately, transparent ceramic (in-line transmission 47% at wavelength 640 nm) is obtained with mean grain size 270 nm and residual porosity 0.03%.

2.4 References

1. K. C. Ruttenberg & R. A. Berner, (1993). Authigenic Apatite Formation and Burial in Sediments from Non-upwelling, Continental-margin Environments. *Geochimica Et Cosmochimica Acta*, 57 (5), 991-1007.
2. T. Kokubo, H. M. Kim & M. Kawashita, (2003). Novel Bioactive Materials with Different Mechanical Properties. *Biomaterials*, 24 (13), 2161-2175.
3. G. He, T. Dahl, A. Veis & A. George, (2003). Nucleation of Apatite Crystals in Vitro by Self-assembled Dentin Matrix Protein 1. *Nature Materials*, 2 (8), 552-558.
4. K. A. Gross & C. C. Berndt, (2002). Biomedical Application of Apatites. *Reviews in Mineralogy and Geochemistry*, 48 (1), 631-672.
5. P. H. J. Mercier, Y. Le Page, P. S. Whitfield, L. D. Mitchell, I. J. Davidson & T. J. White, (2005). Geometrical Parameterization of the Crystal Chemistry of $P6_3/m$ Apatites: Comparison with Experimental Data and ab initio results. *Acta Crystallographica Section B*, 61, 635-655.
6. T. Dordevic, S. Sutovic, J. Stojanovic & L. Karanovic, (2008). Sr, Ba and Cd Arsenates with the Apatite-type Structure. *Acta Crystallographica Section C*, 64, 82-86.
7. Y. Pan & M. E. Fleet. (2002). Phosphates: Geochemical, Geobiological, and Materials Importance. In M. J. Kohn, J. Rakovan & J. M. Hughes (Eds.), *Reviews in Mineralog and Geochemistry* (pp. 15-29). Washington: Mineralogical Society of America.
8. Y. P. Xu & F. W. Schwartz, (1994). Lead Immobilization by Hydroxyapatite in Aqueous-solutions. *Journal of Contaminant Hydrology*, 15 (3), 187-206.
9. X. B. Chen, J. V. Wright, J. L. Conca & L. M. Peurrung, (1997). Effects of pH on Heavy Metal Sorption on Mineral Apatite. *Environmental Science & Technology*, 31 (3), 624-631.
10. W. J. Weber, R. C. Ewing & A. Meldrum, (1997). The Kinetics of Alpha-decay-induced Amorphization in Zircon and Apatite Containing Weapons-grade Plutonium or Other Actinides. *Journal of Nuclear Materials*, 250 (2-3), 147-155.
11. Q. Y. Ma, S. J. Traina, T. J. Logan & J. A. Ryan, (1993). In-situ Lead Immobilization by Apatite. *Environmental Science & Technology*, 27 (9), 1803-1810.
12. X. B. Chen, J. V. Wright, J. L. Conca & L. M. Peurrung, (1997). Evaluation of Heavy Metal Remediation Using Mineral Apatite. *Water Air and Soil Pollution*, 98 (1-2), 57-78.
13. J. S. Arey, J. C. Seaman & P. M. Bertsch, (1999). Immobilization of Uranium in Contaminated Sediments by Hydroxyapatite Addition. *Environmental Science & Technology*, 33 (2), 337-342.
14. Z. L. Dong, T. J. White, B. Wei & K. Laursen, (2002). Model Apatite Systems for the Stabilization of Toxic Metals: I, Calcium Lead Vanadate. *Journal of the American Ceramic Society*, 85 (10), 2515-2522.
15. J. Y. Kim, Z. L. Dong & T. J. White, (2005). Model Apatite Systems for the Stabilization of Toxic Metals: II, Cation and Metalloid Substitutions in Chlorapatites. *Journal of the American Ceramic Society*, 88 (5), 1253-1260.
16. S. Naray-Szabo, (1930). The Structure of Apatite $(CaF)Ca_4(PO_4)_3$. *Zeitschrift Fur Kristallographie*, 75 (5-6), 387-398.
17. J. C. Elliot (1994). *Structure and Chemistry of the Apatites and Other Calcium Orthophosphates*. Amsterdam: Elsevier.
18. T. J. White & Z. L. Dong, (2003). Structural Derivation and Crystal Chemistry of Apatites. *Acta Crystallographica Section B*, 59, 1-16.
19. M. G. Zuev, A. M. Karpov & A. S. Shkvarin, (2010). Synthesis and Spectral Characteristics of $Sr_2Y_8(SiO_4)_6O_2$:Eu Polycrystals. *Journal of Solid State Chemistry*, 184 (1), 52-58.

20. K. B. Steinbruegge, T. Henningsen, R. H. Hopkins, R. Mazelsky, N. T. Melamed, E. P. Riedel & G. W. Roland, (1972). Laser Properties of Nd^{+3} and Ho^{+3} Doped Crystals with Apatite Structure. *Applied Optics*, 11 (5), 999-1012.
21. M. S. Islam, J. R. Tolchard & P. R. Slater, (2003). An Apatite for Fast Oxide Ion Conduction. *Chemical Communications*, 13, 1486-1487.
22. V. V. Kharton, A. L. Shaula, M. V. Patrakeev, J. C. Waerenborgh, D. P. Rojas, N. P. Vyshatko, E. V. Tsipis, A. A. Yaremchenko & F. M. B. Marques, (2004). Oxygen Ionic and Electronic Transport in Apatite-type Solid Electrolytes. *Journal of the Electrochemical Society*, 151 (8), 1236-1246.
23. P. R. Slater, J. E. H. Sansom & J. R. Tolchard, (2004). Development of Apatite-type Oxide Ion Conductors. *Chemical Record*, 4 (6), 373-384.
24. H. C. Yao, J. S. Wang, D. G. Hu, J. F. Li, X. R. Lu & Z. J. Li, (2010). New Approach to Develop Dense Lanthanum Silicate Oxyapatite Sintered Ceramics with high conductivity. *Solid State Ionics*, 181, 41-47.
25. M. Sayer, J. Reid, T. Smith & J. Hendry, (2009). Silicon Substituted Oxyapatite. *US Patent*, 7498043.
26. G. Blasse & B. C. Grabmajer, (1994). *Luminescent Materials*. Berlin: Springer-Verlag.
27. F. Druon, F. Balembois & P. Georges, (2003). Laser Crystals for the Production of Ultra-short Laser Pulses. *Annales de Chimie-science des Materiaux*, 28, 47-72.
28. J. Felsche, (1972). Rare-earth Silicates with Apatite Structure. *Journal of Solid State Chemistry*, 5 (2), 266-275.
29. R. P. Gunawardane, R. A. Howie & F. P. Glasser, (1982). Structure of the Oxyapatite $NaY_9(SiO_4)_6O_2$. *Acta Crystallographica Section B*, 38 (May), 1564-1566.
30. Y. Masubuchi, M. Higuchi, T. Takeda & S. Kikkawa, (2006). Oxide Ion Conduction Mechanism in $RE_{9.33}(SiO_4)_6O_2$ and $Sr_2RE_8(SiO_4)_6O_2$ (RE=La, Nd) from Neutron Powder Diffraction. *Solid State Ionics*, 177 (3-4), 263-268.
31. G. R. Redhammer & G. Roth, (2003). Lithium and Sodium Yttrium Orthosilicate Oxyapatite, $LiY_9(SiO_4)_6O_2$ and $NaY_9(SiO_4)_6O_2$, at Both 100 K and Near Room Temperature. *Acta Crystallographica Section C*, 59, 120-124.
32. H. C. Yao, J. S. Wang, D. G. Hu, J. F. Li, X. R. Lu & Z. J. Li, (2010). New Approach to Develop Dense Lanthanum Silicate Oxyapatite Sintered Ceramics with High Conductivity. *Solid State Ionics*, 181 (1-2), 41-47.
33. S. M. Haile, B. J. Wuensch, T. Siegrist & R. A. Laudise, (1993). Hydrothermal Synthesis of New Alkali Silicates. 1. Potassium Neodymium Phases. *Journal of Crystal Growth*, 131 (3-4), 352-372.
34. C. J. Brinker & G. W. Scherer, (1990). *Sol-gel Science: the Physics and Chemistry of Sol-gel Processing*. San Diego: Academic Press.
35. L. L. Hench & J. K. West, (1990). The Sol-gel Process. *Chemical Reviews*, 90 (1), 33-72.
36. S. Celerier, C. Laberty, F. Ansart, P. Lenormand & P. Stevens, (2006). New Chemical Route Based on Sol-gel Process for the Synthesis of Oxyapatite $La_{9.33}Si_6O_{26}$. *Ceramics International*, 32 (3), 271-276.
37. S. W. Tao & J. T. S. Irvine, (2001). Preparation and Characterisation of Apatite-type Lanthanum Silicates by a Sol-gel Process. *Materials Research Bulletin*, 36 (7-8), 1245-1258.
38. Y. Masubuchi, M. Higuchi, T. Takeda & S. Kikkawa, (2006). Preparation of Apatite-type $La_{9.33}(SiO4)_6O_2$ Oxide ion Conductor by Alcoxide-hydrolysis. *Journal of Alloys and Compounds*, 408, 641-644.
39. Y. Otsuka & S. Fujihara, (2007). Transparent and Luminescent Thin films of Partially Substituted $La_{10}(SiO_4)_6O_3$: Eu^{3+} Apatite-type Silicates. *Journal of the Electrochemical Society*, 154 (10), 335-340.

40. S. Celerier, C. Laberty-Robert, F. Ansart, C. Calmet & P. Stevens, (2005). Synthesis by Sol-gel Route of Oxyapatite Powders for Dense Ceramics: Applications as Electrolytes for Solid Oxide Fuel Cells. *Journal of the European Ceramic Society*, 25 (12), 2665-2668.
41. J. Sanchez & A. McCormick, (1991). NMR and Theoretical Investigation of Cation Binding with Sol-gel Silicates. *Chemistry of Materials*, 3 (2), 320-324.
42. S. Shionoya, (2006). Introduction to the Handbook. In W. M. Yen, S. Shionoya & H. Yamamoto (Eds.), *Phosphor Handbook* (Chapter 1). Boca Raton: CRC Press:, 2006.
43. P. W. Atkins, (1990). *Physical Chemistry*. Oxford: Oxford University Press.
44. W. T. Carnall, G. L. Goodman, K. Rajnak & R. S. Rana, (1989). A Systematic Analysis of the Spectra of the Lanthanides Doped into Single-crystal LaF_3. *Journal of Chemical Physics*, 90 (7), 3443-3457.
45. G. H. Dieke, (1968). *Spectra and Energy Levels of Rare Earth Ions in Crystals*. New York: Interscience Publishers.
46. G. S. Ofelt, (1962). Intensities of Crystal Spectra of Rare-earth Ions. *Journal of Chemical Physics*, 37 (3), 511-520.
47. B. R. Judd, (1962). Optical Absorption Intensities of Rare-earth Ions. *Physical Review*, 127 (3), 750-761.
48. G. Blasse & A. Bril, (1967). Structure and Eu^{3+} Fluorescence of Lithium and Sodium Lanthanide Silicates and Germanates. *Journal of Inorganic & Nuclear Chemistry*, 29 (9), 2231-2241.
49. G. Blasse, (1966). On Eu^{3+} Fluorescence of Mixed Metal Oxides. 4. Photoluminescent Efficiency of Eu^{3+} Activated Oxides. *Journal of Chemical Physics*, 45 (7), 2356-2360.
50. G. Blasse, A. Bril & Nieuwpoo.Wc, (1966). On Eu3+ Fluorescence in Mixed Metal Oxides. 1. Crystal Structure Sensitivity of Intensity Ratio of Electric and Magnetic Dipole Emission. *Journal of Physics and Chemistry of Solids*, 27 (10), 1587-1592.
51. C. E. Housecroft & A. G. Sharpe, (2005). *Inorganic Chemistry*. England: Pearson Education.
52. J. H. Van Vleck, (1932). Theory of the Variations in Paramagnetic Anisotropy among Different Salts of the Iron Group. *Physical Review*, 41 (2), 208-215.
53. R. C. Powell & G. Blasse, (1980). Energy Transfer in Concentrated Systems. *Structure and Bonding*, 42, 43-96.
54. L. G. Van Uitert & L. F. Johnson, (1966). Energy Transfer between Rare-earth Ions. *Journal of Chemical Physics*, 44 (9), 3514-3522.
55. A. L. N. Stevels & J. M. P. J. Verstegen, (1976). Eu^{2+} ->Mn^{2+} Energy Transfer in Hexagonal Aluminates. *Journal of Luminescence*, 14 (3), 207-218.
56. A. E. Hardy, (1965). Performance of Color-television Picture-tube Phosphor Screens. *IEEE Transactions on Broadcast and Television Receivers*, 11 (2), 33-37.
57. A. M. Srivastava & T. J. Sommerer, (1998). Fluorescent Lamp Phosphors. *The Electrochemical Society-Interface*, 7 (28-31), 28.
58. M. Koedam & J. J. Opstelten, (1971). Measurement and Computer-aided Optimization of Spectral Power Distributions. *Lighting Research and Technology*, 3, 205-210.
59. J. M. P. Verstege, D. Radielov & L. E. Vrenken, (1974). New Generation of Deluxe Fluorescent Lamps, Combining an Efficacy of 80 Lumens/W or More with a Color Rendering Index of Approximately 85. *Journal of the Electrochemical Society*, 121 (12), 1627-1631.
60. Navigant Consulting, Inc. (2006). *Solid-State Lighting Research and Development Portfolio*, pp. 48.

61. M. R. Krames, O. B. Shchekin, R. Mueller-Mach, G. O. Mueller, L. Zhou, G. Harbers & M. G. Craford, (2007). Status and Future of High-power Light-emitting Diodes for Solid-state Lighting. *Journal of Display Technology*, 3 (2), 160-175.
62. D. A. Steigerwald, J. C. Bhat, D. Collins, R. M. Fletcher, M. O. Holcomb, M. J. Ludowise, P. S. Martin & S. L. Rudaz, (2002). Illumination with Solid State Lighting Technology. *IEEE Journal of Selected Topics in Quantum Electronics*, 8 (2), 310-320.
63. R. Mueller-Mach, G. O. Mueller, M. R. Krames & T. Trottier, (2002). High-Power Phosphor-converted Light-emitting Diodes Based on III-nitrides. *IEEE Journal of Selected Topics in Quantum Electronics*, 8 (2), 339-345.
64. C. R. Ronda, T. Justel & H. Nikol, (1998). Rare Earth Phosphors: Fundamentals and Applications. *Journal of Alloys and Compounds*, 275, 669-676.
65. S. Muthu, F. J. P. Schuurmans & M. D. Pashley, (2002). Red, Green, and Blue LEDs for White Light Illumination. *IEEE Journal of Selected Topics in Quantum Electronics*, 8 (2), 333-338.
66. J. K. Sheu, S. J. Chang, C. H. Kuo, Y. K. Su, L. W. Wu, Y. C. Lin, W. C. Lai, J. M. Tsai, G. C. Chi & R. K. Wu, (2003). White-light Emission from Near UV InGaN-GaN LED Chip Precoated with Blue/green/red Phosphors. *IEEE Photonics Technology Letters*, 15 (1), 18-20.
67. S. Neeraj, N. Kijima & A. K. Cheetham, (2004). Novel Red Phosphors for Solid-State Lighting: the System $NaM(WO_4)_{2-x}(MoO_4)_x$: Eu^{3+} (M=Gd, Y, Bi). *Chemical Physics Letters*, 387 (1-3), 2-6.
68. T. J. Isaacs, (1973). Study of Eu^{3+} Fluorescence in Some Silicate Oxyapatites. *Journal of the Electrochemical Society*, 120 (5), 654-656.
69. G. Blasse, (1975). Influence of Local Charge Compensation on Site Occupation and Luminescence of Apatites. *Journal of Solid State Chemistry*, 14 (2), 181-184.
70. J. Lin & Q. Su, (1994). A Study of Site Occupation of Eu^{3+} in $ME_2Y_8(SiO_4)_6O_2$ (ME=Mg, Ca, Sr). *Materials Chemistry and Physics*, 38 (1), 98-101.
71. M. J. J. Lammers & G. Blasse, (1987). Luminescence of Tb3+-activated and Ce3+-activated Rare-earth Silicates. *Journal of the Electrochemical Society*, 134 (8A), 2068-2072.
72. X. H. Chuai, H. J. Zhang, F. S. Li, S. Z. Lu, J. Lin, S. B. Wang & C. C. Kou, (2002). Synthesis and Luminescence Properties of Oxyapatite $NaY_9Si_6O_{26}$ doped with Eu^{3+}, Tb^{3+}, Dy^{3+} and Pb^{2+}. *Journal of Alloys and Compounds*, 334, 211-218.
73. M. Yu, J. Lin, Y. H. Zhou, S. B. Wang & H. J. Zhang, (2002). Sol-gel Deposition and Luminescent Properties of Oxyapatite $Ca_2(Y,Gd)_8(SiO_4)_6O_2$ Phosphor Films Doped with Rare Earth and Lead Ions. *Journal of Materials Chemistry*, 12 (1), 86-91.
74. J. P. M. Vanvliet & G. Blasse, (1990). Luminescence from Pr^{3+} in Barium Lanthanum Silicate Oxyapatite. *Materials Research Bulletin*, 25 (3), 391-394.
75. G. A. Sigai & M. N. Alexander, (1988). Yellow Green Barium Lanthanum Silicate Oxyapatite Phosphor, a Fluorescent Lamp Containing the Same, and a Method thereof. *US Patent*, 4748391.
76. A. Yamane, T. Kunimoto, K. Ohmi, T. Honma & H. Kobayashi, (2006). Luminescent Properties of Tb-activated Rare-Earth Oxyapatite Silicate $MLn_4Si_3O_{13}$ (M=Ca, Sr, Ln=La, Gd). *Physica Status Solidi C*, 3 (8), 2705-2708.
77. M. Nikl, (2000). Wide Band Gap Scintillation Materials: Progress in the Technology and Material Understanding. *Physica Status Solidi A*, 178 (2), 595-620.
78. G. Blasse, (1994). Scintillator Materials. *Chemistry of Materials*, 6 (9), 1465-1475.
79. M. J. Weber, (2002). Inorganic Scintillators: Today and Tomorrow. *Journal of Luminescence*, 100 (1-4), 35-45.
80. C. W. E. van Eijk, (2002). Inorganic Scintillators in Medical Imaging. *Physics in Medicine and Biology*, 47 (8), 85-106.

81. C. Greskovich & S. Duclos, (1997). Ceramic Scintillators. *Annual Review of Materials Science*, 27, 69-88.
82. B. Francois, M. Navizet, J. C. Rebreyend & C. Wyon, (1991). Monocrystals of Silicates of Lanthanides Usable as Scintillators for the Detection of X and Gamma Radiation. *US Patent*, 4988882.
83. F. Druon, F. Balembois & P. Georges, (2000). Generation of 90-fs Pulses from a Mode-locked Diode-pumped Yb^{3+}:$Ca_4GdO(BO_3)_3$ laser. *Opictics Letters*, 25 (6), 423-435.
84. F. Druon, S. Chenais & F. Raybaut, (2002). Apatite-structure Crystal, Yb^{3+}:$SrY_4(SiO_4)_3O$, for the Development of Diode-pumped Femtosecond Lasers. *Optics Letters*, 27 (21), 1914-1916.
85. P. H. Haumesser, R. Gaume, B. Viana, E. Antic-Fidancev & D. Vivien, (2001). Spectroscopic and Crystal-field Analysis of New Yb-doped Laser Materials. *Journal of Physics-Condensed Matter*, 13 (23), 5427-5447.
86. F. Druon, F. Balembois & P. Georges, (2003). Laser Crystals for the Production of Ultra-short Laser Pulses. *Annales de Chimie-science des Materiaux*, 28 (6), 47-72.
87. G. H. Ren, L. S. Qin, S. Lu & H. Y. Li, (2004). Scintillation Characteristics of Lutetium Oxyortho-silicate (Lu_2SiO_5:Ce) Crystals Doped with Cerium Ions. *Nuclear Instruments & Methods in Physics Research Section A*, 531 (3), 560-565.
88. C. L. Melcher & J. S. Schweitzer, (1992). Cerium-doped Lutetium Oxyorthosilicate - a Fast, Efficient New Scintillator. *IEEE Transactions on Nuclear Science*, 39 (4), 502-505.
89. E. Zych, C. Brecher & J. Glodo, (2000). Kinetics of Cerium Emission in a YAG:Ce Single Crystal: the Role of Traps. *Journal of Physics-Condensed Matter*, 12 (8), 1947-1958.
90. R. Autrata, P. Schauer & J. Kvapil, (1978). Single-crystal of YAG - New Fast Scintillator in SEM. *Journal of Physics E*, 11 (7), 707-708.
91. P. Z. Yang, P. Z. Deng, J. Xu & Z. W. Yin, (2000). Growth of High-quality Single Crystal of 30 at% Yb:YAG and Its Laser Performance. *Journal of Crystal Growth*, 216 (1-4), 348-351.
92. V. Lupei, A. Lupei & A. Ikesue, (2004). Single Crystal and Transparent Ceramic Nd-doped Oxide Laser Materials: a Comparative Spectroscopic Investigation. *Journal of Alloys and Compounds*, 380 (1-2), 61-70.
93. S. H. Lee, S. Kochawattana, G. L. Messing, J. Q. Dumm, G. Quarles & V. Castillo, (2006). Solid-state Reactive Sintering of Transparent Polycrystalline Nd : YAG Ceramics. *Journal of the American Ceramic Society*, 89 (6), 1945-1950.
94. L. Mezeix & D. J. Green, (2006). Comparison of the Mechanical Properties of Single Crystal and Polycrystalline Yttrium Aluminum Garnet. *International Journal of Applied Ceramic Technology*, 3 (2), 166-176.
95. A. Ikesue & Y. L. Aung, (2006). Synthesis and Performance of Advanced Ceramic Lasers. *Journal of the American Ceramic Society*, 89 (6), 1936-1944.
96. A. Ikesue, T. Kinoshita, K. Kamata & K. Yoshida, (1995). Fabrication and Optical Properties of High-perforemance Polycrystalline Nd-YAG Ceramics for Solid-State Lasers. *Journal of the American Ceramic Society*, 78 (4), 1033-1040.
97. J. Lu, M. Prabhu, J. Song, C. Li, J. Xu, K. Ueda, A. A. Kaminskii, H. Yagi & T. Yanagitani, (2000). Optical Properties and Highly Efficient Laser Oscillation of Nd : YAG Ceramics. *Applied Physics B*, 71 (4), 469-473.
98. A. Lempicki, C. Brecher, H. Lingertat, S. R. Miller, J. Glodo & V. K. Sarin, (2008). A Ceramic Version of the LSO Scintillator. *IEEE Transactions on Nuclear Science*, 55 (3), 1148-1151.
99. Y. K. Kim, H. K. Kim, D. K. Kim & G. S. Cho, (2004). Synthesis of Eu-doped $(Gd,Y)_2O_3$ Transparent Optical Ceramic Scintillator. *Journal of Materials Research*, 19 (2), 413-416.

100. G. C. Wei, (2005). Transparent Ceramic Lamp Envelope Materials. *Journal of Physics D*, 38 (17), 3057-3065.
101. J. M. Sands, P. J. Patel, P. G. Dehmer, A. J. Hsieh & M. C. Boyce, (2004). Protecting the Future Force: Transparent Materials Safeguard the Army's Vision. *AMPTIAC Quart.*, 8, 28-36.
102. I. Yamashita, H. Nagayama & K. Tsukuma, (2008). Transmission Properties of Translucent Polycrystalline Alumina. *Journal of the American Ceramic Society*, 91 (8), 2611-2616.
103. J. P. Cheng, D. Agrawal, Y. J. Zhang & R. Roy, (2002). Microwave Sintering of Transparent Alumina. *Materials Letters*, 56 (4), 587-592.
104. R. Apetz & M. P. B. van Bruggen, (2003). Transparent Alumina: A Light-scattering Model. *Journal of the American Ceramic Society*, 86 (3), 480-486.
105. J. G. J. Peelen & Metselaa.R, (1974). Light-scattering by Pores in Polycrystalline Materials - transmission Properties of Alumina. *Journal of Applied Physics*, 45 (1), 216-220.
106. V. Lupei, A. Lupei & A. Ikesue, (2008). Transparent Polycrystalline Ceramic Laser Materials. *Optical Materials*, 30 (11), 1781-1786.
107. I. Shoji, S. Kurimura, Y. Sato, T. Taira, A. Ikesue & K. Yoshida, (2000). Optical Properties and Laser Characteristics of Highly Nd^{3+}-doped $Y_3Al_5O_{12}$ Ceramics. *Applied Physics Letters*, 77 (7), 939-941.
108. J. Kong, J. Lu, K. Takaichi, T. Uematsu, K. Ueda, D. Y. Tang, D. Y. Shen, H. Yagi, T. Yanagitani & A. A. Kaminskii, (2003). Diode-pumped Yb : Y_2O_3 Ceramic Laser. *Applied Physics Letters*, 82 (16), 2556-2558.
109. A. Shirakawa, K. Takaichi, H. Yagi, J. F. Bisson, J. Lu, M. Musha & K. Ueda, (2003). Diode-pumped Mode-locked Yb^{3+}: Y_2O_3 Ceramic Laser. *Optics Express*, 11 (22), 2911-2916.
110. J. Lu, J. F. Bisson, K. Takaichi, T. Uematsu, A. Shirakawa, M. Musha, K. Ueda, H. Yagi, T. Yanagitani & A. A. Kaminskii, (2003). Yb^{3+}: Sc_2O_3 Ceramic Laser. *Applied Physics Letters*, 83 (6), 1101-1103.
111. J. Lu, K. Takaichi, T. Uematsu, A. Shirakawa, M. Musha, K. Ueda, H. Yagi, T. Yanagitani & A. A. Kaminskii, (2002). Promising Ceramic Laser Material: Highly Transparent Nd^{3+}: Lu_2O_3 Ceramic. *Applied Physics Letters*, 81 (23), 4324-4326.
112. J. Saikawa, Y. Sato, T. Taira & A. Ikesue, (2007). Femtosecond Yb^{3+}-doped $Y_3(Sc_{0.5}Al_{0.5})_2O_{12}$ Ceramic Laser. *Optical Materials*, 29 (10), 1283-1288.
113. D. J. Wisniewski, L. A. Boatner, J. S. Neal, G. E. Jellison, J. O. Ramey, A. North, M. Wisniewska, A. E. Payzant, J. Y. Howe, A. Lempicki, C. Brecher & J. Glodo, (2008). Development of Novel Polycrystalline Ceramic Scintillators. *IEEE Transactions on Nuclear Science*, 55 (3), 1501-1508.
114. S. K. Dutta & G. E. Gazza, (1969). Transparent Y_2O_3 by Hot-pressing. *Materials Research Bulletin*, 4 (11), 791-&.
115. G. E. Gazza, D. Roderick & B. Levine, (1971). Transparent Sc_2O_3 by Hot-pressing. *Journal of Materials Science*, 6 (8), 1137-1139.
116. U. Peuchert, Y. Okano, Y. Menke, S. Reichel & A. Ikesue, (2009). Transparent Cubic-ZrO_2 Ceramics for Application as Optical Lenses. *Journal of the European Ceramic Society*, 29 (2), 283-291.
117. K. Itatani, T. Tsujimoto & A. Kishimoto, (2006). Thermal and Optical Properties of Transparent Magnesium Oxide Ceramics Fabricated by Post Hot-isostatic Pressing. *Journal of the European Ceramic Society*, 26 (4-5), 639-645.
118. J. Sanghera, S. Bayya, G. Villalobos, W. Kim, J. Frantz, B. Shaw, B. Sadowski, R. Miklos, C. Baker, M. Hunt, I. Aggarwal, F. Kung, D. Reicher, S. Peplinski, A. Ogloza, P. Langston, C. Lamar, P. Varmette, M. Dubinskiy & L. DeSandre, (2011). Transparent Ceramics for High-energy Laser Systems. *Optical Materials*, 33 (3), 511-518.

119. A. Ikesue & K. Kamata, (1996). Microstructure and Optical Properties of Hot Isostatically Pressed Nd:YAC Ceramics. *Journal of the American Ceramic Society*, 79 (7), 1927-1933.
120. R. Chaim, Z. Shen & M. Nygren, (2004). Transparent Nanocrystalline MgO by Rapid and Low-temperature Spark Plasma Sintering. *Journal of Materials Research*, 19 (9), 2527-2531.
121. M. Stuer, Z. Zhao, U. Aschauser & P. Bowen, (2009). Transparent Polycrystalline Alumina Using Spark Plasma Sintering: Effect of Mg, Y and La Doping. *Journal of European Ceramic Society*, 30 (6), 1335-1343.
122. Y. Zhou, K. Hirao, Y. Yamauchi & S. Kanzaki, (2004). Densification and Grain Growth in Pulse Electric Current Sintering of Alumina. *Journal of European Ceramic Society*, 24 (12), 3465-3470.
123. Z. J. Shen, M. Johnsson, Z. Zhao & M. Nygren, (2002). Spark Plasma Sintering of Alumina. *Journal of the American Ceramic Society*, 85 (8), 1921-1927.
124. R. Chaim, R. Marder-Jaeckel & Z. Shen, (2006). Transparent YAG Ceramics by Surface Softening of Nanoparticles in Spark Plasma Sintering. *Materials Science and Engineering A*, 429, 74-78.

Chapter 3 Synthesis of $Sr_2Y_8(SiO_4)_6O_2$ and the characterization of its crystal structure

3.1 Introduction

Numerous applications of apatite materials in catalysis,[1] environmental remediation [2] and biomedical industries [3] have been reported. The most common space group for apatite materials is $P6_3/m$ [4] and the general formula can be expressed as $A^I_4A^{II}_6(BO_4)_6X_2$. One main reason for the many applications of apatite materials is the considerable tolerance of apatite structure to incorporate diverse cations into it.[5] Two crystallographic sites A^I (4f in Wycoff symbol) and A^{II} (6h in Wycoff symbol) can incorporate cations of alkali or rare-earth, B position is usually occupied by cations with high valence state such as phosphorous, silicon, vanadium or boron and the anion site X is accommodated by halogen, hydroxyl or oxygen. In order to interpret the crystal structural evolution of various apatite materials and offer instructions for the applications like the environmental remediation, systematic studies of the crystal structures have been reported.[6-11] White and Dong studied the structural derivation of apatite and indicated that the twist angle φ obtained from the crystal structures is an important parameter to interpret the distortion and evolution of the apatite structures.[4,12] The authors studied a series of phosphate and arsenate apatites with one type of cation in both A^I and A^{II} sites and indicated that the twist angle φ varies linearly and inversely with the average ionic radius of the compounds.

Recently, the silicate oxyapatite, one family of apatite, received much attention due to its high melting point (~2000 ºC) and good chemical stabilities.[13] Many applications and studies of silicate oxyapatite have been reported. In the current study, we focused on one silicate oxyapatite $Sr_2Y_8(SiO_4)_6O_2$ (SYS) which was used as the laser host lattice.[14-17] Studies confirmed that laser performances are influenced by the crystal structure of the host.[16,18] However, there is no detailed structural data of $Sr_2Y_8(SiO_4)_6O_2$ available so far.

Therefore, in this chapter, pure phase $Sr_2Y_8(SiO_4)_6O_2$ powders are synthesized and characterized. For our synthesis process, two methods, i.e. solid state reaction and sol-gel method, are employed. In the solid state reaction, two types of raw materials, the commercial powders and the synthetic nano-sized powders, are used for comparison. In the sol-gel method, the influence of the amount of H_2O on the phase purity of apatite is studied. After the synthesis, the crystal structure of $Sr_2Y_8(SiO_4)_6O_2$ is studied by X-ray diffraction (XRD), Rietveld refinement and high resolution transmission electron microscopy (HRTEM). Based on these results, the $Sr_2Y_8(SiO_4)_6O_2$ crystal structure is analyzed and demonstrated for the first time. This is a very fundamental understanding and it helps to resolve similar but more complex apatite structures doped with rare earth or other elements. Furthermore, a systematic study of reported silicate oxyapatite is conducted. The concept of twist angle and a new term of effective ionic radius are applied to analyze these silicate oxyapatites structures.

3.2 Experimental procedures

3.2.1. Solid state reaction

The main steps of solid state reaction are mixing the starting materials and heating the mixture to the desired temperature. In our study, yttrium oxide Y_2O_3, strontium carbonate $SrCO_3$ and silica gel were chosen as the starting materials. The strontium carbonate and silica gel were commercially available ($SrCO_3$ (>99.0%, Alfa Aesar), silica gel 60 (>99.0%, Fluka)). The powders of yttrium oxide were the major constituents of the starting powders according to stoichiometric calculation and its properties certainly would affect the phase formation. Therefore, two different yttrium oxide powders, the commercial Y_2O_3 (99.9%, Alfa Aesar, ~1 μm) and the synthetic nano-sized Y_2O_3, were compared.

3.2.1.1 Synthesis of nano-sized Y_2O_3

0.5 mol/L $Y(NO_3)_3$ and 2.5 mol/L NH_4HCO_3 solutions were obtained by dissolving $Y(NO_3)_3$ (>99.9%, Aldrich) and NH_4HCO_3 (>99.0%, Fluka) powders into deionized water respectively. Then NH_4HCO_3 was slowly dripped into $Y(NO_3)_3$ solution with vigorous stirring and white precipitates appeared according to the following reaction:

$$2Y(NO_3)_3 + 6NH_4HCO_3 \rightarrow Y_2(CO_3)_3(H_2O)_2 \downarrow + 6NH_4NO_3 + H_2O + 3CO_2\uparrow \quad \text{Equation 3-1}$$

During the precipitation, 10% excessive NH_4HCO_3 over the stoichiometric amounts was added into $Y(NO_3)_3$ solution in order to fully precipitate the yttrium species.

The precipitates were washed twice by water and ethanol each followed by drying at 70 ºC in oven. Finally they were calcined at higher temperatures for 4 hours with heating rate 5 ºC/min. Thermal gravimetric and differential thermal analysis (TG-DTA) was used to determine the calcination temperature.

3.2.1.2 Synthesis of $Sr_2Y_8(SiO_4)_6O_2$

Commercial (99.9%, Alfa Aesar, ~1 μm) and synthetic Y_2O_3 were mixed with silica gel 60 (>99.0%, Fluka), $SrCO_3$ (>99.0%, Alfa Aesar) respectively according to the stoichiometry of the formula $Sr_2Y_8(SiO_4)_6O_2$. Each batch of mixture was 4 grams. In order to mix the raw powders homogeneously, the mixture was immersed in ethanol and horizontal ball milled for 12 hours, and then dried at 70 ºC in oven overnight. The as-received mixtures were sintered in the furnace at 1200, 1300 and 1400 ºC for 6 hours with heating rate 5 ºC/min.

3.2.2 Sol gel method

According to the sol-gel synthesis of lanthanum silicate oxyapatites reported by Celerier *et al.*,[19] 15 g $La(NO_3)_3 \cdot 6H_2O$ was mixed with 10 ml acetic acid, 10 ml ethanol and stoichiometric tetraethyl orthosilicate (TEOS) to produce about 0.0034 mol final product. In the current study, the amount of $Sr_2Y_8(SiO_4)_6O_2$ powders produced by each sol-gel reaction was 0.002 mol, so 6 ml acetic acid and 6 ml ethanol were used in the synthesis. Strontium nitrate $Sr(NO_3)_3$ (>99.9%, Fluka), hexahydrate yttrium nitrate $Y(NO_3)_3 \cdot 6H_2O$ (>99.9%, Sigma-Aldrich) were used as the starting materials. The solubility of $La(NO_3)_3 \cdot 6H_2O$ in ethanol is high so it is possible to synthesize lanthanum silicate oxyapatite in a water-free environment, but those of $Sr(NO_3)_3$ and $Y(NO_3)_3 \cdot 6H_2O$ are low [20] and water is needed as a solvent in sol-gel synthesis. The influence of the amount of water added during reaction on the purity of apatite phase was studied. The detailed procedures were as follow:

0.8466 g $Sr(NO_3)_3$, 6.128 g $Y(NO_3)_3 \cdot 6H_2O$ were mixed with 2.66 ml TEOS (>99.99%, Sigma-Aldrich), 6 ml absolute ethanol, 6 ml acetic acid and deionized water. Three different volumes of water, i.e. 6, 9, 12 ml were compared. The mixture was refluxed at 110 ºC and then it became a transparent solution. A translucent viscous gel was obtained

by continuous refluxing and stirring for 4 hours. The gel was dried at 80 ºC overnight and heated at 700 ºC for 4 hours to remove the unwanted organic species. Then the product was ground and followed by the heat treatment at 1400 ºC for 6 hours. It was difficult to obtain a transparent solution during refluxing if the water used was less than 6 ml, which meant strontium and yttrium species were unable to be dissolved and cannot link to the network resulted from condensation process. Therefore, the results with water volume less than 6 ml are not suitable for further experiments.

3.2.3 Characterizations

X-ray diffraction (XRD, Shimadzu 6000, Kyoto, Japan) with Cu*K*α radiation was performed at 40 kV and 30 mA to analyze the phase compositions. The scan speed was 2˚/min with a step size 0.02°. In order to determine the details of the crystal structure, Rietveld refinement was performed on the as-received XRD patterns by software TOPAS (version 3.0, Bruker AXS, Karlsruhe, Germany). Since no special structural details about $Sr_2Y_8(SiO_4)_6O_2$ were known except for its apatite structure-type, one silicate oxyapatite $NaY_9(SiO_4)O_2$ apatite (ICSD #27191) was used as the original structure model. During the refinement, the parameters of background (chebychev function), lattice constants, crystal size, atom positions, site occupancies and global thermal parameters were refined successively.

Scanning electron microscopy (SEM, JSM-6360, Japan) with 15 kV operating voltage was used to investigate the morphologies of commercial and synthetic Y_2O_3 powders. Before SEM observation, the samples were prepared by dispersing the powders in ethanol with the assistance of ultrasonication for 10 minutes. After that, the samples were dripped on the silicon wafer and heated at 80 ºC to dry. In order to investigate the local structure of $Sr_2Y_8(SiO_4)_6O_2$ and verify the results from XRD refinement, high resolution transmission electron microscopy (HRTEM) images and selected area diffraction patterns

(SAED) of $Sr_2Y_8(SiO_4)_6O_2$ were collected by a JEOL JEM 2100F transmission electron microscopes (Cs = 0.5 mm, accelerating voltage = 200 kV, Scherzer defocus ≈ −43 nm).

3.2.4 Analysis of the crystal structures of silicate oxyapatites

Including the data in the presence of study and the ones reported before, seventeen silicate oxyapatites [21-25] all with $P6_3/m$ symmetry were summarized in this chapter (Table 3-4) and the structural evolution was studied. The samples were either powders or single crystals. The variations of the crystal structures are only attributed to the different cations occupying the A^I and A^{II} sites since all the chosen compounds has a general formula of $A^I{}_4A^{II}{}_6(SiO_4)_6O_2$. In many literatures the average ionic size was used to measure the structural variations, though it was unable to distinguish the effect from different sites. In order to emphasize different effects of A^I and A^{II} on the silicate oxyapatite crystal structures, a new parameter called the effective ionic radius is proposed, and it is defined as:

$$r_{eff}^{A^m} = \sum_{i=1}^{n} r_i^{A^m} \times \eta_i^{A^m} \quad \text{(m = I or II)} \qquad \text{Equation 3-2}$$

where $r_{eff}^{A^I}$ (or $r_{eff}^{A^{II}}$) is the effective ionic radius of A^I (or A^{II}), $r_i^{A^I}$ (or $r_i^{A^{II}}$) is the ionic radius of atom (or vacancy) *i* at A^I (or A^{II}) and $\eta_i^{A^I}$ (or $\eta_i^{A^{II}}$) is the occupancy of the atom (or vacancy) *i* at A^I (or A^{II}). The radius of a vacancy is arbitrarily considered as zero.

According to Mercier *et al.*,[8] the twist angles of the silicate oxyapatite structures can be calculated from the atomic positions. The twist angles of eight candidates ($Sr_2RE_8(SiO_4)_6O_2$ (RE = La, Y or Nd), $RE_{9.33}(SiO_4)_6O_2$ (RE = La, Nd, Gd), $LiY_9(SiO_4)_6O_2$ and $NaY_9(SiO_4)_6O_2$) with atomic positions available were calculated and compared.

3.3 Results and discussion

3.3.1 Characterization of the synthetic Y_2O_3

In accordance with Equation 3-1, the precipitates are confirmed to be $Y_2(CO_3)_3(H_2O)_2$ by X-ray diffraction analysis (Figure 3-1).

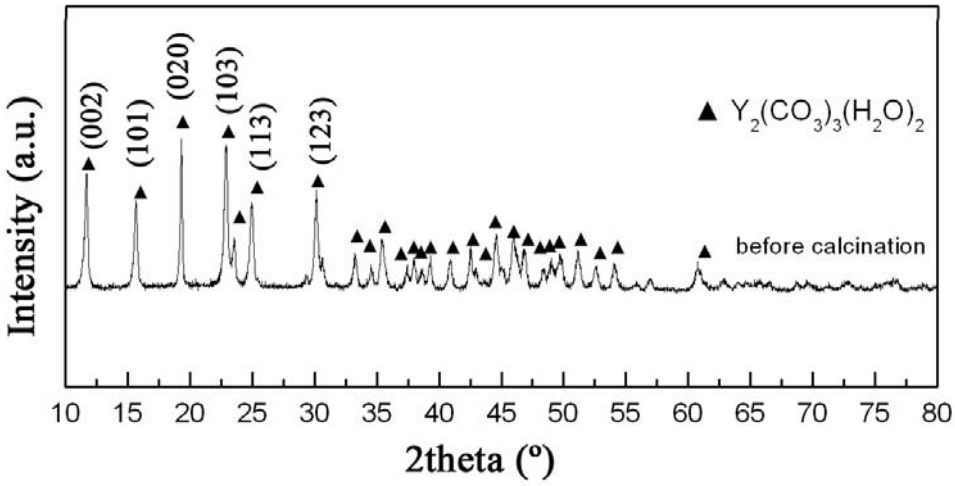

Figure 3-1 XRD pattern of the dried precipitates, which confirmed to be $Y_2(CO_3)_3(H_2O)_2$

In the TG curve of the precipitates (Figure 3-2), weight decreasing occurs with the increase of the temperature until the temperature reaches about 620 ºC. In the DTA curve, the endothermic peak at 80 ºC corresponds to the dehydration process of $Y_2(CO_3)_3(H_2O)_2$, or $Y_2(CO_3)_3(H_2O)_2 \rightarrow Y_2(CO_3)_3 + 2H_2O \uparrow$, and the one at 140 ºC reflects the decomposition of the residual ammonium species. The decomposition of $Y_2(CO_3)_3$ occurs at about 340 ºC as indicated in the DTA curve. This decomposition process does not complete until the temperature reaches 620 ºC as no more decrease of the weight occurs in TG curve. The endothermic peak at highest temperature (~ 600 ºC) is related to the crystallization of Y_2O_3. The constant exothermic trend in the DTA profile is caused by the machine.

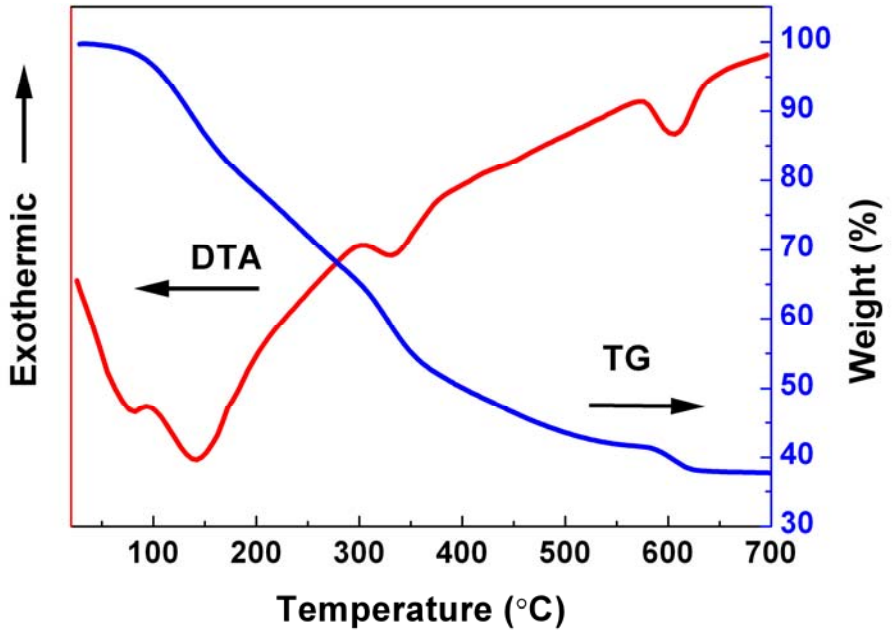

Figure 3-2 TG-DTA profile of the $Y_2(CO_3)_3(H_2O)_2$ precipitates up to 700 ºC

The precipitates are calcined at three different temperatures 500 ºC, 700 ºC and 900 ºC and the XRD patterns of calcined samples are shown in Figure 3-3. The formation of pure cubic-Y_2O_3 phase is confirmed by the Rietveld refinement of these XRD patterns and the crystallite sizes obtained from refinement are 15, 36 and 64 nm respectively for samples calcined at 500 ºC, 700 ºC and 900 ºC. Small crystallite size and broad XRD peaks indicate poor crystallization with a possible existence of amorphous materials in the sample calcined at 500 ºC . The well crystallized Y_2O_3 powders are obtained after 700 ºC calcination. Indeed, it is consistent with the analysis of TG-DTA which suggests the crystallization temperature of Y_2O_3 is around 600 ºC. Higher temperature calcination at 900 ºC enlarges the crystal size and leads to narrower peaks in the XRD pattern. In the experiments hereafter, Y_2O_3 powders calcined at 700 ºC are used as the nano-size and high crystallinity.

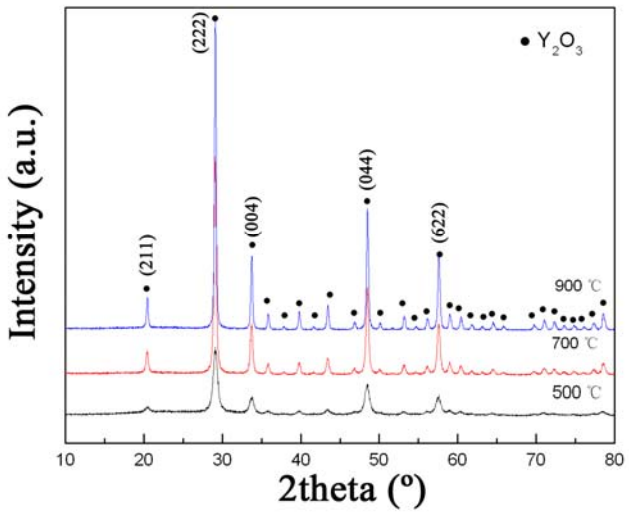

Figure 3-3 XRD patterns of the precipitates with calcination temperatures at 500 ºC, 700 ºC, 900 ºC, showing the formation of pure Y_2O_3 phase.

The morphologies of commercial and synthetic Y_2O_3 powders after ultrasonic dispersion are observed by SEM as shown in Figure 3-4. As compared to the commercial Y_2O_3 powders, the synthetic ones are more homogenous and much smaller, i.e. about 80−100 nm in size. In the solid state reaction, raw powders with the small and uniform size are preferred due to their large surface area and high reactivity. Moreover, the yield of this precipitation method to produce such uniform Y_2O_3 powder is about 15 gram once, which is sufficient to support subsequent works.

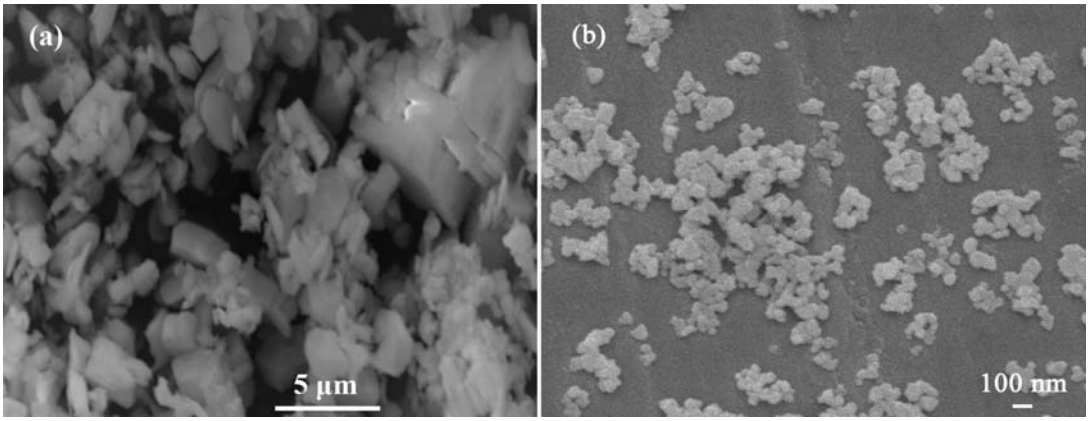

Figure 3-4 Morphologies of Y_2O_3 powders: (a) commercial and (b) synthetic powders.

3.3.2 Purity of $Sr_2Y_8(SiO_4)_6O_2$ synthesized from solid state reaction

XRD patterns of the samples synthesized from the commercial Y_2O_3 with different heating temperatures are shown in Figure 3-5. Although the main phase in the as-reacted sample is $Sr_2Y_8(SiO_4)_6O_2$ apatite, extra peaks belonging to Y_2O_3, SiO_2 and one unidentified phase are persistent in all the samples with different heating temperatures even the one with prolonged reaction duration at 1400 ºC, indicating the incomplete reaction of the raw materials. The unidentified phase could be some strontium compound since the starting materials are mixed stoichiometrically. However, due to the small amount of this impurity and probably some overlapping of the XRD peaks with other phases, it is difficult to determine the structure. The Rietveld refinement results of the XRD pattern from the one heated at 1400 ºC for 18 hours (Figure 3-6) quantitatively show that there are 88.7 wt% apatite, 3.1 wt% Y_2O_3 and 8.2 wt% SiO_2 in the sample. The existence of impurities and unreacted starting materials is due to the inhomogeneous size distribution and low reactivity of commercial Y_2O_3 starting powder

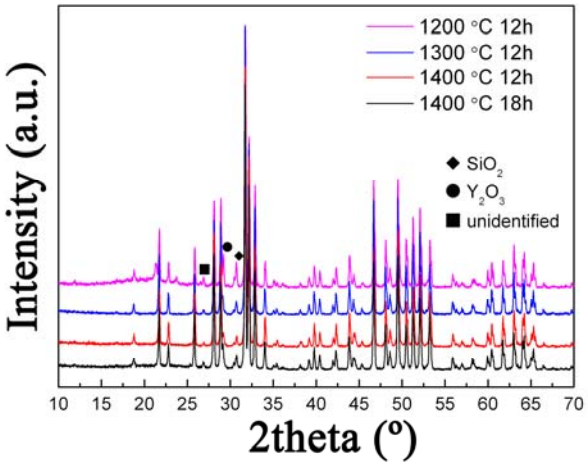

Figure 3-5 XRD patterns of samples synthesized from commercial Y_2O_3 with different heating temperatures and durations

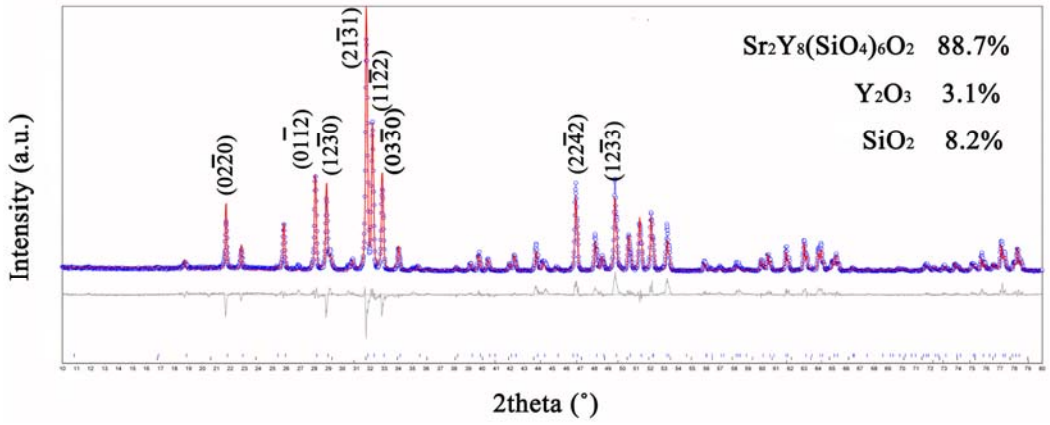

Figure 3-6 XRD refinement of the sample synthesized from commercial Y_2O_3. The sample is heated at 1400 °C for 18 hours. The major peaks of phase $Sr_2Y_8(SiO_4)_6O_2$ are indexed.

The samples synthesized by the synthetic nano-sized Y_2O_3 powder and commercial $SrCO_3$ and silica gel contain less impurities as the XRD peaks of impurities in Figure 3-7 are lower than those in Figure 3-5. When the heating temperature reaches 1400 ºC, the XRD peaks from impurities disappear and the pure phase of $Sr_2Y_8(SiO_4)_6O_2$ apatite is obtained. Moreover, the pure apatite phase still maintained with shortened reaction duration as 6 hours (Figure 3-8). All these results indicate the synthetic nano-sized Y_2O_3 powders have high reactivity and are in favor of the formation of pure $Sr_2Y_8(SiO_4)_6O_2$ phase. All the solid state synthesis of $Sr_2Y_8(SiO_4)_6O_2$ hereafter are conducted by mixing synthetic nano-sized Y_2O_3 powders, commercial $SrCO_3$ and silica gel with reaction at 1400 ºC for 6 hours.

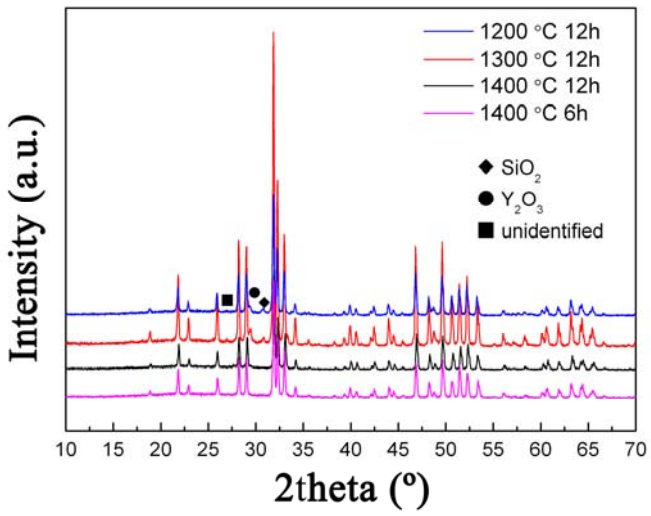

Figure 3-7 XRD patterns of samples synthesized from synthetic nano-sized Y_2O_3 with different heating temperatures and durations

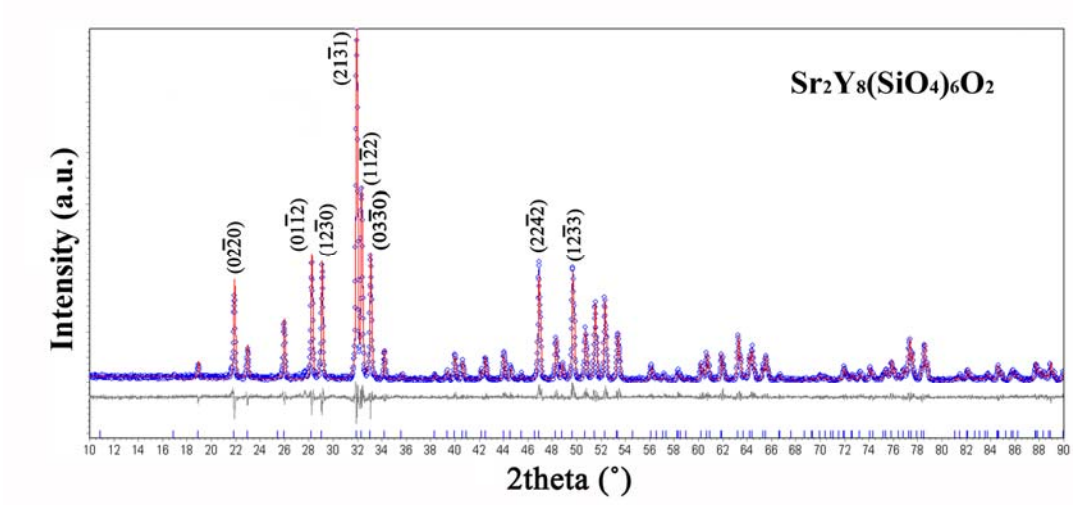

Figure 3-8 XRD refinement of the sample synthesized from synthetic nano-sized Y_2O_3, exhibiting the pure phase of $Sr_2Y_8(SiO_4)_6O_2$. The sample is heated at 1400 °C for 6 hours.

3.3.3 Sol-gel method

The XRD patterns of the sol-gel synthesized samples are shown in Figure 3-9. Obviously, the samples with 12 or 9 ml water added during synthesis have impurities. The results from Rietveld refinement indicate that the impurities might be Y_2O_3, SiO_2, Sr_2SiO_4 and Y_2SiO_5. The weight fractions of the silicate oxyapatite phase are about 85%

for the sample synthesized with 12 ml water and 90% for one with 9 ml water (Figure 3-10). Only the one with 6 ml water added shows the formation of pure apatite phase. Celerier *et al.* [19] observed similar phenomenon and suggested that the large volume of water would hydrolyze the siloxane bond resulted from condensation process and lead to the inhomogeneity in the polymerized network. Moreover, impurities still appear in the sample obtained from the gel with 6 ml water and heating at 1300 ºC, which suggests that 1400 ºC is the phase formation temperature of $Sr_2Y_8(SiO_4)_6O_2$ and heating at lower temperature is not favorable to the pure apatite formation.

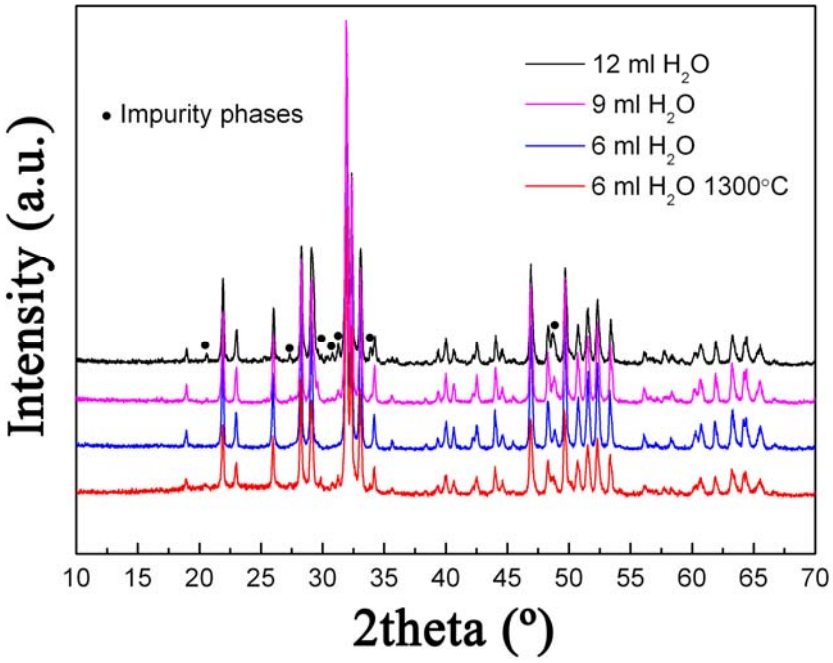

Figure 3-9 XRD patterns of the sol-gel synthesized samples with different amounts of water added and different tempertatures. The black, purple and blue patterns represent the sample synthesized at 1400 ºC with 12, 9 and 6 ml H_2O respectively. The red pattern corresponds to the sample synthesized at 1300 ºC with 6 ml H_2O. Only the one with 6 ml H_2O and 1400 ºC heating is pure phase.

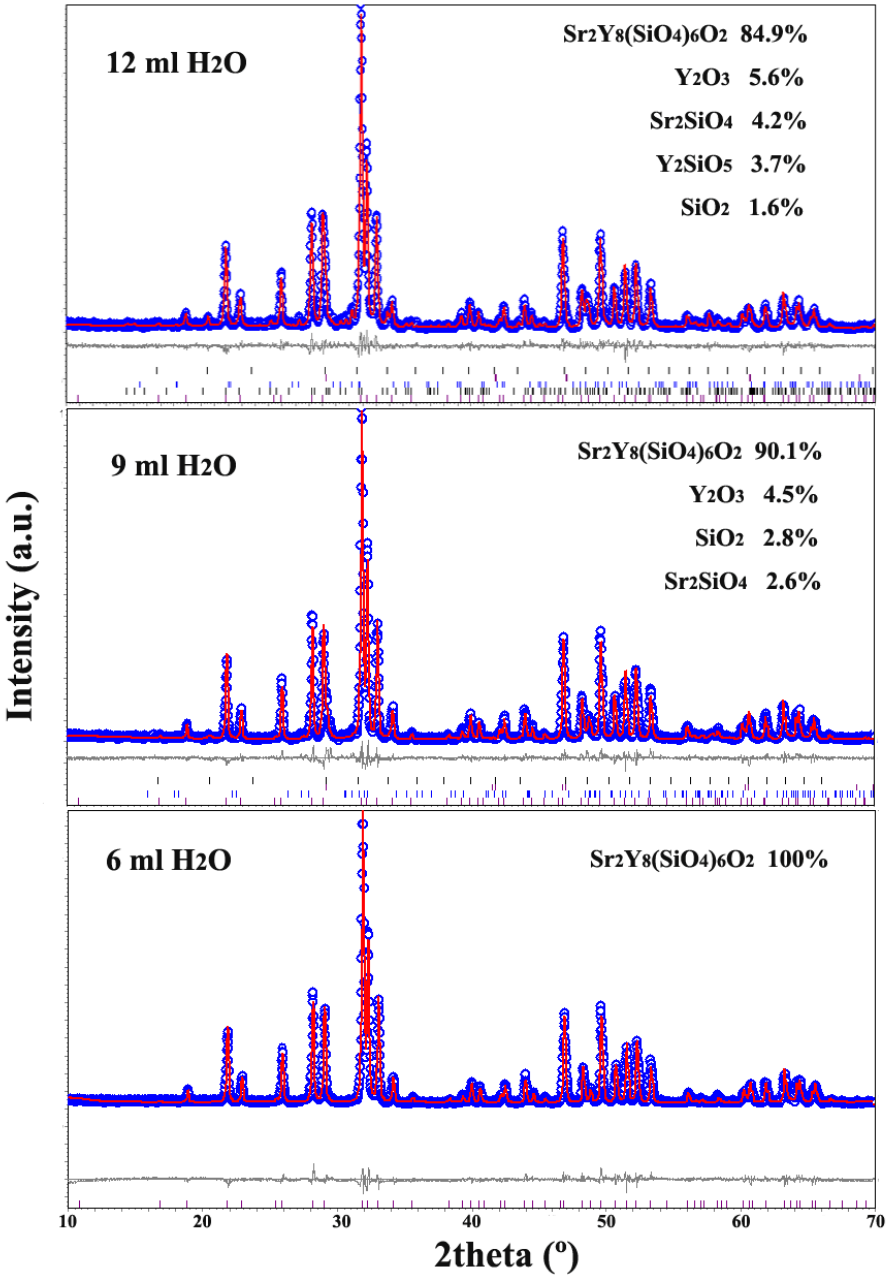

Figure 3-10 Rietveld refinement results of the samples from sol gel method with 12ml, 9ml and 6ml H_2O. The weight percentages of compositions are indicated.

The morphologies of the powders synthesized from the solid state reaction and sol-gel method are compared in Figure 3-11. The particles obtained from solid state reaction are homogeneous with sizes in sub-micrometer scale. The nano-sized Y_2O_3 powders used in solid state reaction ensure the high homogeneity of the silicate oxyapatite powders. The powders synthesized from the sol-gel method are irregularly shaped with large difference

in the particle size, which may be due to the large polymerized networks resulted from the rapid condensation process during sol-gel synthesis.

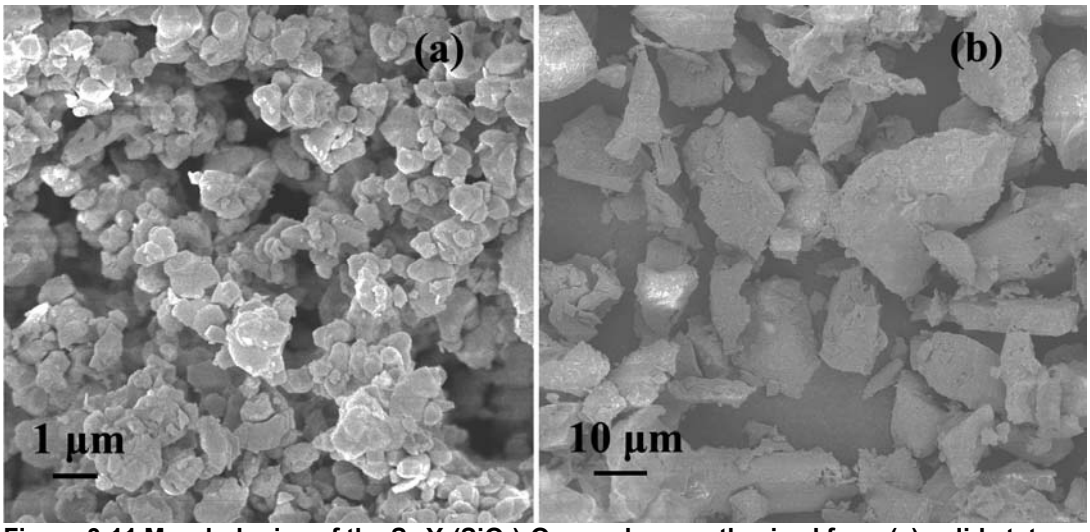

Figure 3-11 Morphologies of the $Sr_2Y_8(SiO_4)_6O_2$ powders synthesized from (a) solid state reaction and (b) sol-gel method.

3.3.4 Crystal structure of $Sr_2Y_8(SiO_4)_6O_2$

The Rietveld refinement results from both solid state and sol-gel synthesis are identical so in this section only the results from solid state reaction are shown. Several space groups other than $P6_3/m$ have been tested but the refinement results are diverged after some calculation cycles. Therefore, it is believed that the space group of $Sr_2Y_8(SiO_4)_6O_2$ is $P6_3/m$. In order to reveal the distribution of Sr^{2+} and Y^{3+} cations among A^I and A^{II} sites, site occupancies at A^I and A^{II} sites are refined. Assuming occupancies of Y^{3+} and Sr^{2+} at A^{II} are x and 1-x. Considering the multiplicity of A^I and A^{II} are 4 and 6 respectively, the occupancies of Y^{3+} and Sr^{2+} at A^I site is 2-1.5x and 1.5x-1. The refinement results reveal that all Sr^{2+} cations enter A^I sites with rest of A^I sites occupied by Y^{3+}. All of the A^{II} sites are accommodated by Y^{3+}. These results are in accordance with F. Druon's report.[15] The detailed refinement parameters and structural data are shown in Table 3-1, 3-2 and 3-3.

Table 3-1 Crystal structure data and refinement parameters of $Sr_2Y_8(SiO_4)_6O_2$

Phase name	$Sr_2Y_8(SiO_4)_6O_2$
[a] *R*-Bragg	3.961
[b] GOF	1.48
Spacegroup	$P6_3/m$
Cell Mass	1496.630
Cell Volume (Å^3)	524.076(79)
Crystallite Size (nm)	157.6
Crystal Density (g/cm^3)	4.74
Lattice parameters:	
a (Å)	9.3884(6)
c (Å)	6.8657(4)
Z	1
θ range for data collection	10°-90°
Refinement method	full-matrix least-squares on F^2

$$^{a}R_{Bragg} = \frac{\sum \left| I_{k,obs} - I_{k,calc} \right|}{\sum I_{k,obs}}$$

$$^{b}GOF = \frac{R_{wp}}{R_{\exp}} = \sqrt{\frac{\sum w_m (Y_{m,obs} - Y_{m,calc})^2}{M - P}}$$

Where $I_{k,obs}$ and $I_{k,calc}$ are the observed and calculated intensities of the *k*th reflection respectively; R_{wp} is *R*-weighted pattern and R_{exp} is *R*-expected value; w_m is the reciprocal of the variance for each observation; $Y_{m,obs}$ and $Y_{m,calc}$ are the observed and calculated data respectively at data point *m*; *M* is the number of data points and *P* is the number of parameters

Table 3-2 Atomic coordinates in the $Sr_2Y_8(SiO_4)_6O_2$ unit cell

Atom	Site	x	y	z	Occupation
Y/Sr	4f (A^I)	1/3	2/3	0.0008(6)	0.5/0.5
Y/Sr	6h (A^{II})	0.2324(2)	0.9959(4)	1/4	1/0
Si	6h	0.3958(7)	0.3709(7)	1/4	1
O1	6h	0.3139(14)	0.4823(14)	1/4	1
O2	6h	0.5925(14)	0.4767(14)	1/4	1
O3	12i	0.3378(10)	0.2488(10)	0.0659(10)	1
O4	2a	0	0	1/4	1

Table 3-3 Selected bond lengths (Å) and bond angles (°) for $Sr_2Y_8(SiO_4)_6O_2$

Bond lengths of A^I(4f)−O		Bond lengths A^{II}(6h)−O	
A^I−O1 ×3	2.375(11)	A^{II}−O4	2.2014(5)
A^I−O2 ×3	2.489(17)	A^{II}−O3 ×2	2.342(8)
A^I−O3 ×3	2.815(10)	A^{II}−O2	2.378(11)
		A^{II}−O3 ×2	2.422(9)
		A^{II}−O1	2.659(11)
Bond lengths of Si−O		Bond angles of O−Si−O	
Si−O1	1.577(16)	O2−Si−O1	112.5(5)
Si−O2	1.601(13)	O2−Si−O3	108.5(6)
Si−O3 ×2	1.607(7)	O1−Si−O3	111.7(6)
		O3−Si−O3	103.7(7)

Based on the refinement, crystal structure of $Sr_2Y_8(SiO_4)_6O_2$ that consists of Si−O tetrahedra, A^I−O and A^{II}−O polyhedra are displayed in Figure 3-12. The Si−O bonds in the Si−O tetrahedra range from 1.577 Å to 1.607 Å and the mean bond length is 1.598 Å. The O−Si−O bond angles vary from 103.7 º to 111.6 º (Table 3-3). Two parameters are employed to quantitatively study the distortion of the Si−O tetrahedra. One is the bond length distortion [26] known as BLD (the standard deviation from the mean value of the bond length) and the other is tetrahedral angle variance [27] known as TAV (the bond angle deviation from ideal one of 109.5° in tetrahedra). The crystal structure details show that BLD of Si−O in the tetrahedron is 0.77 % and the value of TAV is 10.9 °. As compared to P−O tetrahedra in $Ca_5(PO_4)_6F$ [28] whose BLD and TAV values are 0.20 % and 3.4 ° respectively, Si−O tetrahedra in $Sr_2Y_8(SiO_4)_6O_2$ are more distorted. One rational explanation is that Si^{4+} is larger than P^{5+} (r_{Si4+} = 0.26 Å, r_{P5+} = 0.17 Å) and tends to expand the tetrahedron distortedly. It is not unusual that distorted Si−O tetrahedra exist in the silicate oxyapatites as indicated by Redhammer and Roth.[22] Although Si−O tetrahedra do not link to each other directly, they serve an important function to interconnect polyhedra A^I−O and A^{II}−O. Every Si−O tetrahedron is surrounded by four A^I−O

polyhedra (Figure 3-12b) with two of them sharing an O1 atom with the Si−O tetrahedron. The other two A^I−O polyhedra connect with the Si−O tetrahedron through the O2−O3 edges with the O2 atom as the common point of three polyhedra involved. Among five A^{II}−O polyhedra around each Si−O tetrahedron (Figure 3-12d), one of A^{II}−O polyhedra shares O3−O3 edge with the Si−O tetrahedron while the other four connect to Si−O tetrahedron separately by vertex-sharing.

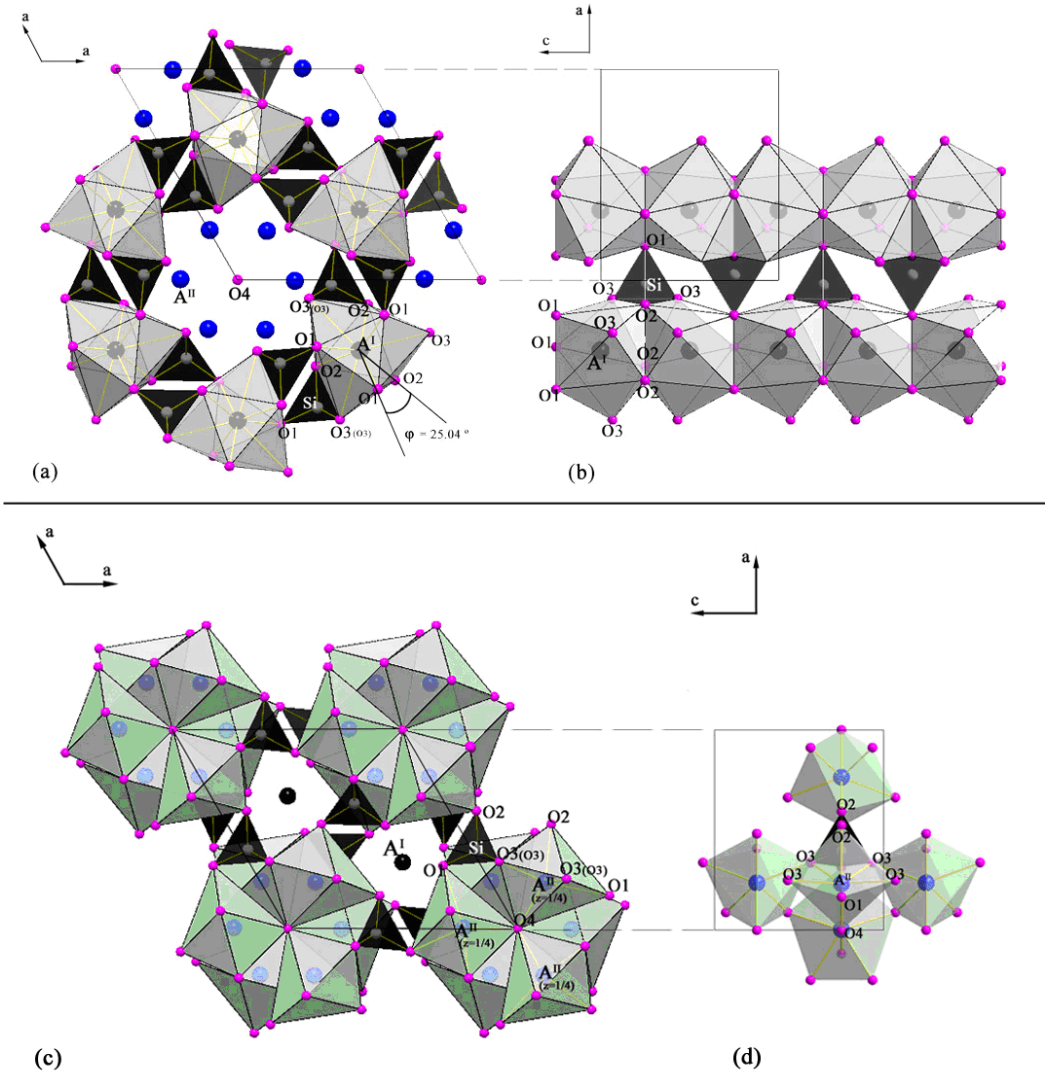

Figure 3-12 The crystal structure of $Sr_2Y_8(SiO_4)_6O_2$. The spheres of black, blue, white and pink colors represent A^I, A^{II}, silicon and oxygen atoms respectively. (a) A^I−O polyhedra (grey) and Si−O tetrahedra (black) configuration along the *c*-axis are shown. The oxygen atoms in the back of Si−O tetrahedra are labeled in bracket. The twist angle φ is also indicated. (b) The two A^I−O polyhedra columns along the *a*-axis are presented. (c) Configuration of the A^{II}−O polyhedra (green) and Si−O tetrahedra (black) is highlighted. Three labeled A^{II} and the central O4 atoms have the same z value (z = ¼). (d) The connection of the Si−O tetrahedra and A^{II}−O polyhedra is shown along *a*-axis direction.

For the A^I–O polyhedra, nine coordinated oxygen atoms lead to a symmetry of C_3 at the central A^I position and construct a tricapped trigonal-prismatic geometry (Figure 3-12a and b). The A^I–O bonds can be divided into three groups: three A^I–O1 bonds with length of 2.375 Å, three A^I–O2 with length of 2.489 Å and three A^I–O3 bonds with 2.815 Å (Table 3-3). In each A^I–O polyhedron, A^IO1_3 and A^IO2_3 form two trigonal prisms that share their vertex at A^I site with two triangle bases parallel to the *ab* plane and normal to the *c*-axis. Along the *c*-axis, these two prisms are obviously twisted respect to each other in the projection of *ab* plane and this is the origin of the parameter twist angle φ which was proposed as a useful tool to analyze the structural evolution and examine the reliability of the structural determination.[4,12] In fact, the twist angle φ (Figure 3-12a) is the projected bond angle of O1−A^I–O2 on the *ab* (0001) plane and it can be calculated based on the position of O1 and O2 atoms. The twist angle for $Sr_2Y_8(SiO_4)_6O_2$ is determined to be 25.04 º. Moreover, polyhedral columns along *c*-axis are formed by face-sharing A^I–O polyhedra. These columns are separated from each other by Si–O tetrahedra.

Seven oxygen atoms (O1×1, O2×1, O3×4 and O4×1) are included in the A^{II}–O polyhedron with A^{II}–O bond lengths from 2.2014 Å to 2.659 Å. The A^{II}–O polyhedron is irregular with pentagonal bipyramidal geometry (Figure 3-12c and d). The O4 atom is a unique feature in the oxyapatite structures. It occupies the 2a position (x = y = 0, z = ¼) and directly connects to three Y^{3+} cations at A^{II} sites. Therefore, the O4 atom cannot be included into any Si–O tetrahedra and the calculation of its sum of the bond valence is about 1.8, which is less than 2. This unsaturated oxygen has considerable impact on the cation occupancy as well as other properties.[29] As compared to fluoride-apatites such as $Ca_5(PO_4)_6F$, F atom substitute the O4 atom and lies at the same 2a position. But regarding to larger anion like Cl^- (r_{Cl^-} = 1.81 Å, $r_{O^{2-}}$ = 1.40 Å and r_{F^-} = 1.33 Å with CN = 6), it will accommodate at 2b (x = y = z = 0) position which is larger than 2a position.[30]

The HRTEM figure and the SAED pattern along $[2\bar{1}\bar{1}0]$ direction are shown in Figure 3-13. According to the images, the d-spacing of $(01\bar{1}0)$ planes and (0001) planes are estimated to be about 8.1 Å and 6.9 Å respectively. These two values can also be derived from the lattice constants as:

$$d_{(01\bar{1}0)} = a \bullet \cos 30^\circ = 9.3384 \bullet \frac{\sqrt{3}}{2} \mathring{A} = 8.0873 \mathring{A} \approx 8.1 \mathring{A}$$
$$d_{(0001)} = c = 6.8657 \mathring{A} \approx 6.9 \mathring{A} \qquad \text{Equation 3-3}$$

The d-spacing values obtained from lattice constants and HRTEM images agree with each other, suggesting that the phase of $Sr_2Y_8(SiO_4)_6O_2$ is obtained and the XRD refinement is reliable.

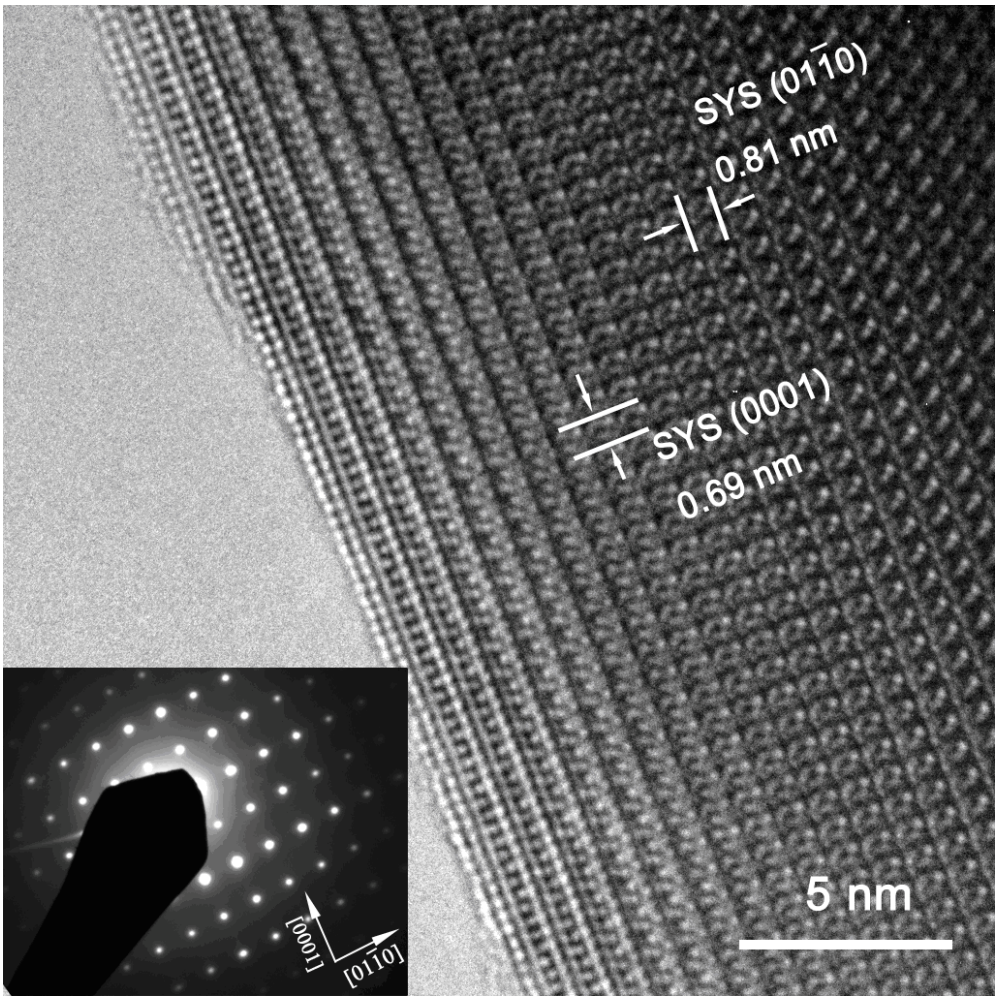

Figure 3-13 HRTEM image of $Sr_2Y_8(SiO_4)_6O_2$ along $[2\bar{1}\bar{1}0]$ zone axis, inset is the selected area diffraction pattern.

3.3.5 Crystal structures of the silicate oxyapatites

The above analysis shows that some crystallographic site is occupied by more than one atom like A^I site in $Sr_2Y_8(SiO_4)_6O_2$. In order to illustrate the effect of different atoms occupying one site on the crystal structure, the concept of effective radius is introduced. The effective ionic radius r_{eff} of one crystallographic site is defined as the sum of the products of ionic radii and the corresponding occupancies in that site. In the current case, there are two different crystallographic sites in the silicate oxyapatites, so

$$r_{eff}^{A^m} = \sum_{i=1}^{n} r_i^{A^m} \times \eta_i^{A^m} \quad \text{(m = I or II)}$$

where $r_{eff}^{A^I}$ (or $r_{eff}^{A^{II}}$) is the effective ionic radius of A^I (or A^{II}), $r_i^{A^I}$ (or $r_i^{A^{II}}$) is the ionic radius of atom (or vacancy) *i* at A^I (or A^{II}) and $\eta_i^{A^I}$ (or $\eta_i^{A^{II}}$) is the occupancy of the atom (or vacancy) *i* at A^I (or A^{II}). The radius of a vacancy is arbitrarily considered as zero. In this section, crystal structures of various silicate oxyapatites are analyzed in terms of the effective radius. Combining with our results of $Sr_2Y_8(SiO_4)_6O_2$, the lattice constants (*a* and *c*) of various silicate oxyapatites measured by other authors [21-25] (Table 3-4) are summarized in Figure 3-14. In the relationship of lattice constants and $r_{eff}^{A^I}$ (Figure 3-14a and b), four groups appear: $Sr_2RE_8(SiO_4)_6O_2$, $NaRE_9(SiO_4)_6O_2$, $LiRE_9(SiO_4)_6O_2$ and $RE_{9.33}(SiO_4)_6O_2$. The lattice constants increase almost linearly with the value of $r_{eff}^{A^I}$ in each group. The small deviations from the linearity may be resulted from different forms of samples (powder or single crystal) or characterization techniques (neutron diffraction or X-ray) listed in Table 3-4. With the purpose to interpret the grouping phenomenon, two groups $NaRE_9(SiO_4)_6O_2$ and $LiRE_9(SiO_4)_6O_2$ are chosen for examples. In order to compensate the smaller Li^+ in A^I position and obtain the same $r_{eff}^{A^I}$ value, the cation RE in $LiRE_9(SiO_4)_6O_2$ should be larger than that in $NaRE_9(SiO_4)_6O_2$. The RE cations not only occupy A^I but also A^{II} position so larger RE cations expand the unit cell significantly.

Consequently $LiRE_9(SiO_4)_6O_2$ group appears on the left of $NaRE_9(SiO_4)_6O_2$. Regarding the fixed cation such as Li^+, Na^+ and Sr^{2+}, it can be concluded more generally that the group with smaller cation appears on the left in Figure 3-14a and b. The lattice constants also linearly vary with the value of $r_{eff}^{A^{II}}$ in each group. However, from Figure 3-14c and d, the separation between each group is not obvious because the size of unit cell is largely determined by RE and A^{II} sites are fully occupied by RE. Based on the above discussion, the relationship between lattice constants and the effective radius is sensitive to the site with multiply cations occupied and it may also act as a tool to determine which site the cation enters. Moreover, the compound $Sm_{10}(SiO_4)_6O_2$ is an interesting case. $Sm_{10}(SiO_4)_6O_2$ can be expressed as $Sm^{2+}{}_2Sm^{3+}{}_8(SiO_4)_6O_2$ because of the co-existence of Sm^{2+} and Sm^{3+} [25] and the size of Sm^{2+} is close to that of Sr^{2+} ($r_{Sm}{}^{2+}$ = 1.19 Å, $r_{Sr}{}^{2+}$ = 1.18 Å). The data for $Sm_{10}(SiO_4)_6O_2$ in Figure 3-14 follow the trends for $Sr_2RE_8(SiO_4)_6O_2$ group, which demonstrate that the relationship between lattice constants and the effective radius is purely size-effect rather than the effect of cation type.

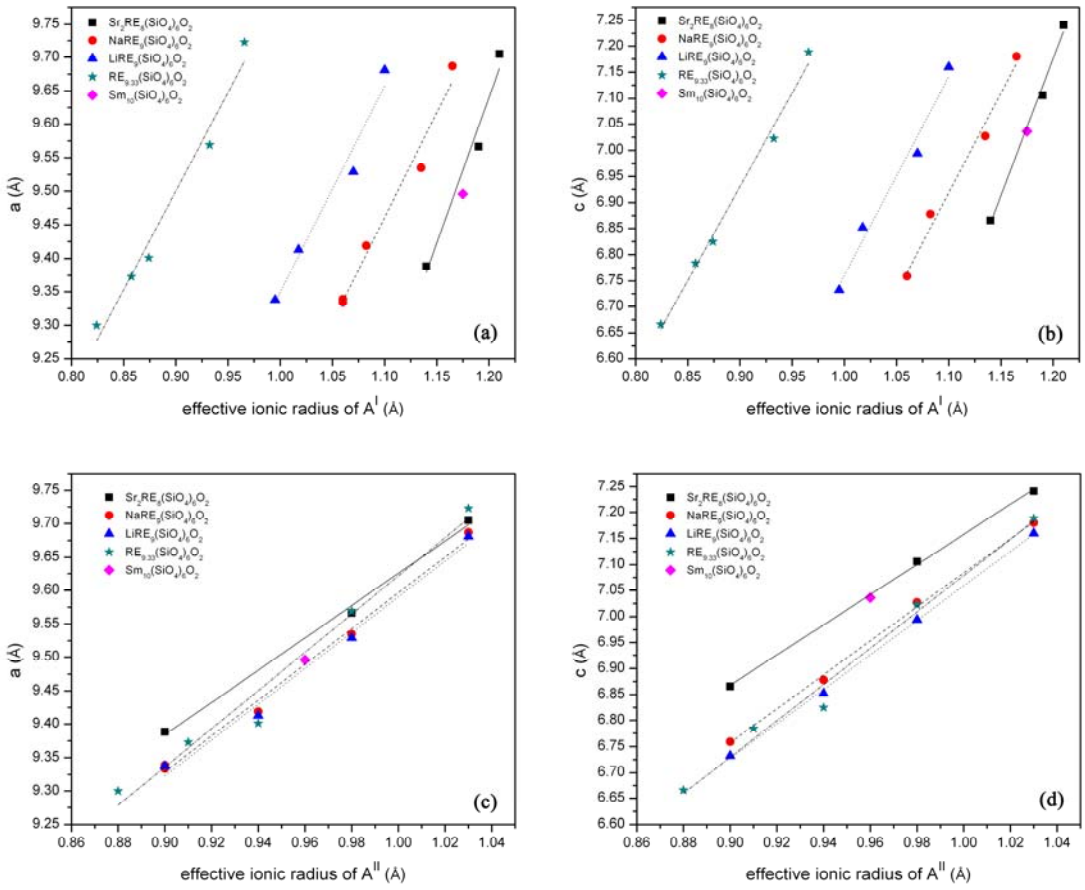

Figure 3-14 The relationship between the effective ionic radius of A^I and the lattice parameters *a* and *c* are shown in (a) and (b) respectively. The relationship between the effective ionic radius of A^{II} and the lattice parameters *a* and *c* are shown in (c) and (d) respectively. The lines of the linear fitting within each group are also shown.

Table 3-4 Crystal structure data of the selected silicate oxyapatites and the calculated effective ionic radius

Compound name	*a* (Å)	*c* (Å)	Occupancy of A^I	Occupan-cy of A^{II}	$r_{eff}^{A^I}$ (Å)	$r_{eff}^{A^{II}}$ (Å)	Refs
[a] $LiY_9(SiO_4)_6O_2$	9.3376	6.7321	Li/Y = 0.25/0.75	Y = 1	0.995	0.9	22
[a] $NaY_9(SiO_4)_6O_2$	9.3386	6.7589	Na/Y = 0.25/0.75	Y = 1	1.06	0.9	
[b] $La_{9.33}(SiO_4)_6O_2$	9.7228	7.1881	Vac/La = 0.167/0.833	La = 1	0.966	1.03	23
[b] $Sr_2La_8(SiO_4)_6O_2$	9.7048	7.2411	Sr/La = 0.5/0.5	La = 1	1.21	1.03	
[b] $Nd_{9.33}(SiO_4)_6O_2$	9.569	7.0225	Vac/Na = 0.167/0.833	Nd = 1	0.932	0.98	
[b] $Sr_2Nd_8(SiO_4)_6O_2$	9.5666	7.1062	Sr/Nd = 0.5/0.5	Nd = 1	1.19	0.98	
[a] $NaY_9(SiO_4)_6O_2$	9.334	6.759	Na/Y = 0.25/0.75	Y = 1	1.06	0.9	24
$Sm_{10}(SiO_4)_6O_2$	9.4959	7.0361	Sm^{2+}/Sm^{3+} = 0.5/0.5	Sm^{3+} = 1	1.175	0.96	25
$Dy_{9.33}(SiO_4)_6O_2$	9.373	6.784	Vac/Dy = 0.167/0.833		0.858	0.91	21
$Gd_{9.33}(SiO_4)_6O_2$	9.401	6.825	Vac/Gd = 0.167/0.833	Dy = 1	0.874	0.94	
$Tm_{9.33}(SiO_4)_6O_2$	9.30	6.666	Vac/Tm = 0.167/0.833	Gd = 1	0.824	0.88	
$LiLa_9(SiO_4)_6O_2$	9.681	7.160	Li/La = 0.25/0.75	Tm = 1	1.10	1.03	
$LiNd_9(SiO_4)_6O_2$	9.529	6.994	Li/Nd = 0.25/0.75	La = 1	1.07	0.98	
$LiGd_9(SiO_4)_6O_2$	9.413	6.852	Li/Gd = 0.25/0.75	Nd = 1	1.018	0.94	
$NaLa_9(SiO_4)_6O_2$	9.687	7.180	Na/La = 0.25/0.75	Gd = 1	1.165	1.03	
$NaNd_9(SiO_4)_6O_2$	9.535	7.027	Na/Nd = 0.25/0.75	La = 1	1.135	0.98	
$NaGd_9(SiO_4)_6O_2$	9.419	6.878	Na/Gd = 0.25/0.75	Nd = 1	1.083	0.94	
				Gd = 1			

a: the samples are single crystals. The rest are powder form.
b: the samples are characterized by the neutron diffraction. The rest are tested by X-ray diffraction.
Vac stands for vacancy.

Moreover, the twist angles φ of the silicate oxyapatites are summarized. The atomic positions are necessary to calculate the twist angle and in these silicate oxyapatites, there are eight suitable candidates: $Sr_2RE_8(SiO_4)_6O_2$ (RE = La, Y or Nd), $RE_{9.33}(SiO_4)_6O_2$ (RE = La, Nd, Gd), $LiY_9(SiO_4)_6O_2$ and $NaY_9(SiO_4)_6O_2$.[21-23] The former two groups are simplified as Sr_2RE_8 and $RE_{9.33}$. The twist angle values are divided into three groups with respect to either $r_{eff}^{A^I}$ or $r_{eff}^{A^{II}}$, as shown in Figure 3-15. Within Sr_2RE_8 or $RE_{9.33}$ group, the

twist angles decrease almost linearly with the increase of the ionic radius, which is consistent with the results reported by White and Dong.[12] When the cation size is small, the A^I–O polyhedron tends to collapse toward octahedron in order to shorten the bonds, leading to a large twist angle. White and Dong [12] also suggested that there would be anomalous deviation from linear relationship between the twist angle and cation size when the structural determination is incorrect. Therefore, the linearity of the Sr_2RE_8 also suggests the refinement of $Sr_2Y_8(SiO_4)_6O_2$ in this work is correct. Small deviations from linearity in Figure 3-15 is due to different measurement methods (e.g. XRD and neutron diffraction) and refinement parameters of the data since the twist angle is sensitive to the atomic positions.

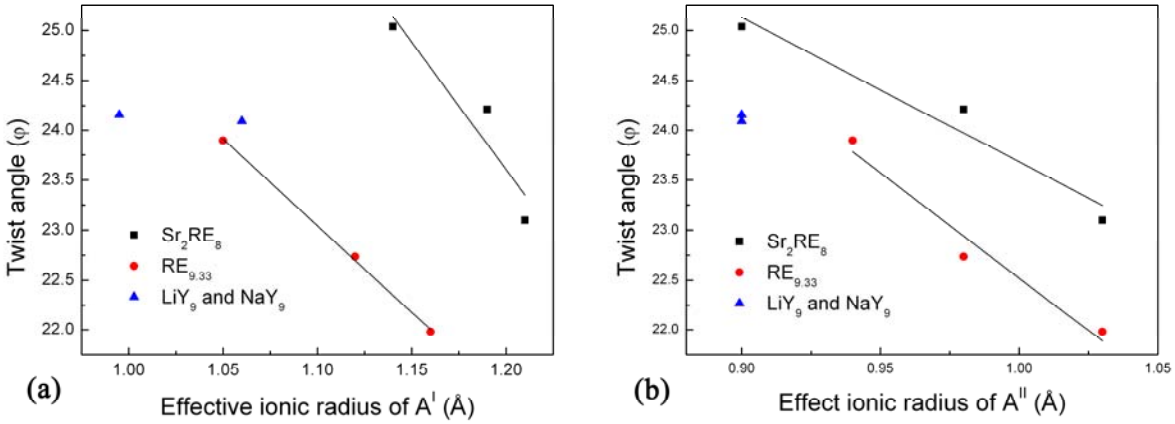

Figure 3-15 Relationship between twist angles and effective ionic radius of AI (a) and AII (b). The linear fitting results of Sr_2RE_8 and $RE_{9.33}$ groups are shown as black line.

3.4 Conclusion

1. Pure $Sr_2Y_8(SiO_4)_6O_2$ powders are synthesized by solid state reaction and sol gel method. In the solid state synthesis, the properties of the starting materials play an important role. Homogeneous nano-sized Y_2O_3 powders obtained from the precipitation method demonstrate that high reactivity and pure $Sr_2Y_8(SiO_4)_6O_2$ powder materials can be produced by using this powder as one of the starting materials in solid state reaction.

2. In the sol-gel method, the amount of water added to dissolve the reactants is crucial. Experimental results showed that 6 ml H_2O is an appropriate amount to synthesize pure $Sr_2Y_8(SiO_4)_6O_2$ materials. Less water is unable to dissolve the reactants and more water would induce impurities in the final product.

3. Silicate oxyapatite $Sr_2Y_8(SiO_4)_6O_2$ with $P6_3/m$ symmetry has lattice constants $a = b =$ 9.3884 Å, and c = 6.8657 Å. Half of A^I sites are occupied by Sr^{2+} while the other half of A^I sites and all the A^{II} sites are filled by Y^{3+}. The twist angle φ is 25.04 ° and this apatite structure is constructed by Si−O, A^I−O and A^{II}−O polyhedra. In each A^{II}−O polyhedron, there is a special oxygen atom called free oxygen O4, which is considerably underbonded.

4. Crystallographic features of the $Sr_2Y_8(SiO_4)_6O_2$ as well as other silicate oxyapatites are compared and summarized. A new parameter called effective ionic radius is introduced, which is able to distinguish different crystallographic sites. The lattice constants and the twist angles are analyzed by utilizing this new parameter and the results are rational.

3.5 References

1. B. M. Choudary, C. Sridhar, M. L. Kantam, G. T. Venkanna & B. Sreedhar, (2005). Design and Evolution of Copper Apatite Catalysts for N-arylation of Heterocycles with Chloro- and Fluoroarenes. *Journal of the American Chemical Society*, 127 (28), 9948-9949.
2. X. B. Chen, J. V. Wright, J. L. Conca & L. M. Peurrung, (1997). Effects of pH on Heavy Metal Sorption on Mineral Apatite. *Environmental Science & Technology*, 31 (3), 624-631.
3. L. L. Hench, (1991). Bioceramics-from Concept to Clinic. *Journal of the American Ceramic Society*, 74 (7), 1487-1510.
4. T. J. White & Z. L. Dong, (2003). Structural Derivation and Crystal Chemistry of Apatites. *Acta Crystallographica Section B*, 59, 1-16.
5. Y. Pan & M. E. Fleet. (2002). Phosphates: Geochemical, Geobiological, and Materials Importance. In M. J. Kohn, J. Rakovan & J. M. Hughes (Eds.), *Reviews in Mineralog and Geochemistry* (pp. 15-29). Washington: Mineralogical Society of America.
6. J. Felsche, (1973). *Structure and Bonding*. Berlin: Springer-Verlag.
7. D. E. C. Corbridge, (1974). *The Structural Chemistry of Phosphorus*. Amsterdam: Elsevier.
8. P. H. J. Mercier, Y. Le Page, P. S. Whitfield & L. D. Mitchell, (2006). Geometrical Parameterization of the Crystal Chemistry of $P6_3/m$ Apatite. II. Precision, Accuracy and Numerical Stability of the Crystal-chemical Rietveld Refinement. *Journal of Applied Crystallography*, 39, 369-375.
9. J. Y. Kim, Z. L. Dong & T. J. White, (2005). Model Apatite Systems for the Stabilization of Toxic Metals: II, Cation and Metalloid Substitutions in Chlorapatites. *Journal of the American Ceramic Society*, 88 (5), 1253-1260.
10. M. I. Kay, R. A. Young & A. S. Posner, (1964). Crystal Structure of Hydroxyapatite. *Nature*, 204 (496), 1050-1052.
11. Z. L. Dong, T. J. White, B. Wei & K. Laursen, (2002). Model Apatite Systems for the Stabilization of Toxic Metals: I, Calcium Lead Vanadate. *Journal of the American Ceramic Society*, 85 (10), 2515-2522.
12. Z. L. Dong & T. J. White, (2004). Calcium-lead Fluoro-vanadinite Apatites. I. Disequilibrium Structures. *Acta Crystallographica Section B*, 60, 138-145.
13. K. B. Steinbruegge, T. Henningsen, R. H. Hopkins, R. Mazelsky, N. T. Melamed, E. P. Riedel & G. W. Roland, (1972). Laser Properties of Nd^{+3} and Ho^{+3} Doped Crystals with Apatite Structure. *Applied Optics*, 11 (5), 999-1012.
14. F. Druon, S. Chenais & F. Raybaut, (2002). Apatite-structure Crystal, Yb^{3+}:$SrY_4(SiO_4)_3O$, for the Development of Diode-pumped Femtosecond Lasers. *Optics Letters*, 27 (21), 1914-1916.
15. F. Druon, F. Balembois & P. Georges, (2003). Laser Crystals for the Production of Ultra-short Laser Pulses. *Annales de Chimie-Science des Materiaux*, 28, 47-72.
16. F. Druon, F. Balembois & P. Georges, (2004). Ultra-short-pulsed and Highly-efficient Diode-pumped Yb : SYS Mode-locked Oscillators. *Optics Express*, 12 (20), 5005-5012.
17. F. Druon & P. Georges, (2004). Pulse-compression down to 20 fs Using a Photonic Crystal Fiber Seeded by a Diode-pumped Yb : SYS Laser at 1070 nm. *Optics Express*, 12 (15), 3383-3396.
18. P. H. Haumesser, R. Gaume, B. Viana, E. Antic-Fidancev & D. Vivien, (2001). Spectroscopic and Crystal-field Analysis of New Yb-doped Laser Materials. *Journal of Physics-Condensed Matter*, 13 (23), 5427-5447.

19. S. Celerier, C. Laberty, F. Ansart, P. Lenormand & P. Stevens, (2006). New Chemical Route Based on Sol-gel Process for the Synthesis of Oxyapatite $La_{9.33}Si_6O_{26}$. *Ceramics International*, 32 (3), 271-276.
20. W. M. Haynes (Ed.). (2010). *Handbook of Chemistry and Physics Online*. CRC Press.
21. J. Felsche, (1972). Rare-earth silicates with Apatite structure. *Journal of Solid State Chemistry*, 5 (2), 266-275.
22. G. R. Redhammer & G. Roth, (2003). Lithium and Sodium Yttrium Orthosilicate Oxyapatite, $LiY_9(SiO_4)_6O_2$ and $NaY_9(SiO_4)_6O_2$, at Both 100 K and Near Room Temperature. *Acta Crystallographica Section C*, 59, 120-124.
23. Y. Masubuchi, M. Higuchi, T. Takeda & S. Kikkawa, (2006). Oxide Ion Conduction Mechanism in $RE_{9.33}(SiO_4)_6O_2$ and $Sr_2RE_8(SiO_4)_6O_2$ (RE=La, Nd) from Neutron Powder Diffraction. *Solid State Ionics*, 177 (3-4), 263-268.
24. R. P. Gunawardane, R. A. Howie & F. P. Glasser, (1982). Structure of the Oxyapatite $NaY_9(SiO_4)_6O_2$. *Acta Crystallographica Section B*, 38 (May), 1564-1566.
25. M. G. Morgan, M. T. Wang & A. Mar, (2002). Samarium Orthosilicate Oxyapatite, $Sm_5(SiO_4)_3O$. *Acta Crystallographica Section E*, 58, 70-71.
26. B. Renner & G. Lehmann, (1986). Correlation of angular and Bond Length Distortions in TO4 Units in Crystals. *Zeitschrift Fur Kristallographie*, 175 (1-2), 43-59.
27. K. Robinson, G. V. Gibbs & P. H. Ribbe, (1971). Quadriatic Elongation – Quantitative Measure of Distortion in Coordination Polyhedra. *Science*, 172 (3983), 567-570.
28. Sudarsan.K, R. A. Young & P. E. Mackie, (1972). Comparison of Synthetic and Mineral Fluorapatite, $Ca_5(PO_4)_3F$, in Crystallographic Detail. *Materials Research Bulletin*, 7 (11), 1331-1338.
29. G. Blasse, (1975). Influence of Local Charge Compensation on Site Occupation and Luminescence of Apatites. *Journal of Solid State Chemistry*, 14 (2), 181-184.
30. M. Bauer & W. E. Klee, (1993). Induced Ferroelectricity in Chlorapatite. *Zeitschrift Fur Kristallographie*, 206, 15-24.
31. Y. Ohgi, H. Kagi, H. Arima, A. Ohta, K. Kamada, A. Yoshikawa & K. Sugiyama, (2009). Crystal Growth and Structural Characterizations of Ce-doped $Gd_{9.33}(SiO_4)_6O_2$ Single Crystals. *Journal of Crystal Growth*, 311 (3), 526-529.

Chapter 4 Crystal structures and photoluminescent properties of Eu^{3+} doped $Sr_2Y_8(SiO_4)O_2$

4.1 Introduction

From the previous chapter, the significant tolerance for different cations in silicate oxyapatite materials has been demonstrated. There are also many studies about the relationship between the photoluminescent properties of the rare earth incorporated silicate oxyapatite structures. Eu^{3+} is a special rare earth cation since its photoluminescent properties would reflect the local symmetries in the host lattice. The photoluminescence (PL) of Eu^{3+} is derived from the electronic transition between the 4*f* energy levels and usually result in orange-red light.[1,2] The magnetic dipole transition $^5D_0$-$^7F_1$ always occurs when Eu^{3+} cations interact with the host lattice. However the electric-dipole $^5D_0$-$^7F_2$ transition of Eu^{3+} is hypersensitive to the inversion center and strictly forbidden at the inversion center, whereas it will relax and gain high intensity when the symmetry of Eu^{3+} position is lower.[3] Moreover, the $^5D_0$-$^7F_0$ transition never splits under the crystal field, therefore it can serve as an indictor of site occupancy. As the silicate oxyapatite has two different cation sites and complex structure, a number of studies about Eu^{3+} doped silicate oxyapatites have been done to reveal the relationship of the PL properties and the structure, especially the site preference. Based on the analysis of the spectra of Eu^{3+} doped silicate oxyapatites, Blasse suggested that occupation preference of Eu^{3+} between A^I and A^{II} sites was governed by the local charge compensation, which derived from the underbonded free oxygen.[4] However, occasionally this theory conflicted with Felsche's theory [5] based on the size of the cation sites. Later, Lin and Su found Eu^{3+} occupying two cationic sites simultaneously and they attributed this phenomenon to the compromise of the size effect proposed by Felsche and the charge compensation effect proposed by Blasse.[6] All these studies were only focused on the spectral analysis and did not combine

with other materials characterization techniques, for instance X-ray diffraction and Rietveld refinement.

In the practical aspect, Eu^{3+} is a widely-used activator for red phosphor. In the fluorescent lamp, Eu^{3+} doped Y_2O_3 is the ideal red phosphor with quantum efficiency close to 100%. More recently, white light emit diodes (white LEDs) become attractive due to their low energy consumption, high durability and environmental friendliness.[7] The white LEDs with tri-color phosphors combine LED chips with emission at near-ultraviolet (near-UV) region with blue, green and red phosphors.[8,9] Currently the most applicable red phosphor for this kind of white LEDs is $Y_2O_2S:Eu^{3+}$, whose efficiency is much lower than the other two phosphors with green (e.g. $ZnS:Cu^{+}/Al^{3+}$) and blue (e.g. $BaMgAl_{10}O_{17}:Eu^{2+}$) emissions.[10] Also its chemical stability at higher temperature is poor. Therefore, a novel red phosphor excited effectively at the near UV region is needed to improve the performance of the white LEDs. Hu *et al.* suggested Eu^{3+} doped $CaMoO_4$ could be a promising red phosphor due to the intense red emission with excitation of Eu^{3+} 4*f* levels at near UV region and its good chemical stability.[11] Later, various molybdates and tungstates materials have been investigated as hosts for Eu^{3+} ions.[12-15] However, very few studies on silicate oxyapatites as white LED phosphor materials have been reported so far, though it was reported as a host for Eu^{3+} by Isaacs.[16]

Since the crystal structure of $Sr_2Y_8(SiO_4)_6O_2$ has been analyzed in detail at the previous chapter, $Sr_2Y_8(SiO_4)_6O_2$ is used as the host for Eu^{3+} in this chapter. The crystal structure especially the site occupancy of Eu^{3+} is studied by not only PL spectra but also X-ray diffraction and the Rietveld refinement. Furthermore, since pure $Sr_2Y_8(SiO_4)_6O_2$ was successfully synthesized by solid state reaction and sol-gel method in previous chapter, Eu^{3+} doped samples synthesized by these two methods are compared. Color and intensity of the red emission of this phosphor is also analyzed, indicating the potential application in white LEDs.

4.2 Experimental procedures

4.2.1 Synthesis of europium doped $Sr_2Y_8(SiO_4)_6O_2$

In the sol-gel synthesis, europium acetate $Eu(CH_3COO)_3$ (>99.9%, Sigma-Aldrich) was used as europium source and silicate oxyapatites with different doping concentration $Sr_2Y_{8-x}Eu_x(SiO_4)_6O_2$ (x = 0.05, 0.1, 0.5, 1, 2 and 5) were prepared. 0.002 mol sample was synthesized each time. Strontium nitrate $Sr(NO_3)_3$ (>99.9%, Fluka), hexahydrate yttrium nitrate $Y(NO_3)_3 \cdot H_2O$ (>99.9%, Sigma-Aldrich) and europium acetate $Eu(CH_3COO)_3$ were mixed stiochiometrically with 2.66 ml tetraethoxysilane $Si(OC_2H_5)_4$ (TEOS, >99.99%, Sigma-Aldrich) and dissolved in a solution with 6 ml deionized water, 6 ml absolute enthonal and 6 ml acetic acid. Reflux process was performed at 110°C for 4 hours to form the homogeneous gel. After drying the gel at 80°C for 12 hours, the product was heated to 700°C for 4 hours to eliminate the organic species. Finally the silicate oxyapatite powders were obtained by heat treatment at 1400°C for 6 hours.

In the solid state reaction, europium oxide Eu_2O_3 (>99.9%, Sigma-Aldrich) was the europium source and mixed with $SrCO_3$ (>99.0%, Alfa Aesar), silica gel 60 (>99.0%, Fluka) and the synthetic Y_2O_3 nanopowder. All the rest procedures were the same as introduced in the previous chapter.

4.2.2 Characterizations

X-ray diffraction (XRD, D8 Advance, Bruker AXS, Karlsruhe, Germany) with Cu*K*α radiation and operated at 40 kV and 30 mA was used to investigate the phase compositions. The scan speed was 2˚/min with a step size 0.02°. In order to determine the details of the crystal structure, Rietveld refinement was performed on the as-received XRD patterns by software TOPAS (version 3.0, Bruker AXS, Karlsruhe, Germany). Since the structure of Sr_2Y_8 $(SiO_4)_6O_2$ has been investigated in previous chapter, it was

used as the starting model. It also has been confirmed that the site occupancy of Sr^{2+} at A^I site is 50% in $Sr_2Y_8(SiO_4)_6O_2$. As Eu^{3+} only replace Y^{3+} in this study, occupancy of Sr^{2+} is kept constant as 50%. During the refinement of the site occupancies, some constraint conditions were set as follow. Considering the site multiplicities and assuming the site occupancy of Eu^{3+} at A^{II} site is n, the site occupancies of Eu^{3+} at A^I, Y^{3+} at A^I and Y^{3+} at A^{II} are $(x-6n)/4$, $(2-x+6n)/4$ and $1-n$ respectively with x in the chemical formula $Sr_2Y_{8-x}Eu_x(SiO_4)_6O_2$.

High resolution transmission electron microscopy (HRTEM) images and selected area diffraction patterns (SAED) were collected by a JEOL JEM 2100F transmission electron microscopes (Cs = 0.5 mm, accelerating voltage = 200 kV, Scherzer defocus ≈ −43 nm).The element distributions across the phosphor particles were examined by the energy dispersive x-ray spectroscopy (EDX, Oxford Instruments, UK), attached using the scanning transmission electron microscope (STEM) mode. The interval distance between the collected data points was 0.3 nm and the dwell time on each point was fixed at 400 μs in the line scan mode.

The normal photoluminescence (PL) and photoluminescence excitation (PLE) spectra were collected by a Shimadzu RF-5301PC spectrophotometer. PL and PLE with higher resolution were also measured. The excitation source was a Xenon lamp of 450 W with a monochromator of 0.3 m grating. The signal from the sample went through a monochromator of 0.75 m grating with filters. All the slits were fixed at 20 μm.

4.3 Results and discussion

4.3.1 The crystal structures of $Sr_2Y_{8-x}Eu_x(SiO_4)_6O_2$ from sol-gel method

The series of $Sr_2Y_{8-x}Eu_x(SiO_4)_6O_2$ (x=0.05, 0.1, 0.5, 1, 2, 5) from sol-gel method are confirmed to be pure silicate oxyapatite phases by XRD results and refinements (Table 4-1). The low values of *R* from the Rietveld refinement results for all the compounds prove the high reliability of the refined data. As an example, the XRD and Rietveld refinement patterns of $Sr_2Y_6Eu_2(SiO_4)_6O_2$ are shown in Figure 4-1. The XRD patterns of $Sr_2Y_{8-x}Eu_x(SiO_4)_6O_2$ (x=0.05, 0.1, 0.5, 1, 2, 5) are shown in Figure 4-2a and all the patterns indicate the high purities of the corresponding samples. Small deviation between the present results and the lattice constants in the previous chapter may be due to the usage of different XRD machines. The lattice constants *a* and *c* increase as the europium content in the sample increases (Figure 4-2b) because of larger Eu^{3+} size (r_{Eu3+} = 0.95 Å, r_{Y3+} = 0.9 Å with CN = 6). Moreover, the structure data of $Sr_2Y_6Eu_2(SiO_4)_6O_2$ (Table 4-2) obtained from the refinement are used to construct the polyhedral networks (Figure 4-3). This crystal structure appears similar to the europium-free $Sr_2Y_8(SiO_4)_6O_2$. Three types of polyhedra (A^I–O, A^{II}–O and Si–O) exist as well as the unique free oxygen O4. The bond lengths in the A^I–O polyhedra are 2.325, 2.511 and 2.811 Å respectively for A^I–O1, A^I–O2 and A^I–O3. The bond lengths for the A^{II}–O polyhedra range from 2.206 to 2.658 Å (Table 4-3). The free oxygen O4 is close to A^{II} position with length of 2.206 Å and its bond valence is calculated to be 1.79 which is underbonded.[17]

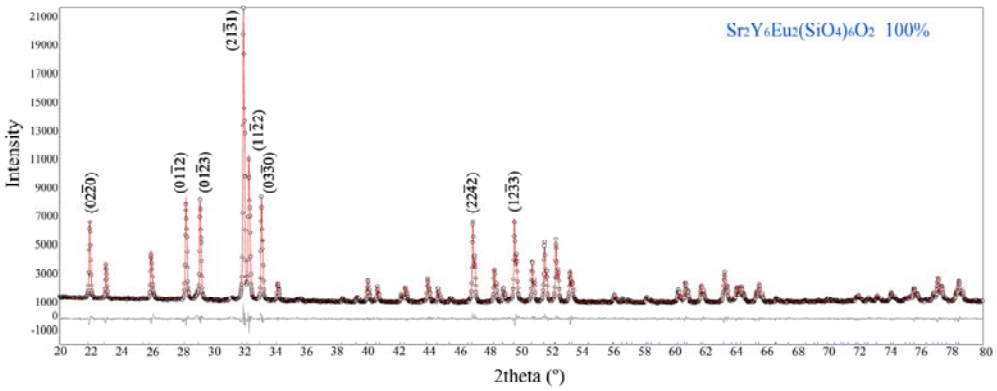

Figure 4-1 Rietveld refinement results for $Sr_2Y_6Eu_2(SiO_4)_6O_2$. The experimental X-ray diffraction pattern, the calculated refinement pattern and the difference between the former two pattern are shown in black, red and grey respectively.

Table 4-1 Rietveld refinement results for $Sr_2Y_{8-x}Eu_x(SiO_4)_6O_2$ (x = 0.05, 0.1, 0.5, 1, 2, 5)

	a /Å	c /Å	$^aR_{Bragg}$/%	^bR_p/%	$^cR_{wp}$/%	Eu@A^I	Eu@A^{II}	V/Å^3
X=0.05	9.3804(9)	6.8681(1)	1.204	3.79	4.78	0.0125	0	523.382(5)
X=0.1	9.3808(7)	6.8711(9)	2.047	6.36	9.27	0.0250	0	523.658(1)
X=0.5	9.3854(2)	6.8800(3)	1.781	6.51	8.97	0.1096	0.0103	524.837(4)
X=1	9.3884(9)	6.8820(1)	1.033	3.31	4.29	0.1491	0.0673	525.326(4)
X=2	9.3911(2)	6.8922(1)	2.512	3.52	4.70	0.2758	0.1501	526.422(6)
X=5	9.3941(8)	6.9146(2)	2.266	4.07	5.16	0.5	0.5	528.469(2)

$$^aR_{Bragg} = \frac{\sum |I_{k,obs} - I_{k,calc}|}{\sum I_{k,obs}}$$

$$^bR_{wp} = \sqrt{\frac{\sum w_m (Y_{m,obs} - Y_{m,calc})^2}{\sum w_m Y_{m,obs}^{\ 2}}}$$

$$^cR_p = \sqrt{\frac{\sum w_m |Y_{m,obs} - Y_{m,calc}|}{\sum Y_{m,obs}}}$$

Where $I_{k,obs}$ and $I_{k,calc}$ are the observed and calculated intensities of the kth reflection respectively; w_m is the reciprocal of the variance for each observation; $Y_{m,obs}$ and $Y_{m,calc}$ are the observed and calculated data respectively at data point m.

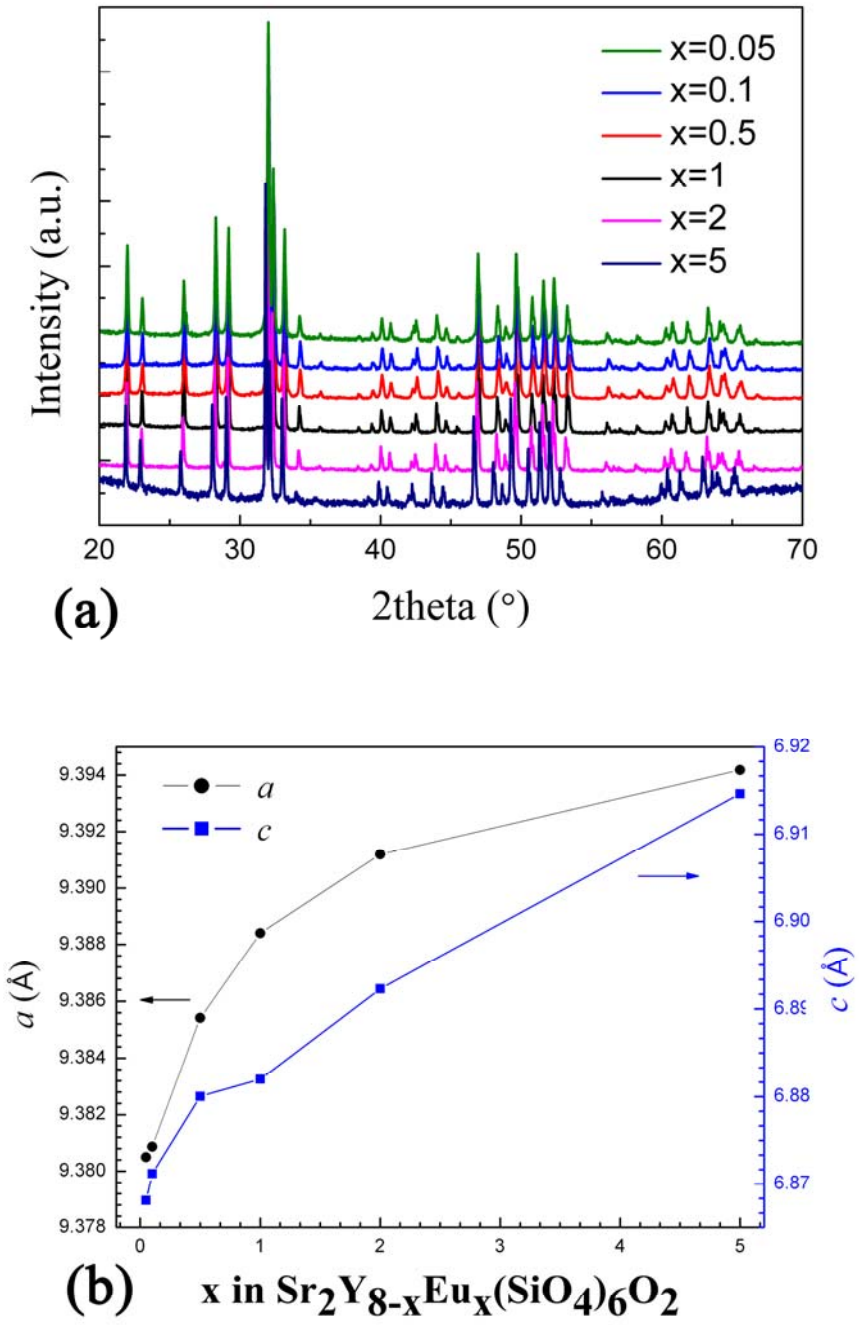

Figure 4-2 (a) the XRD patterns of $Sr_2Y_{8-x}Eu_x(SiO_4)_6O_2$ (x = 0.05, 0.1, 0.5, 1, 2, 5); (b) the relationships between the lattice constants and Eu^{3+} concentration.

Table 4-2 The atomic positions of $Sr_2Y_6Eu_2(SiO_4)_6O_2$ from the refinement

Atom	Wyckoff symbol	x/a	y/b	z/c	[a]Beq/Å^2
Y/Eu	6h (A^{II})	0.23131	0.99287	1/4	1.033
Y/Sr/Eu	4f (A^{I})	1/3	2/3	0.00412	1.842
Si	6h	0.39659	0.37084	1/4	0.847
O1	6h	0.31448	0.48850	1/4	0.201
O2	6h	0.58600	0.47145	1/4	0.397
O3	12i	0.34102	0.25627	0.06738	1.21
O4	2a	0	0	1/4	1.519

[a] The isotropic temperature factor Beq = *U*iso×8×pi^2

Table 4-3 The bond lengths (Å) of the A^I–O and A^{II}–O in $Sr_2Y_{8-x}Eu_x(SiO_4)_6O_2$ (x = 1, 2, 5)

Sites	bond	X = 1	X = 2	X = 5
A^I	3×A^I-O1	2.421(2)	2.325(9)	2.354(7)
	3×A^I-O2	2.469(7)	2.511(1)	2.413(5)
	3×A^I-O3	2.848(1)	2.811(8)	2.769(6)
	Average	2.579(3)	2.549(6)	2.512(6)
A^{II}	A^{II}-O4	2.199(4)	2.206(2)	2.217(3)
	2×A^{II}-O3	2.389(8)	2.354(7)	2.343(5)
	A^{II}-O2	2.443(6)	2.430(9)	2.418(8)
	2×A^{II}-O3	2.475(8)	2.493(5)	2.502(6)
	A^{II}-O1	2.565(9)	2.658(7)	2.686(1)
	Average	2.419(7)	2.427(5)	2.430(5)

Moreover, Rietveld refinement reveals the occupancy of Eu^{3+} between A^I and A^{II} sites in the materials with different Eu^{3+} doping concentrations. Eu^{3+} cations prefer occupying A^I site when Eu^{3+} concentration is low (x = 0 ~ 0.5), which is consistent with both the

theories about the site preference proposed by Blasse [4] and Felsche.[5] Blasse's theory emphasizes the influence of the charge compensation. In order to compensate the underbonded free oxygen bonded to A^{II} position, this position is preferred by cations with smaller radius and/or higher charge. Since the cationic radius of Y^{3+} is smaller than Eu^{3+}, Y^{3+} cations tend to enter A^{II} and Eu^{3+} cations prefer A^{I} sites. In Felsche's theory, the site occupancy is determined by the size of cationic site. Larger cation prefers the larger A^{I} site and vice versa. Therefore, larger Eu^{3+} cations tend to occupy A^{I} sites. In the samples with higher Eu^{3+} concentrations ($x \geq 0.5$), Eu^{3+} cations begin to accommodate A^{II} sites with the site preference to A^{I} still maintained. Some discrepancy from linear relationship between Eu^{3+} concentration and lattice constants around $x = 0.5 \sim 1$ (Figure 4-2b) may be due to Eu^{3+} entering A^{II} sites. Beside of the site occupancies of Eu^{3+}, the polyhedral shapes would evolve with various Eu^{3+} concentrations and more pronounced with higher Eu^{3+} concentrations. Therefore, samples with $x = 1, 2, 5$ are chosen (Table 4-3) and their average bond lengths in A^{I}–O and A^{II}–O polyhedra are shown. With the increase of Eu^{3+} concentration, the average bond length of A^{II}–O is elongated from 2.419 to 2.430 Å, because larger Eu^{3+} cations substitute Y^{3+} at A^{II} sites and enlarge the polyhedra. As shown in Figure 4-3, the column of free oxygen atoms is surrounded by six columns cations A^{II} sites along the *c* axis. There are mainly two Coulomb interactions exerting on cations at A^{II} sites, one is the attractive force from the free oxygen and the other is the repulsive force between neighboring A^{II} columns. With Y^{3+} cations replaced by larger Eu^{3+} cations, the repulsive force enlarges the distances between A^{II} columns and results in longer bond lengths. However, with the increase of Eu^{3+} concentration, the A^{I}–O polyhedron shrinkages as its average bond length decreases from 2.579 to 2.512 Å. It is because the repulsive forces between the A^{I} columns are weak as they are separated by Si−O polyhedra and the expansion of A^{II}–O polyhedra compresses the volume of A^{I}–O polyhedra.

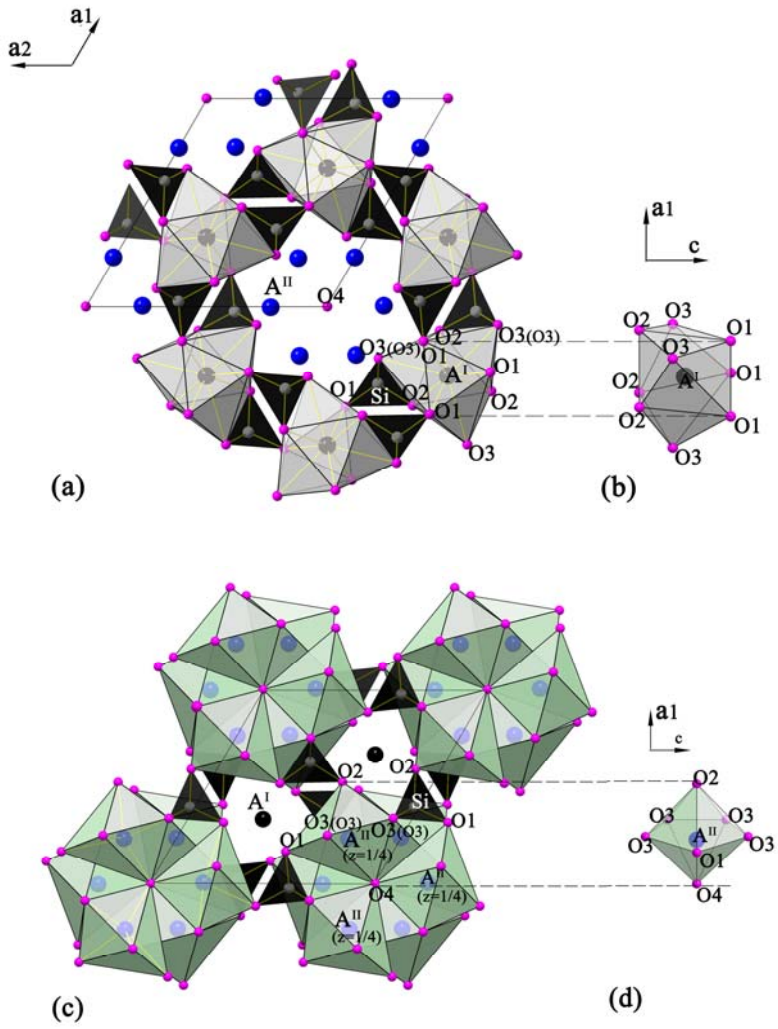

Figure 4-3 The crystal structure of $Sr_2Y_6Eu_2(SiO_4)_6O_2$. The spheres of black, blue, white and pink colors represent A^I cation, A^{II} cation, silicon, and oxygen atoms, respectively. (a) crystal structure along *c*-axis direction with the A^I−O polyhedra and Si−O are highlighted; (b) the A^I−O polyhedra along *a*-axis direction; (c) crystal structure along *c*-axis direction with the A^{II}−O polyhedra and Si−O are highlighted; (d) the A^{II}−O polyhedra along *a*-axis direction

The HRTEM image and the FFT pattern in *c* direction are shown in Figure 4-4. The d-spacing of $(10\bar{1}0)$ obtained from the HRTEM is about 8.1 Å. This d-spacing value can also be calculated from crystallographic data (Table 4-1) as:

$$d_{(10\bar{1}0)} = a \bullet \cos 30^\circ = 9.3911 \bullet \frac{\sqrt{3}}{2} \text{Å} = 8.1329 \text{Å} \approx 8.1 \text{Å} \qquad \text{Equation 4-1}$$

The result agrees with the observation from HRTEM, indicating the high reliability of the crystallographic data obtained from Rietveld refinement.

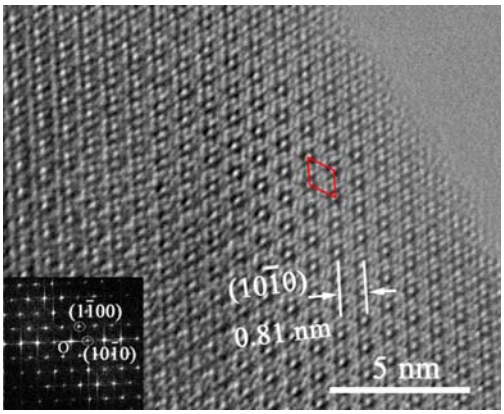

Figure 4-4 HRTEM image along the *c*-axis direction. The inset image is the FFT image

4.3.2 Photoluminescent properties

The PLE spectra of $Sr_2Y_{8-x}Eu_x(SiO_4)_6O_2$ (x=0.05, 0.1, 0.5, 1, 2, 2.5, 5) with the emission fixed at 613 nm are shown in Figure 4-5. The Eu^{3+}–O^{2-} charge transfer band (CTB), which is allowed by the selection rules, appears at 250−300 nm with a broad width. The intra-*4f* transitions from the ground state $^7F_0$ of Eu^{3+} result in the sharp peaks at 350−450 nm. The intra-*4f* transitions from Eu^{3+} at A^I and A^{II} sites are mostly overlapped, because different coordination environments affect little on the *4f* electrons which are well shielded by the outer electrons. The PLE peaks of the intra-*4f* transitions are intensified by the increase of Eu^{3+} concentration with $x \leq 2$. There are two reasons to explain this phenomenon. Firstly, each Eu^{3+} cation contributes to the overall intensities of the PLE peaks, regardless of the occupation at A^I or A^{II} sites. So more Eu^{3+} doped definitely increase the overall PLE intensities of the intra-*4f* transitions until concentration quenching happens. It also explains the increase of CTB intensities when $x \leq 2$. However, apparently the increase of intensities for intra-*4f* transitions is more pronounced than that of CTB, which is related to the second reason. Based on the parity selection rules, the intra-*4f* transitions are forbidden. But this selection rules is relaxed due to the effect of uneven crystal field components which can mix the opposite parity *5d* wave functions into those of *4f*.[18, 19] According to the crystal structure, A^{II} sites are linked to the free

oxygen O4 that would induce a linear crystal field at A^{II} sites,[4] while no such feature exists at A^{I} site. Consequently, the intra-*4f* transitions of Eu^{3+} at A^{II} are more probable and their corresponding peaks in PLE are higher than those for A^{I} sites. Therefore, the PLE peaks of the Eu^{3+} intra-*4f* transitions are intensified rapidly due to the increase of Eu^{3+} occupancy at A^{II}. The transition with highest intensity is the $^7F_0$–$^5L_6$ transition at 393 nm when x = 2 (Figure 4-5), which means the 613 nm emission of $Sr_2Y_6Eu_2(SiO_4)_6O_2$ can be excited most effectively at 393 nm. Moreover, the concentration quenching lowers the intensities in the PLE when x > 2.

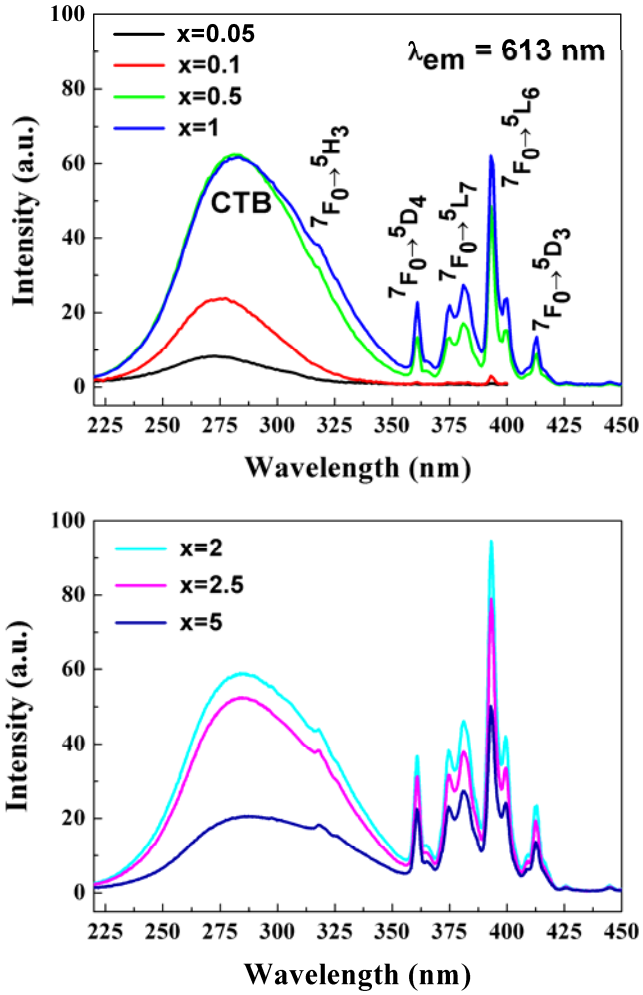

Figure 4-5 The PLE spectra of $Sr_2Y_{8-x}Eu_x(SiO_4)_6O_2$ (x = 0.05, 0.1, 0.5, 1, 2.5, 5) with the emission wavelength fixed at 613 nm. The CTB and the intra-*4f* transitions are indexed.

The positions of CTB in the PLE spectra also vary with different Eu^{3+} concentrations. At lower Eu^{3+} concentration, CTB is positioned around 273 nm while CTB of $Sr_2Y_3Eu_5(SiO_4)_6O_2$ red-shifts to 289 nm. It can also be ascribed to Eu^{3+} occupancies. In higher Eu^{3+} concentration, Eu^{3+} would accumulate at A^{II} sites which are linked to the free oxygen O4 with the shortest bond as compared to others. The short bond induces more overlapping between electronic orbitals of Eu^{3+} and O^{2-} and lowers the energy required to transfer one electron from the O^{2-} to Eu^{3+},[2] which leads to red-shift of CTB position.

As discussed above, the excitation of $^7F_0$–$^5L_6$ transition at 393 nm is effective and, coincidently, it matches the near-UV emission of the InGaN LED chip, so the photoluminescence (PL) of these silicate oxyapatite materials is studied by excitation at 393 nm (Figure 4-6). Red emissions from the intra-*4f* transitions $^5D_0$–$^7F_{0,1,2,3,4}$ under this excitation are detected (Figure 4-6a). Emission from higher levels of $^5D_1$ or $^5D_2$ is not detected. It is because the multiphonon relaxation process resulted from high vibration frequency (υ_{SiO4} = 930 cm^{-1}) in the host lattice bridges $^5D_0$ with $^5D_1$ and $^5D_2$ and relaxes all the electrons to $^5D_0$ state. The peak intensity of the forced electric-dipole transition $^5D_0$–$^7F_2$ at 613 nm is much higher than that of the magnetic-dipole transition $^5D_0$–$^7F_1$, which indicates the positions Eu^{3+} occupying are not inversion centers and is consistent with structure results.[20]

In line with PLE spectra, $Sr_2Y_6Eu_2(SiO_4)_6O_2$ has the most intense emission of 613 nm among the series of materials (Figure 4-6b). Concentration quenching occurs if further increase the Eu^{3+} concentration and the intensities of the emission peaks would be reduced. In fact, both radiative and non-radiative processes simultaneously are involved when the excited electrons release the energy. In order to characterize the radiative and non-radiative processes, the parameter termed as critical distance (R_c) is used. It is defines the separation between atoms when the probability of radiative process (P_r) equals to that of non-radiative process (P_n). When the distances between Eu^{3+} cations are larger than R_c,

energy releasing process is more locally and radiative process is preferred; while the distances between Eu^{3+} are shorter than R_c, energy migration between Eu^{3+} cations occurs and non-radiative process happens. As the sizes of Eu^{3+} and Y^{3+} are similar, the unit cell can be considered as constant during substitution. Increasing Eu^{3+} concentration can be considered as filling more Eu^{3+} cations in a fixed volume, which lead to shorter separation between Eu^{3+} cations. Once the concentration reaches certain value (critical concentration), the separation between Eu^{3+} cations become R_c. The relation between critical concentration and R_c can be expressed as:

$$R_c \approx 2\left(\frac{3V}{4\pi xN}\right)^{1/3} \qquad \text{Equation 4-2}$$

Where x is the critical concentration, V is the volume of the unit cell and N is the number of the host cationic sites in the unit cell.[21,22] In the current case, V is 526.4 $Å^3$, N is 8 and x is about 2, so the critical distance R_c is about 4 Å. If Eu^{3+} cations are closer than this distance, the energy migrates occurs and finally results in concentration quench.[23] The nearest distances of A^I–A^I, A^{II}–A^{II} and A^I–A^{II} are about 3.5, 4.1 and 4.0 Å respectively according to XRD refinement results, which are comparable to the value R. Therefore, the concentration quenching occurs when the activators become neighbors at high Eu^{3+} content.

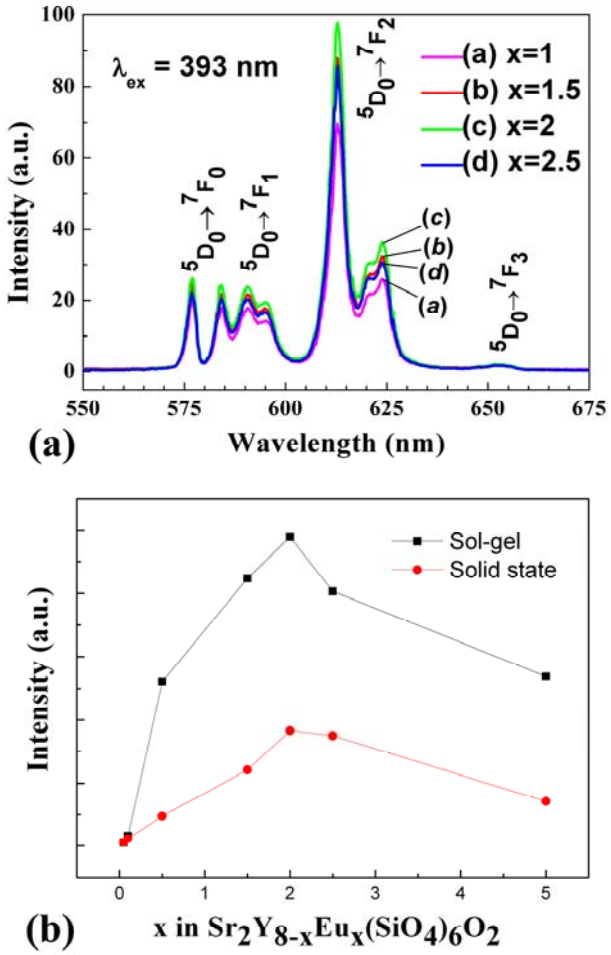

Figure 4-6 (a) PL spectra of $Sr_2Y_{8-x}Eu_x(SiO_4)_6O_2$ (x = 1, 1.5, 2, 2.5) excited at 393 nm. (b) the variation of the PL intensities with the Eu^{3+} doping concentration. Samples from both sol-gel and solid state reaction are shown.

The crystal fields around Eu^{3+} tend to split the energy levels such as ^7F_J or ^5D_J (J>0) but the energy level with J = 0 will never split under crystal field. Therefore, the number of the $^5D_0$–$^7F_0$ transition peaks in PL spectra should be equal to that of the cationic sites occupied by Eu^{3+}. Figure 4-7 shows the high resolution PL spectra of the $^5D_0$–$^7F_0$ transition of $Sr_2Y_6Eu_2(SiO_4)_6O_2$. The existence of two $^5D_0$–$^7F_0$ peaks indicates that Eu^{3+} occupies both A^I and A^{II} positions. The two peaks are differentiated by Gaussian fitting and the positions are identified at 577.5 nm (α) and 578.5 nm (β). High resolution PLE spectra monitored the emission at α and β peaks are shown in Figure 4-7b. The CTB positions for α and β peaks are at 297.5 and 292.9 nm respectively. As discussed above,

the short distance between Eu^{3+} at A^{II} and the free oxygen leads to CTB at longer wavelength. So the α peak is assigned to Eu^{3+} at A^{II} and β peak is related to Eu^{3+} at A^{I}. Moreover, the $^5D_0$–$^7F_0$ transitions between the sample with x = 2 and 5 are compared (Figure 4-7c). The α (A^{II}) peak of sample with x = 5 is slightly higher than that of the sample with x = 2, indicating the increase of Eu^{3+} content at A^{II} sites. However, the difference in the spectra is not as much as that in site occupancies, probably due to the energy transfer from Eu^{3+} at A^{II} sites to those at A^{I} sites.

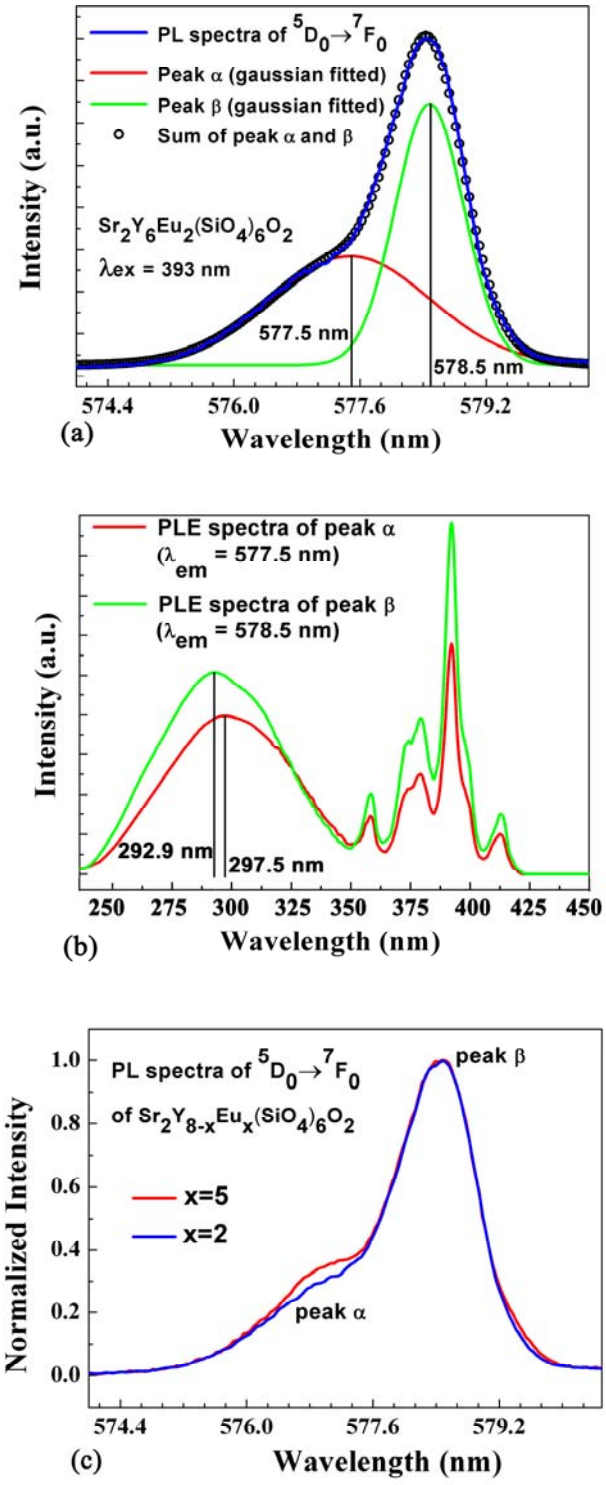

Figure 4-7 (a) the high resolution PL spectra of the $^5D_0$-$^7F_0$ transition in $Sr_2Y_6Eu_2(SiO_4)_6O_2$ excited at 393 nm. Double peak Gaussian fitting is performed and the peaks of α and β are identified at 577.5 nm and 578.5 nm. (b) the high resolution PLE spectra of peak α and β. (c) The normalized high resolution Pl spectra of the $^5D_0$-$^7F_0$ transition in $Sr_2Y_6Eu_2(SiO_4)_6O_2$ and $Sr_2Y_3Eu_5(SiO_4)_6O_2$. Both are excited at 393 nm.

4.3.3 Effect of processing methods on the microstructures and photoluminescent properties

Sol-gel method and solid state reaction are two common methods to synthesize the phosphors. Here the structures and photoluminescent properties of the $Sr_2Y_6Eu_2(SiO_4)_6O_2$ phosphor materials synthesized from both routes are compared. According to the XRD of $Sr_2Y_6Eu_2(SiO_4)_6O_2$, both methods can produce pure oxyapatite phase. Regarding to the $^5D_0-^7F_2$ transition at 613 nm, the intensity of the phosphor synthesized from sol-gel method is about three times higher than that synthesized via solid state reaction as indicated in Figure 4-6b, which is consistent with other authors' reports.[24-26] The sol-gel method is a wet chemistry approach and the ions participated in the reaction are mixed homogeneously at atomic level. Therefore, the activator ions are distributed uniformly across the final product. However, during the solid state reaction, the diffusion process is crucial for the phase formation, which would result in the segregation of some reactant elements with different diffusion rates. Figure 4-8 shows the EDX spectra of the surfaces of the phosphors synthesized via sol-gel and solid state reaction. In order to normalize the EDX spectra of yttrium (Y) and europium (Eu) in $Sr_2Y_6Eu_2(SiO_4)_6O_2$, the intensity of the Eu is magnified by three times during plotting. The spectra of Y and Eu from sol-gel synthesized sample show little composition variation, demonstrating the good homogeneity. However, obvious difference between Y and Eu appears in the EDX spectra from the solid state reacted sample. It indicates that, even though the pure phase is obtained, uneven distributions of the elements occur and deteriorate the luminescent properties. So it is a more appropriate way to synthesize Eu:$Sr_2Y_8(SiO_4)_6O_2$ by sol-gel method.

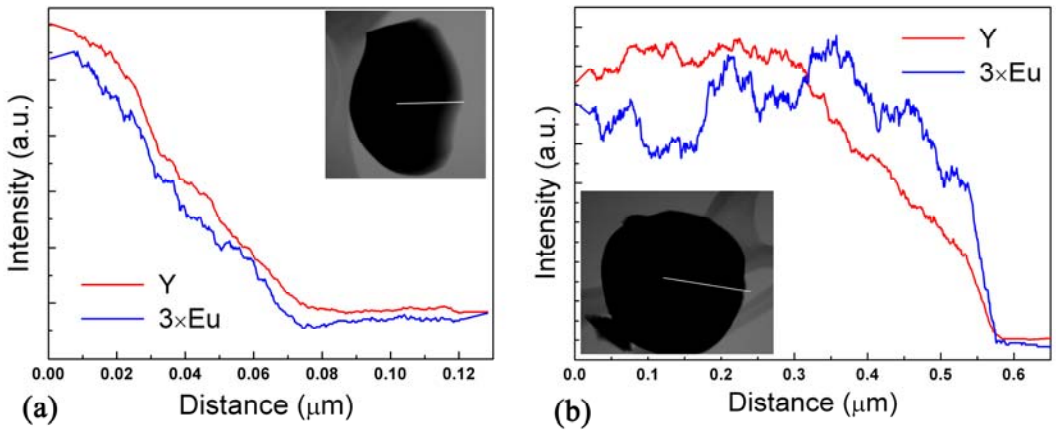

Figure 4-8 EDX spectra of the $Sr_2Y_6Eu_2(SiO_4)_6O_2$ obtained from (a) sol-gel method and (b) solid state reaction. The signals of europium (Eu) are enlarged by three times in order to compare with the signals of yttrium (Y). The insets are the corresponding STEM images.

4.3.4 Comparison with commercial Eu:Y_2O_3 phosphor

The PL and PLE spectra of $Sr_2Y_6Eu_2(SiO_4)_6O_2$ and commercial Eu:Y_2O_3 phosphor (4.5 wt% Eu^{3+}, Advanced Material Resources, Singapore) are shown in Figure 4-9. Eu:Y_2O_3 is a commercial red phosphor applied in fluorescent lamp and its quantum efficiency is almost 100%. Indeed, it can be excited effectively by the ultraviolet light at 254 nm (Figure 4-9a), which can be produced by discharge of mercury vapor in the fluorescent lamp. The lower intensities of the PLE peaks in the near UV region mean Eu:Y_2O_3 is not suitable for near UV excitation, while the strong peak in the PLE of $Sr_2Y_6Eu_2(SiO_4)_6O_2$ at 393 nm indicates efficient excitation. The PL spectra confirm that $Sr_2Y_6Eu_2(SiO_4)_6O_2$ excited at 393 nm can emit red light with comparable intensity of Eu:Y_2O_3 phosphor under 254 nm excitation.

Furthermore, CIE coordinates of the emission from $Sr_2Y_6Eu_2(SiO_4)_6O_2$ with excitation at 393 nm are (0.63, 0.37), close to the coordinates of pure red color (0.67, 0.33) in National Television System Committee (NTSC) standard. The strong emission and the nearly pure red color ensure Eu:$Sr_2Y_8(SiO_4)_6O_2$ as a promising phosphor in the white LED applications.

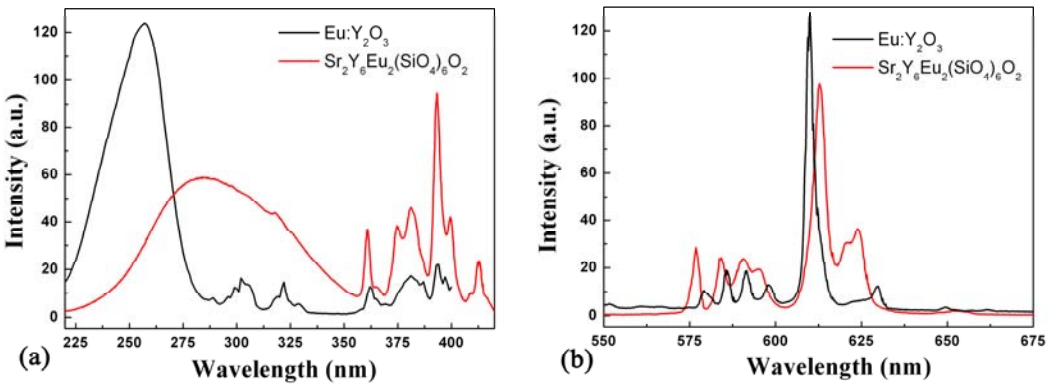

Figure 4-9 (a) PLE and (b) PL spectra of $Sr_2Y_6Eu_2(SiO_4)_6O_2$ and commercial Eu:Y_2O_3 powder

4.4 Conclusion

1. Pure europium doped silicate oxyapatites $Sr_2Y_{8-x}Eu_x(SiO_4)_6O_2$ are synthesized by sol-gel method. The XRD and Rietveld refinement reveal that most Eu^{3+} cations enter A^I site in low europium concentration (x = 0~0.5). As the Eu^{3+} concentration increases (x > 0.5), Eu^{3+} also occupy A^{II} site but the preference to the A^I site is still maintained. With the increase of the europium concentration, the average bond length in A^{II}–O polyhedron and the bond length of A^{II}–O4 are elongated, but the average bond length in A^I–O polyhedron becomes smaller.

2. The photoluminescent properties are closely related to the crystal structure. Cationic sites with no inversion center result in intense emission of the $^5D_0$–$^7F_2$ transition of Eu^{3+}. As Eu^{3+} cations enter A^{II} sites in higher doping concentration, the free oxygen O4 linking to the A^{II} site induces the shifting of CTB bands and relaxation of parity selection rule, leading to an effective excitation of the $^7F_0$–$^5L_6$ transition at 393 nm. Moreover, the analysis of the $^5D_0$–$^7F_0$ transition confirms that Eu^{3+} occupies two different cationic sites.

3. $Sr_2Y_6Eu_2(SiO_4)_6O_2$ appears to be the one with the highest emission intensity. Further increase of the europium content leads to the concentration quenching which reduces the emission intensity. The critical distance for concentration quenching is about 4 Å.

4. Comparison between the samples from solid state reaction and sol-gel method indicates that the sol-gel method is able to achieve more homogeneous microstructure and higher light output samples.

5. The light output of $Sr_2Y_6Eu_2(SiO_4)_6O_2$ excited at 393 nm is comparable to commercial fluorescent lamp phosphor Eu:Y_2O_3. The CIE coordinates for $Sr_2Y_6Eu_2(SiO_4)_6O_2$ are

(0.63, 0.37) which is close to the pure red color. Therefore, this Eu^{3+} doped $Sr_2Y_8(SiO_4)_6O_2$ is a promising red phosphor for the white LEDs.

4.5 References

1. G. Blasse & A. Bril, (1967). Structure and Eu^{3+} Fluorescence of Lithium and Sodium Lanthanide Silicates and Germanates. *Journal of Inorganic & Nuclear Chemistry*, 29 (9), 2231-2241.
2. G. Blasse, (1966). On Eu^{3+} Fluorescence of Mixed Metal Oxides. 4, Photoluminescent Efficiency of Eu^{3+} Activated Oxides. *Journal of Chemical Physics*, 45 (7), 2356-2360.
3. G. Blasse, A. Bril & W. Nieuwpoo, (1966). On Eu3+ Fluorescence in Mixed Metal Oxides. 1, Crystal Structure Sensitivity of Intensity Ratio of Electric and Magnetic Dipole Emission. *Journal of Physics and Chemistry of Solids*, 27 (10), 1587-1592.
4. G. Blasse, (1975). Influence of Local Charge Compensation on Site Occupation and Luminescence of Apatites. *Journal of Solid State Chemistry*, 14 (2), 181-184.
5. J. Felsche, (1972). Rare-earth Silicates with Apatite Structure. *Journal of Solid State Chemistry*, 5 (2), 266-275.
6. J. Lin & Q. A. Su, (1994). A Study of Site Occupation of Eu^{3+} in $ME_2Y_8(SiO_4)_6O_2$ (ME=Mg, Ca, Sr). *Materials Chemistry and Physics*, 38 (1), 98-101.
7. A. Bergh, G. Craford, A. Duggal & R. Haitz, (2001). The Promise and Challenge of Solid-state Lighting. *Physics Today*, 54 (12), 42-47.
8. J. K. Sheu, S. J. Chang, C. H. Kuo, Y. K. Su, L. W. Wu, Y. C. Lin, W. C. Lai, J. M. Tsai, G. C. Chi & R. K. Wu, (2003). White-light Emission from Near UV InGaN-GaN LED Chip Precoated with Blue/green/red Phosphors. *IEEE Photonics Technology Letters*, 15 (1), 18-20.
9. S. Muthu, F. J. P. Schuurmans & M. D. Pashley, (2002). Red, Green, and Blue LEDs for White Light Illumination. *IEEE Journal of Selected Topics in Quantum Electronics*, 8 (2), 333-338.
10. S. Neeraj, N. Kijima & A. K. Cheetham, (2004). Novel Red Phosphors for Solid-state Lighting: the System $NaM(WO_4)_{2-x}(MoO_4)_x$: Eu^{3+} (M=Gd, Y, Bi). *Chemical Physics Letters*, 387 (1-3), 2-6.
11. Y. S. Hu, W. D. Zhuang, H. Q. Ye, D. H. Wang, S. S. Zhang & X. W. Huang, (2005). A Novel Red Phosphor for White Light Emitting Diodes. *Journal of Alloys and Compounds*, 390 (1-2), 226-229.
12. Y. C. Chang, C. H. Liang, S. A. Yan & Y. S. Chang, (2010). Synthesis and Photoluminescence Characteristics of High Color Purity and Brightness $Li_3Ba_2Gd_3(MoO_4)_8$:Eu^{3+} Red Phosphors. *Journal of Physical chemistry C*,114 (8), 3645-3652.
13. Z. Xu, C. Li, G. Li, R. Chai, C. Peng, D. Yang & J. Lin, (2010). Self-Assembled 3D Urchin-Like $NaY(MoO_4)_2$:Eu^{3+}/Tb^3+ Microarchitectures: Hydrothermal Synthesis and Tunable Emission Colors. *Journal of Physical chemistry C*, 114 (6), 2573-2582.
14. Z. L. Wang, H. B. Liang, L. Y. Zhou, H. Wu, M. L. Gong & Q. Su, (2005). Luminescence of $(Li_{0.333}Na_{0.334}K_{0.333})Eu(MoO_4)_2$ and Its Application in Near UV InGaN-based Light-emitting Diode. *Chemical Physics Letters*, 412 (4-6), 313-316.
15. L. Zhou, L. G. Yi, R. F. Sun, F. Z. Gong & J. H. Sun, (2008). A Potential Red Phosphor $Na_{0.5}Gd_{0.5}MoO_4$:Eu^{3+} For Light-Emitting Diode Application. *Journal of the American Ceramic Society*, 91 (10), 3416-3418.
16. T. J. Isaacs, (1973). Study of Eu^{3+} Fluorescence in Some Silicate Oxyapatites. *Journal of the Electrochemical Society*, 120 (5), 654-656.
17. I. D. Brown & D. Altermatt, (1985). Bond-valence Parameters Obtained from a Systematic Analysis of the Inorganic Crystal-structure Database. *Acta Crystallographica Section B*, 41 (Aug), 244-247.

18. B. R. Judd, (1962). Optical Absorption Intensities of Rare-earth Ions. *Physical Review*, 127 (3), 750-761.
19. G. S. Ofelt, (1962). Intensities of Crystal Spectra of Rare-Earth Ions. *Journal of Chemical Physics*, 37, 511-520.
20. G. Blasse & B. C. Grabmajer, (1994). *Luminescent Materials*. Berlin: Springer-Verlag.
21. G. Blasse, (1969). Energy Transfer in Oxidic Phosphors. *Philips Res. REP.*, 24, 131.
22. X. M. Liu, C. K. Lin & J. Lin, (2007). White Light Emission from Eu^{3+} in $CaIn_2O_4$ Host Lattices. *Applied Physics Letters*, 90 (8).
23. G. Blasse, (1967). Concentration Quenching of Eu^{3+} Fluorescence. *Journal of Chemical Physics*, 46 (7), 2583-2585.
24. D. Boyer, G. Bertrand-Chadeyron, R. Mahiou, C. Caperaa & J. C. Cousseins, (1999). Synthesis Dependent Luminescence Efficiency in Eu^{3+} Doped Polycrystalline YBO^3. *Journal of Materials Chemistry*, 9 (1), 211-214.
25. S. Y. Yin, D. H. Chen, W. J. Tang & Y. H. Yuan, (2007). Synthesis of $CaTiO_3$: Pr, Al Phosphors by Sol-gel Method and Their Luminescence Properties. *Journal of Materials Science*, 42 (8), 2886-2890.
26. P. T. Diallo, K. Jeanlouis, P. Boutinaud, R. Mahiou & J. C. Cousseins, (2001). Improvement of the Optical Performances of Pr^{3+} in $CaTiO_3$. *Journal of Alloys and Compounds*, 323, 218-222.

Chapter 5 Fabrication of $Sr_2Y_8(SiO_4)_6O_2$ translucent ceramics

5.1 Introduction

Other than the application as phosphor, silicate oxyapatites have been utilized in solid state lasers and scintillators,[1-3] due to their good thermal and chemical stability as well as the flexible structures.[4] Both applications in lasers and scintillators require the silicate oxyapatites to be bulk and transparent, so mostly single crystals are used. Czochralski method is widely employed as the crystal growth method for the silicate oxyapatites with high melting points (~2000 °C).[5] However, Czochralski method is a cost and time consuming process. The crystal growth requires expensive equipments to maintain crucial conditions. Moreover, it is difficult to fabricate crystal with high activator concentration due to the segregation effect. Therefore, in order to overcome these drawbacks, the transparent ceramics have come into sight as a promising alternative. Like all the ceramic materials, transparent ceramics are also polycrystalline with random-oriented grains. Their closely compacted grains and extreme low porosity lead these ceramics transparent to the visible light. Various ceramic processes provide possible ways to fabricate transparent ceramics with comparable properties to single crystals [6, 7] but higher efficiency in both time and cost aspects. Moreover, sophisticated ceramic fabrication techniques can produce tailored shapes and composites, which is an advantage over single crystal growth. Another important advantage of transparent ceramics is that tailored shape and different composites can be achieved by the ceramic processing techniques.[8]

The main principle to produce transparent ceramics is to minimize or eliminate the light-scattering centers within the ceramic body such as pores, impurity phases, rough surfaces and grain boundaries.[9] Rough surfaces can be minimized by carefully polishing the sample surfaces and the second-phase inclusions can be eliminated by pure raw

ceramic powder. The scattering effect of the pores is predominant since the porosity as low as 0.1% can deteriorate the transparency.[10] Several sintering techniques like the hot isostatic pressing and the high vacuum sintering [11-13] are developed to remove the pores and produce highly condensed materials. More recently, another sintering technique, the spark plasma sintering (SPS) is drawing more attention. This technique could heat the sample with a high heating rate due to the spark plasma induced by high-pulsed electric current. As the spark discharge between the powder particles heats the sample homogeneously, there is almost no temperature gradient within the sample during the sintering process.[14] Moreover, the combination of mechanical pressure, vacuum condition and electric field during the spark plasma sintering process is favorable for the elimination of pores and the consolidation of the particles. Transparent ceramics of various materials such as YAG [15] and $MgAl_2O_4$ [16, 17] have been successfully produced via SPS process. The scattering at grain boundaries usually occurs in the non-cubic materials which exhibit anisotropic optical properties. When the light encounters the boundary between two grains with different refractive indexes, the strong light-scattering occurs.[10] Therefore, all ceramics with high transparency are of cubic crystal structures such as YAG,[18,19] Y_2O_3,[20,21] Sc_2O_3 [13]. Ceramics with non-cubic structures usually appear translucent, such as Lu_2SiO_5 (monoclinic) whose translucent ceramic form has been produced and applied in X-ray and gamma ray detection.[22,23]

So far, few attempts to fabricate translucent silicate oxyapatite ceramics have been reported. In this chapter, the silicate oxyapatite $Sr_2Y_8(SiO_4)_6O_2$ powder is sintered in SPS with the attempt to produce highly condensed ceramics. Due to the hexagonal structure, a translucent appearance is expected. In order to eliminate the scattering effect caused by the impurity phases, pure $Sr_2Y_8(SiO_4)_6O_2$ powders from solid state reaction as reported in Chapter 2 are used. The powders from sol-gel method are not used here because their irregular shapes and inhomogeneity as shown in Chapter 2 are not suitable for sintering.

The microstructure evolutions of the ceramics during sintering are demonstrated. The light transmittances of ceramics with complete and incomplete condensation are compared and investigated. The Mie scattering theory [24,25] is applied to analyze the influence of the pore and birefringence on the light transmittance.

5.2 Experimental procedures

The $Sr_2Y_8(SiO_4)_6O_2$ powders synthesized from solid state reaction as described in Chapter 2 were further ball milled using zirconia balls and ethanol for 6 hours. A SPS system (Sumitomo Coal Mining SPS system, Dr. Sinter Modal 1050, Japan) was used to produce the ceramic samples. Each batch of 2 grams powders was filled in a graphite die and aligned in the SPS chamber. The samples were first heated to 600 ºC with a heating rate of 300 ºC/min and held for 1 minute for stabilization. After that temperature was further increased with a heating rate 100 ºC/min and dwelled at the final temperature for 3 minutes. The temperature profile was monitored by a pyrometer. The pressure on the graphite die was kept at 23 MPa. The as-received ceramic pellets were annealed at 1400 ºC for 1 hour to remove the residual carbon as well as other defects. The surfaces of the pellets were carefully polished by sand papers and diamond pastes to a thickness of 0.8 mm.

The phase compositions of the as-synthesized samples were studied by X-ray diffractometer (XRD, D8 Advance, Bruker AXS, Karlsruhe, Germany) with a Cu-tube. It is operated at 40 kV and 30 mA with scan range of 10° - 80°. Rietveld refinement was performed by software TOPAS (Version 3.0. Bruker AXS, Karlsruhe, Germany). The sizes of the powders and the surface morphologies were observed using a JEOL JSM-6340F scanning electron microscope (SEM, Tokyo, Japan) with a field emission source. The grain sizes at the sample surface were measured from the SEM image and a correction factor 1.56 was used.[26] The total forward transmittance is the parameter that includes all the light passed through the sample in -180°−180° range. It was measured by the Lambda 1050 UV/VIS/IR spectrometer equipped with the integration sphere (Perkin Elmer, MA, USA) in the range from 400 nm to 800 nm. For the in-line transmittance, only the transmitted light in the same direction as the incident light is considered. It was measured by Cary 5000 UV-VIS-NIR spectrophotometer (Varian, California, USA) in the

range from 200 nm to 810 nm. The densities of the ceramic pellets were measured using Archimedes method.

The effective scattering coefficients of the birefringence and pores for the in-line transmittance were calculated by the Mie scattering theory. All the calculations of Mie scattering used an algorithm written by Prahl.[25, 27]

5.3 Results and discussion

5.3.1 Characterization of microstructures

XRD patterns of the ceramics sintered by SPS at 1400 ºC and 1500 ºC combined with the raw $Sr_2Y_8(SiO_4)_6O_2$ powders are shown in Figure 5-1. Since the calculated [28] and experimental patterns agree with each other, the impurities are excluded and pure silicate oxyapatite phases are indexed. So the light scattering at the secondary phase will be minimized in the ceramics.

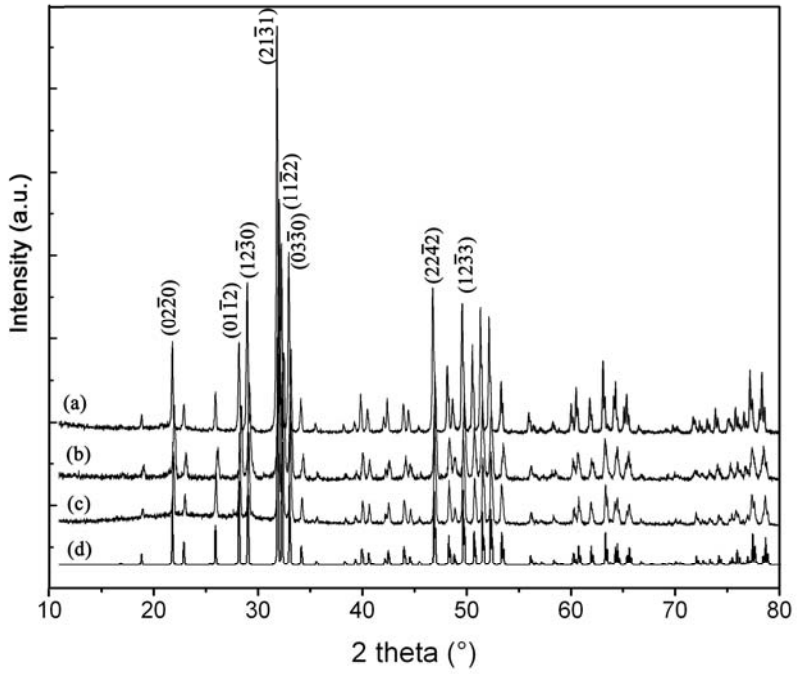

Figure 5-1 XRD patterns of (a) the $Sr_2Y_8(SiO_4)_6O_2$ ceramic pellet SPSed at 1500 ºC, (b) the $Sr_2Y_8(SiO_4)_6O_2$ ceramic pellet SPSed at 1400 ºC, (c) the pure $Sr_2Y_8(SiO_4)_6O_2$ powders obtained after solid state reaction, (d) the calculated pattern derived from refinement.

The morphology of the ball-milled $Sr_2Y_8(SiO_4)_6O_2$ powders is investigated by SEM and shown in Figure 5-2. The powder is homogeneous and well dispersed. The average particle size is estimated to be 0.77 μm. This uniform morphology in micrometer scale can be attributed to the employment of the nano-sized Y_2O_3 powder in the powder synthesis process. As the major component (~58 wt%) of the starting powders, the nano-

sized Y_2O_3 powders are helpful to form pure silicate oxyapatite phase during the solid state reaction process and also prevent the powders from aggregating and coarsening.

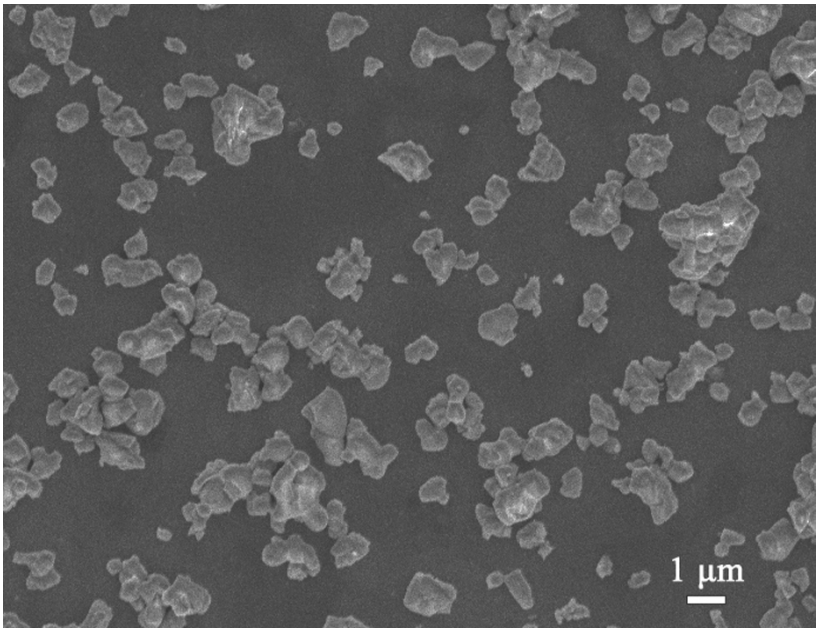

Figure 5-2 The morphology of the $Sr_2Y_8(SiO_4)_6O_2$ powders after 6-hours ball milling using zirconia balls and ethanol.

The shrinkage curves of ceramics during SPS are shown in Figure 5-3. The shrinkage process takes place at the heating temperature about 1200 ºC and continued until the temperature is raised to 1500 ºC. No further shrinkage is observed in dwell regions in sintering curves. The microstructure evolutions from 1100 ºC to 1500 ºC are shown in Figure 5-4 and the corresponding particle or grain sizes and relative densities are summarized in Figure 5-5. Microstructure of the ceramic SPS heated at 1100 ºC (Figure 5-4a) indicates that most powder particles are still separated from each other without condensation, which is in line with the shrinkage curve. The particle size is about 1.1 μm. Facets of some particles become obvious due to the surface diffusion [29] which takes place at early stage of sintering. When the heating temperature is increased to 1200 ºC, particles start to agglomerate with each other and condensation begins, though the pores are still continuous and the relative density is low. These continuous pores can effectively prevent the particles or grains from growth (Figure 5-5). One feature in this ceramic (Figure 5-4b

and c) is that the grain boundaries are not well-defined and some nano-clusters appear at the grain boundaries. This phenomenon was also observed during the SPS process of YAG and can be ascribed to the grain rotation and sliding aided by particle-surface softening.[15] The microstructure of the sample spark plasma sintered at 1300 ºC indicates a typical on-going condensation process. Most of the continuous pores are replaced by isolated ones which accommodate at the joints of grain boundaries and can be further reduced by curvature-driven grain boundary migration. The relative density is close to 90%, and the grain size grows to around 2 μm. Larger grains make the grain rotation and sliding less easier, therefore grain boundaries in Figure 5-4 become well-defined. The small particles inside some pores are caused by the polishing process in SEM sample preparation. For the sample heated at 1400 ºC, the relative density is 98.1%, and its grain size is 3.2 μm. Continuous pores are eliminated but some small pores at the joints of the grain boundaries still exist. When the ceramic is heated to 1500 ºC, its relative density can approach 99.3% and the grain size grows to about 3.8 μm. In this case, very small pores still can be observed in high magnifications.

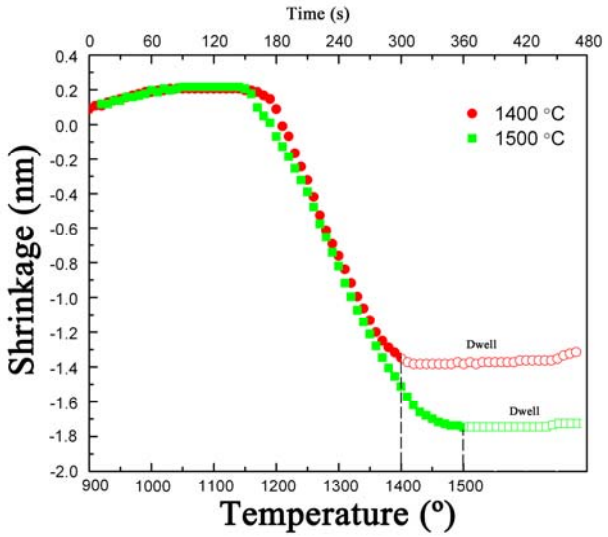

Figure 5-3 The shrinkage curves of $Sr_2Y_8(SiO_4)_6O_2$ SPSed at 1400 °C (circle) and 1500 °C (square). The shrinkages during the dwell region related to the time axis are plotted as open circles for 1400 °C and open squares for 1500 °C.

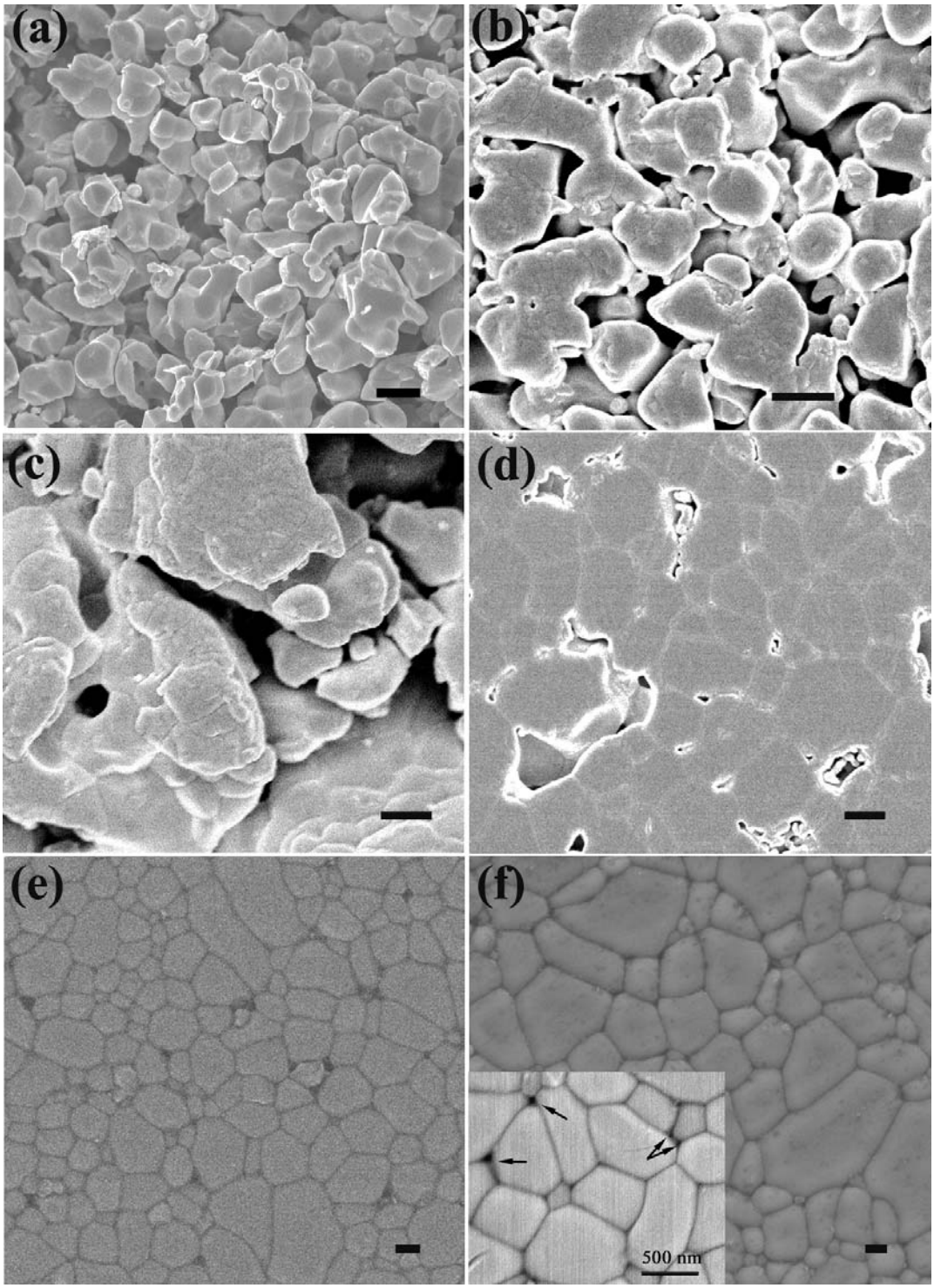

Figure 5-4 Microstructures of $Sr_2Y_8(SiO_4)_6O_2$ ceramic pellets SPSed at (a) 1100 ºC, (b) and (c) 1200 ºC, (d) 1300 ºC, (e) 1400 ºC and (f) 1500 ºC. All the scale bar represent for 1 μm. Fracture surfaces of samples SPSed at 1100 ºC and 1200 ºC are observed while samples SPSed at 1300 ºC, 1400 ºC and 1500 ºC are polished and heat-etched. Inset is the one with higher magnification. The pores are indicated by the arrows.

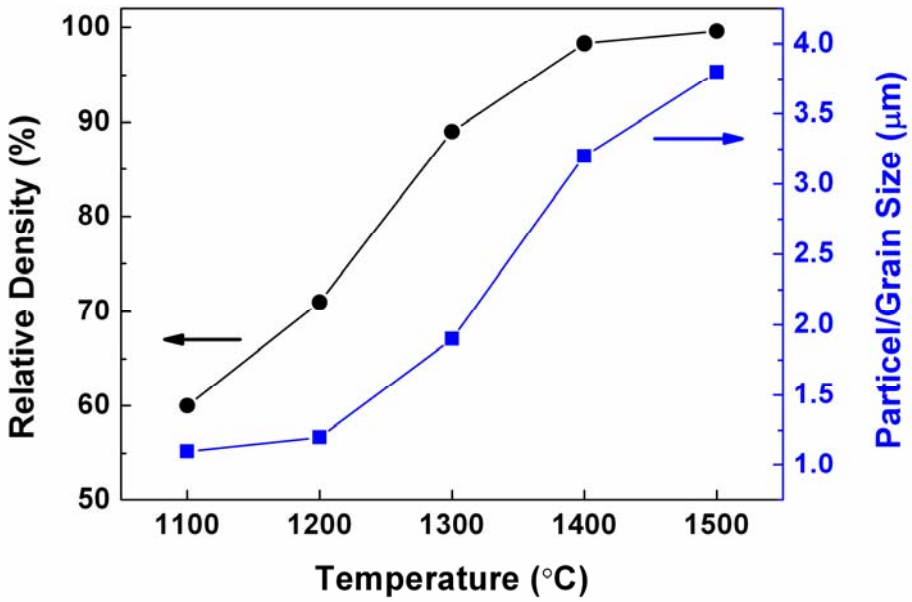

Figure 5-5 Variations of relative densities and grain sizes with the SPS temperatures.

5.3.2 Light transmittances analysis of ceramics SPSed at 1400 ºC and 1500 ºC

The features of microstructures of the ceramics sintered at 1400 ºC and 1500 ºC make them appropriate for comparison of the pore and grain effect on the light transmittances. The porosity of the 1400 ºC sintered ceramic, considered as the incompletely condensed sample, is 1.9% and almost three times of that in the 1500 ºC sintered one (0.7%) which is considered as the completely condensed sample. Based on the surface morphologies of these two samples (Figure 5-4), relatively high densities have also been displayed due to the closely compacted grains. In the 1400 ºC sintered sample large pores of about 580 nm are observed, which are comparable to the wavelength of the visible lights and result in strong scattering of incoming visible lights according to the Mie theory.[24] For the sample sintered at 1500 ºC, much less pores are exhibited under SEM, though some small pores with a size of about 80 nm are still visible. The average grain size of the ceramic sintered by SPS at 1500 ºC and 1400 ºC is 3.8 μm and 3.2 μm respectively.

The images of the ceramics sintered at 1400 ºC and 1500 ºC are shown in Figure 5-6. The sample sintered at 1400 ºC with SPS is opaque due to the existence of relatively large pores and high porosity. The sample sintered at 1500 ºC is translucent as the letters beneath can be displayed.

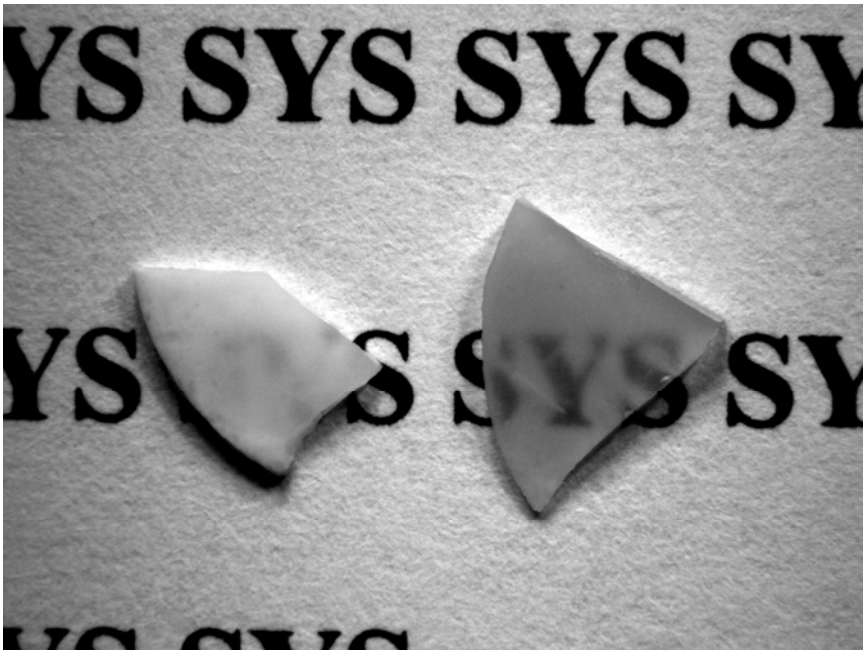

Figure 5-6 Images of the $Sr_2Y_8(SiO_4)_6O_2$ ceramic pellets SPSed at 1400 ºC (left) and 1500 ºC (right). The thicknesses of both samples are 0.8 mm.

The transmittance of the opaque sample is poor as the total forward and the in-line transmittances are almost zero. For the translucent one, both the total forward transmittance and the in-line transmittance are raised as the wavelength increases (Figure 5-7). In the infrared range, the total forward transmittance of the translucent sample reaches about 52% but the in-line transmittance is 3.2% at 800 nm which is relatively low. The large difference between the total forward transmittance and the in-line transmittance of the present sample implies that large fraction of the incoming light is deflected at the grain boundaries and the residual pores.

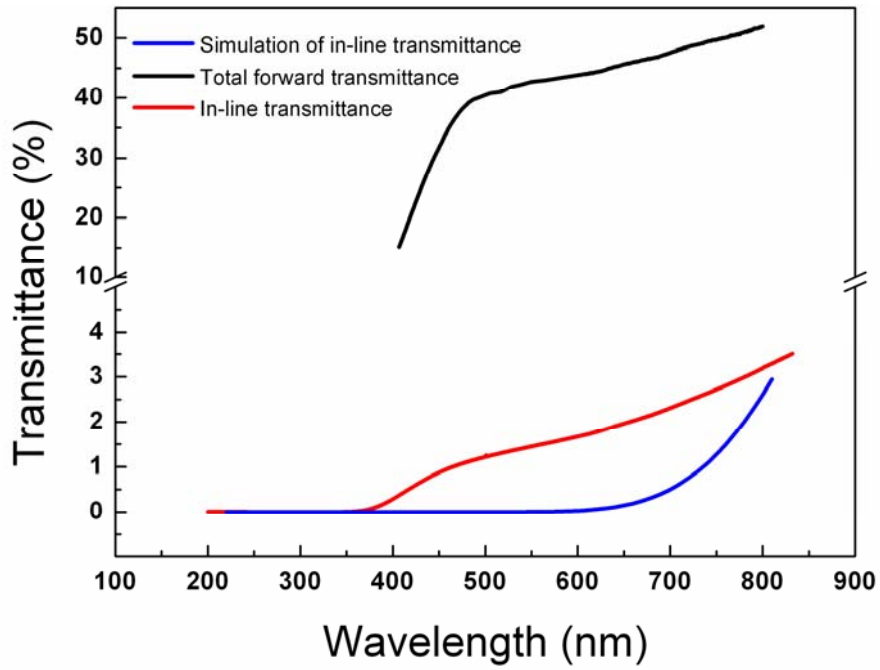

Figure 5-7 The transmittances of the 1500 °C SPSed $Sr_2Y_8(SiO_4)_6O_2$ with thickness 0.8 mm. The black line represents the total forward transmittance and the red line is the in-line transmittance. The blue line is the calculated in-line transmittance based on Mie theory and the parameters V_p = 0.7%, r_{bi} = 1.9 μm and r_{pore} = 40 nm.

The in-line transmittance T of a sample can be expressed as:

$$T = (1-R)^2 \exp(-C_{sca}t) \qquad \text{Equation 5-1}$$

where R is the reflectivity, C_{sca} is the effective scattering coefficient which consider all the scattering centers and t is the thickness of the sample. The reflectivity R can be derived from the reflective index of material n and the air $n' = 1$:

$$R = \frac{(n-n')^2}{(n+n')^2} \qquad \text{Equation 5-2}$$

The reflective index of $Sr_2Y_8(SiO_4)_6O_2$ is unavailable, so the data of n_o = 1.831 and n_e = 1.816 from a similar compound $Ca_2Y_8(SiO_4)_6O_2$ are used for approximation.[5] The R value turns out to be about 0.84. Due to the anisotropic properties of $Sr_2Y_8(SiO_4)_6O_2$, the C_{sca} should take the scattering by pores and by birefringence into account:

$$C_{sca} = C_{pore} + C_{bi} \qquad \text{Equation 5-3}$$

The effective scattering coefficient of pore C_{pore} can be expressed as:[30]

$$C_{pore} = N_{pore} G_{pore} Q_{pore} = \frac{3V_p}{4r_{pore}} Q_{pore} \qquad \text{Equation 5-4}$$

Where N_{pore} is the pore density, G_{pore} is the geometrical cross section of pore, r_{pore} is the radius of the pores, V_p is the porosity and Q_{pore} is th scattering efficiency of pore. The effective scattering coefficient of the birefringence can be calculated based on the model proposed by Apetz:[10]

$$C_{bi} = N_{bi} G_{bi} Q_{bi} = \frac{1}{2} \frac{1}{\frac{4}{3}\pi r_{bi}^3} Q_{bi} \qquad \text{Equation 5-5}$$

Where N_{bi} is the number of the scattering centers causing birefringence effect, G_{bi} is the geometrical cross section, r_{bi} is the radius of the scattering centers and Q_{bi} is the scattering efficiency. In order to further calculate the effective scattering coefficients of the birefringence C_{bi} and pores C_{pore} of the ceramics sintered at 1400 ºC and 1500 ºC, the results of the density measurements and the SEM images are utilized as: V_p (1500 ºC) = 0.7%, V_p (1400 ºC) = 1.9%, r_{bi} (1500 ºC) = 1.9 μm, r_{bi} (1400 ºC) = 1.6 μm, r_{pore} (1500 ºC) = 40 nm and r_{pore}(1400 ºC) = 580 nm. The calculated effective scattering coefficients of both ceramics samples are shown in Figure 5-8. The values of C_{bi} for the ceramics sintered at 1400 ºC and 1500 ºC are similar because of their similar grain sizes, which means the light scattering by the birefringence effect in both ceramic samples are almost the same. The values of C_{pore} are higher than the corresponding C_{bi} in both 1400 ºC and 1500 ºC sintered ceramics, indicating that more incoming light is scattered by residual pores. Obviously the value of C_{pore} for the sample sintered at 1400 ºC is most pronounced because of the higher porosity and larger pore size. So strong scattering of the incident light occurs and results in poor light transmittance of the sample.

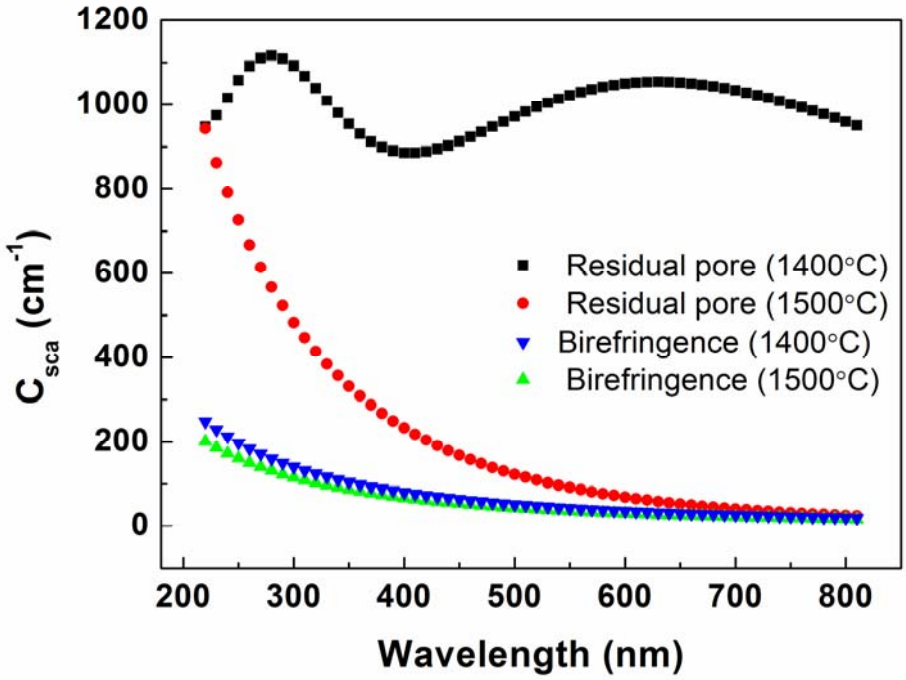

Figure 5-8 The effective scattering coefficients of residual pores (■) and birefringence (▼) in the ceramic SPSed at 1400 °C; The effective scattering coefficients of residual pores (●) and birefringence (▲) in the ceramic sintered at 1500 °C.

The in-line transmittance of the 1500 ºC sintered sample is simulated (Figure 5-7) according to Equation 5-1 by using the effective scattering coefficients obtained above. The difference of the experimental and simulated transmittance curves is small at the infrared region, but in the region with shorter wavelengths the simulation results underestimate the transmittance values. Same phenomenon was also reported [31] and it may be resulted from the usage of the average pore size in the calculation.

5.4 Conclusion

1. The translucent silicate oxyapatite $Sr_2Y_8(SiO_4)_6O_2$ ceramic with hexagonal crystal structure is successfully fabricated by employing the spark plasma sintering.

2. Microstructure evolutions of the ceramics during the sintering are investigated. With lower sintering temperatures like 1100 °C and 1200 °C, the relative densities of the ceramics are low and continuous pores exist which inhibits the particle or grain growth. When the sintering temperature is increase to 1300 °C or 1400 °C, relative densities are also increased and isolated pores and grain growth occurs inside the ceramics. When the sintering temperature reaches 1500 °C, translucent ceramic with 99.3% relative density is obtained.

3. The completely and incompletely condensed ceramic samples sintered by SPS are investigated. The densification process has not completed in the opaque ceramic sintered at 1400 °C. The ceramic sintered at 1500 °C is densified with about 0.7% porosity and appears translucent. The total forward transmittance is about 52% but the in-line transmittance is much lower due to the scattering effect of the residual pores. More quantitative calculation has revealed how the total forward transmittance is affected by both birefringence effect and residual pores.

5.5 References

1. B. Francois, M. Navizet, J. Rebreyend & C. Won, (1991). Monocrystals of Silicates of Lanthanides Usable as Scintillators for the Detection of X and Gamma Radiation. *US Patent*, 4988882.
2. F. Druon, S. Chenais & F. Raybaut, (2002). Apatite-structure Crystal, Yb^{3+}:$SrY_4(SiO_4)_3O$, for the Development of Diode-pumped Femtosecond Lasers. *Optics Letters*, 27 (21), 1914-1916.
3. F. Druon, F. Balembois & P. Georges, (2004). Ultra-short-pulsed and Highly-efficient Diode-pumped Yb : SYS Mode-locked Oscillators. *Optics Express*, 12 (20), 5005-5012.
4. U. Anselmi-Tamburini, J. Woolman & Z. Munir, (2007). Transparent Nanometric Cubic and Tetragonal Zirconia Obtained by High-pressure Pulsed Electric Current Sintering. *Advanced Functional Materials*, 17, 3267-3273.
5. K. B. Steinbruegge, T. Henningsen, R. H. Hopkins, R. Mazelsky, N. T. Melamed, E. P. Riedel & G. W. Roland, (1972). Laser Properties of Nd^{+3} and Ho^{+3} Doped Crystals with Apatite Structure. *Applied Optics*, 11 (5), 999-1012.
6. V. Lupei, A. Lupei & A. Ikesue, (2004). Single Crystal and Transparent Ceramic Nd-doped Oxide Laser Materials: a Comparative Spectroscopic Investigation. *Journal of Alloys and Compounds*, 380 (1-2), 61-70.
7. L. Mezeix & D. J. Green, (2006). Comparison of the Mechanical Properties of Single Crystal and Polycrystalline Yttrium Aluminum Garnet. *International Journal of Applied Ceramic Technology*, 3 (2), 166-176.
8. A. Ikesue & Y. L. Aung, (2006). Synthesis and Performance of Advanced Ceramic Lasers. *Journal of the American Ceramic Society*, 89 (6), 1936-1944.
9. K. Hayashi, O. Kobayashi, S. Toyoda & K. Morinaga, (1991). Transmission Optical-properties of Polycrystalline Alumina with Submicron Grains. *Materials Transactions JIM*, 32 (11), 1024-1029.
10. R. Apetz & M. P. B. Bruggen, (2003). Transparent Alumina: a Light-scattering Model. *Jounal of American Ceramics Society*, 86 (3), 480-486.
11. J. D. Kuntz, J. J. Roberts, M. Hough & N. J. Cherepy, (2007). Multiple Synthesis Routes to Transparent Ceramic Lutetium Aluminum Garnet. *Scripta Materialia*, 57 (10), 960-963.
12. S. H. Lee, E. R. Kupp, A. J. Stevenson, J. M. Anderson, G. L. Messing, X. Li, E. C. Dickey, J. Q. Dumm, V. K. Simonaitis-Castillo & G. J. Quarles, (2009). Hot Isostatic Pressing of Transparent Nd:YAG Ceramics. *Journal of the American Ceramic Society*, 92 (7), 1456-1463.
13. J. Lu, J. F. Bisson, K. Takaichi, T. Uematsu, A. Shirakawa, M. Musha, K. Ueda, H. Yagi, T. Yanagitani & A. A. Kaminskii, (2003). Yb^{3+}: Sc_2O_3 Ceramic Laser. *Applied Physics Letters*, 83 (6), 1101-1103.
14. M. Omori, (2000). Sintering, Consolidation, Reaction and Crystal Growth by the Spark Plasma System (SPS). 287 (2), 183-188.
15. R. Chaim, R. Marder-Jaeckel & J. Z. Shen, (2006). Transparent YAG Ceramics by Surface Softening of Nanoparticles in Spark Plasma Sintering. *Materials Science and Engineering A*, 429 (1-2), 74-78.
16. C. Wang & Z. Zhao, (2009). Transparent $MgAl_2O_4$ Ceramic Produced by Spark Plasma Sintering. *Scripta Materialia*, 61 (2), 193-196.
17. K. Morita, B. N. Kim, K. Hiraga & H. Yoshida, (2008). Fabrication of Transparent $MgAl_2O_4$ Spinel Polycrystal by Spark Plasma Sintering Processing. *Scripta Materialia*, 58 (12), 1114-1117.

18. A. Ikesue, T. Kinoshita, K. Kamata & K. Yoshida, (1995). Fabrication and Optical Properties of High-perforemance Polycrystalline Nd-YAG Ceramics for Solid-state Lasers. *Journal of the American Ceramic Society*, 78 (4), 1033-1040.
19. I. Shoji, S. Kurimura, Y. Sato, T. Taira, A. Ikesue & K. Yoshida, (2000). Optical Properties and Laser Characteristics of Highly Nd^{3+}-doped $Y_3Al_5O_{12}$ Ceramics. *Applied Physics Letters*, 77 (7), 939-941.
20. J. Kong, J. Lu, K. Takaichi, T. Uematsu, K. Ueda, D. Y. Tang, D. Y. Shen, H. Yagi, T. Yanagitani & A. A. Kaminskii, (2003). Diode-pumped Yb : Y_2O_3 ceramic laser. *Applied Physics Letters*, 82 (16), 2556-2558.
21. A. Shirakawa, K. Takaichi, H. Yagi, J. F. Bisson, J. Lu, M. Musha & K. Ueda, (2003). Diode-pumped Mode-locked Yb^{3+}: Y_2O_3 Ceramic Laser. *Optics Express*, 11 (22), 2911-2916.
22. A. Lempicki, C. Brecher, H. Lingertat, S. R. Miller, J. Glodo & V. K. Sarin, (2008). A Ceramic Cersion of the LSO Scintillator. *IEEE Transactions on Nuclear Science*, 55 (3), 1148-1151.
23. D. J. Wisniewski, L. A. Boatner, J. S. Neal, G. E. Jellison, J. O. Ramey, A. North, M. Wisniewska, A. E. Payzant, J. Y. Howe, A. Lempicki, C. Brecher & J. Glodo, (2008). Development of Novel Polycrystalline Ceramic Scintillators. *IEEE Transactions on Nuclear Science*, 55 (3), 1501-1508.
24. H. C. Van de Hulst, (1957). *Light Scattering by Small Particles*. New York: Wiley.
25. Craig F. Bohren & D. R. Huffman, (1983). *Absorption and Scattering of Light by Small Particles*. New York: Wiley.
26. M. Mendelso, (1969). Average Grain Size in Polycrystalline Ceramics. *Journal of the American Ceramic Society*, 52 (8), 443-446.
27. S. Prahl, (2007). *Mie Scattering Calculator*.
Available: http://omlc.ogi.edu/calc/mie_calc.html.
28. Y. Q. Shen, A. Tok, D. Y. Tang & Z. L. Dong, (2010). Synthesis and Crystal Structure Charactreization of Silicate Apatite $Sr_2Y_8(SiO_4)_6O_2$. *Journal of the American Ceramic Society*, 93 (4), 1176-1182.
29. S.-J. L. Kang, (2005). *Sintering-Densification, Grain Growth and Microstructure*. Oxford: Elsevier.
30. J. Peelen & R. Mestselaar, (1973). Light Scattering by Pores in Polycrystalline Materials: Transmission Properties of Alumina. *Journal of Applied Physics*, 45 (1), 216-220.
31. I. Yamashita, H. Nagayama & K. Tsukuma, (2008). Transmission Properties of Translucent Polycrystalline Alumina. *Journal of the American Ceramic Society*, 91 (8), 2611-2616.

Chapter 6 Photoluminescence of Ce^{3+} doped $Sr_2Y_8(SiO_4)_6O_2$ translucent ceramics

6.1 Introduction

In Chapter 5, the translucent ceramic of $Sr_2Y_8(SiO_4)_6O_2$ has been successfully fabricated. One of the applications for the translucent ceramics is the scintillators in biomedical imaging devices.[1, 2] For example, a translucent ceramic form of Ce^{3+} doped Lu_2SiO_5 was produced by hot pressing and demonstrated potential applications as the scintillators in CT system,[3] in which Ce^{3+} cations acted as luminescent centers. Generally the scintillation process consists of three parts: first the incoming radiation is absorbed and converted into electron-hole pairs, then the electron-hole pairs are transferred to the luminescent activators, finally the energy is emitted when the excited luminescent centers return to ground states radiatively.[4] Therefore, as involved in one of three key processes in scintillators, the luminescent properties of luminescent centers are important and would affect the whole energy conversion efficiency and overall performance as a scintillator. The Ce^{3+} cations are widely used dopants in scintillators as the 5*d*-4*f* transition of Ce^{3+} is parity allowed with intensive emission and the relatively short decay time (20~60 ns), which ensures fast response during imaging process.[5]

Ce^{3+} doped silicate apatite single crystals have been fabricated and patented as scintillators for X- and gamma-radiation.[6] However, very few studies on ceramic forms of silicate apatites have been reported. Moreover, spark plasma sintering with superior time-efficiency is seldom tried to fabricate ceramic optical materials. In the present work, translucent ceramics of Ce^{3+} doped silicate apatite, Ce^{3+}:$Sr_2Y_8(SiO_4)_6O_2$ are fabricated, and their photoluminescent properties are studied.

The rare earth cations have special electronic structures and some of their intra-4*f* or 5*d*-4*f* transitions [7] result in luminescence. The coordinating environments of rare earth

cations in the host materials have great influence on their electronic structures.[8] Therefore, even one type of rare earth cation could have different electronic structures as well as luminescent properties when occupying different cationic sites in one host material. More interestingly in some cases, the rare earth cations in two different sites will interact with each other strongly and result in the energy transfer process.[9] This phenomenon is attractive because it would not only affect the decay behavior and the chromaticity of the emitting light but also provide an opportunity to study the luminescent behavior in physics. Most of such phenomena occurred in the Eu^{2+} doped compounds (Eu^{2+} doped $Sr_5(PO_4)_2SiO_4$,[10] Rb_2ZnBr_4,[11] $Sr_2Si_5N_8$ [12] and Sr_2SiO_4 [13]).

Ce^{3+} is another interesting rare earth cation, which is widely utilized in lighting and imaging applications. The energy transfer exists in Ce^{3+} doped $Ba_2Ca(BO_3)_2$ [14] and Sr_3AlO_4F [15] as reported recently. However, few of them have studied the energy transfer rate between Ce^{3+} in apatite structures. In the present chapter, the energy transfer process is discovered between Ce^{3+} cations at different sites in Ce^{3+}:$Sr_2Y_8(SiO_4)_6O_2$ and the energy transfer rate is studied. The energy levels for Ce^{3+} at A^I and A^{II} sites are constructed by configurational coordinate model, after which the energy transfer behavior is investigated quantitatively by fitting the decay profiles.

6.2 Experimental procedures

Silicate oxyapatites $Sr_2Y_{8-x}Ce_x(SiO_4)_6O_2$ (x = 0.01, 0.05 and 0.1) powders were prepared through solid state reaction. Stoichiometric amount of $SrCO_3$ (>99.0%, Alfa Aesar), silica gel 60 (>99.0%, Fluka), CeO_2 (>99.95%, Sigma-Aldrich) and synthetic nano-sized Y_2O_3 were weighted with each batch of 4 grams. The synthesis of nano-sized Y_2O_3 powder was introduced in Chapter 3.[16] The powders were immersed in ethanol and horizontal ball milled for 12 hours, followed by drying at 70ºC overnight. The dried mixtures were heated to 1400ºC for 6 hours in a tube furnace with reduced atmosphere (95% N_2 + 5% H_2).

The resultant $Sr_2Y_8(SiO_4)_6O_2$ powders were further ball milled using zirconia balls and ethanol for 6 hours. The ceramics samples were fabricated by a SPS system (Sumitomo Coal Mining SPS system, Dr. Sinter Modal 1050, Japan). The samples were first heated to 600 ºC and stabilized for 1 minute. And then the temperature was increased with a heating rate of 100 ºC/min to 1500 ºC and dwelled for 3 minutes. During the whole process, the pressure applied on the graphite die was kept at 23 MPa and the temperature profile was monitored by a pyrometer. The as-received ceramic pellets were heat treated at 1200 ºC for 1 hour in a muffle furnace to remove the residual carbon on the surface as well as other defects. The surfaces of the two pellets were carefully polished by sand papers and diamond pastes to a thickness of about 1 mm. In order to minimize the amount of oxidized cerium cations, the pellets were heated at 1200 ºC for 2 hours in a tube furnace with reduced atmosphere. The densities were measured by Archimedes methods.

X-ray diffraction (XRD, D8 Advance, Bruker AXS, Karlsruhe, Germany) was used to study the phase compositions. The Cu*K*α radiation was used as the X-ray source and the operation was carried out at 40 kV and 40 mA with a 2θ step size of 0.02° and a scan rate of 2˚/min. The surface morphologies of the ceramics were observed using a JEOL JSM-6340F scanning electron microscope (SEM, Tokyo, Japan) with a field emission source.

The photoluminescence (PL) and photoluminescence excitation (PLE) spectra were collected by a Shimadzu RF-5301PC spectrophotometer.

Time-resolved photoluminescence with a resolution of 10 ps (PicoQuant PicoHarp 300) was conducted by time-correlated single photon counting technique at room temperature. The excitation source was the 295 nm pulse laser (100 fs, 80 MHz) from the third harmonic of the titanium sapphire laser (Chameleon, Coherent Inc.).

6.3 Results and discussion

6.3.1 Microstructure characteristics of Ce: $Sr_2Y_8(SiO_4)_6O_2$ apatites

The appearances of $Sr_2Y_{8-x}Ce_x(SiO_4)_6O_2$ (x = 0.01, 0.05 and 0.1) translucent ceramics with thickness of 1mm are shown in Figure 6-1 and the pattern beneath can be well displayed. The SEM images of the samples indicate these ceramics are well densified. Entrapped pores that usually act as the light scattering centers are invisible in SEM figures, indicating that most of the pores are removed by the fabrication process.

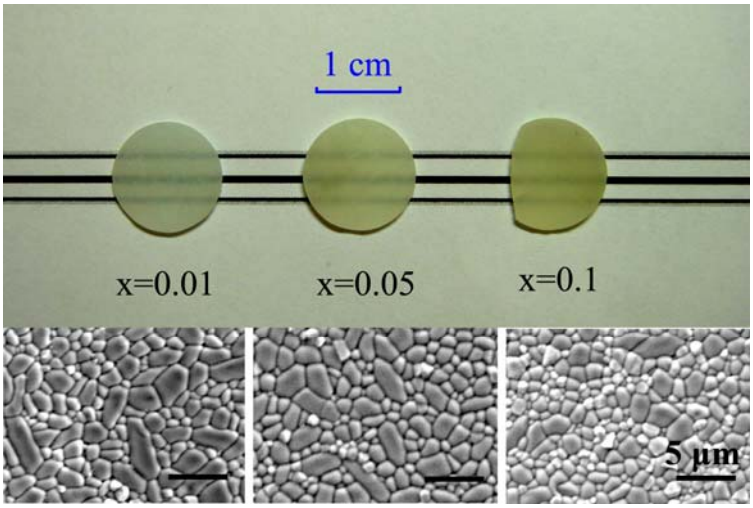

Figure 6-1 The appearances of $Sr_2Y_{7.99}Ce_{0.01}(SiO_4)_6O_2$ (left), $Sr_2Y_{7.95}Ce_{0.05}(SiO_4)_6O_2$ (middle) and $Sr_2Y_{7.9}Ce_{0.1}(SiO_4)_6O_2$ (right) and their corresponding SEM images. The scale bar in SEM image is 5 μm. The thicknesses of the samples are all about 1mm.

XRD patterns of $Sr_2Y_{8-x}Ce_x(SiO_4)_6O_2$ (x = 0.01, 0.05 and 0.1) translucent ceramics and the reference pattern of $Sr_2Y_8(SiO_4)_6O_2$ generated from the refinement are shown in Figure 6-2. The ceramics are all pure apatite phase and no peaks from impurities are detected. Enlarged patterns show that the XRD peaks shift to the lower 2θ values with the increase of Ce^{3+} content, indicating that larger Ce^{3+} cations have substituted Y^{3+} (r_{Ce3+} = 1.01 Å, r_{Y3+} = 0.9 Å when CN = 6). The heights of some peaks from the Rietveld calculated patterns do not match exactly with those from the experiments and that is

probably due to the preferred orientation existed inside the ceramic samples. Therefore, it is difficult to obtain reliable values of site occupancies of Ce^{3+}.

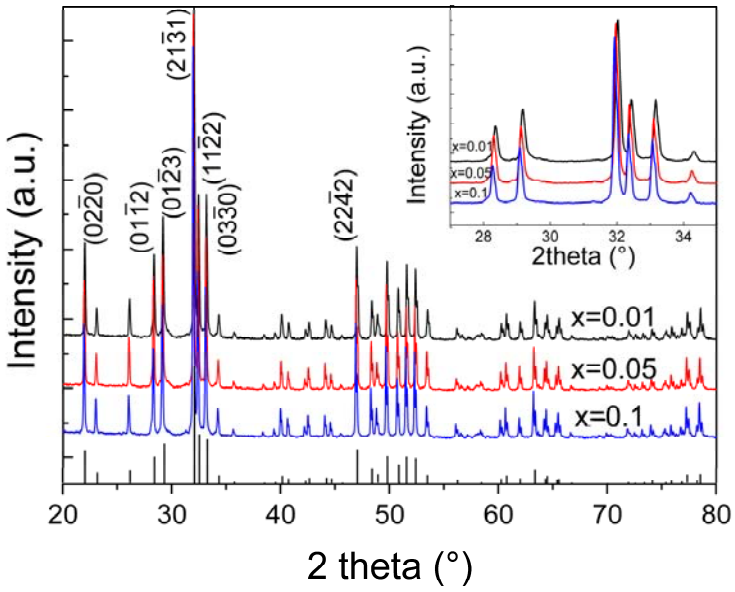

Figure 6-2 XRD for $Sr_2Y_{7.99}Ce_{0.01}(SiO_4)_6O_2$ (black), $Sr_2Y_{7.95}Ce_{0.05}(SiO_4)_6O_2$ (red) and $Sr_2Y_{7.9}Ce_{0.1}(SiO_4)_6O_2$ (blue). The XRD intensities of Sr_2Y_8 $(SiO_4)_6O_2$ from refinement are indicated at the bottom. The inset is the enlarged image in the 2θ range from 27 to 35°. The peaks are shifted to lower 2θ values when the Ce^{3+} doping concentration is increased.

6.3.2 Photoluminescence and photoluminescence excitation spectra of Ce: $Sr_2Y_8(SiO_4)_6O_2$ apatites and energy transfer of Ce^{3+} cations

The PL and PLE of $Sr_2Y_{8-x}Ce_x(SiO_4)_6O_2$ (x = 0.01, 0.05 and 0.1) translucent ceramics at room temperature are shown in Figure 6-3. All the broad bands in these spectra correspond to the electronic transition between 4*f* and 5*d* shells of Ce^{3+}. In the PL spectra of $Sr_2Y_{7.99}Ce_{0.01}(SiO_4)_6O_2$ excited by 320 nm, single band appears at 391 nm, which is ascribed to the transition from the lowest 5*d* state to 4*f* states at one crystallographic site. Although Ce^{3+} emission should be doublet as 4*f* states consist of two levels ^2F_J (J = 7/2 and 5/2), the single emission band in silicate apatite was observed by Lammers and Blasse [17] due to the structural disorder. Moreover, a shoulder at 424 nm has higher intensity in the PL spectra excited by 295 nm, which is related to the other crystallographic site. Based on the fact that Ce^{3+} ions prefer occupying the A^I sites according to Blasse's [18] and Felsche's [19] theories, the intense broad band at 391 nm

should correspond to electronic transitions of Ce^{3+} at A^I sites (Ce^{3+}(I)) and the shoulder at 424 nm corresponds to the small portion of Ce^{3+} occupying A^{II} sites (Ce^{3+}(II)). This designation is consistent with the results from the PLE spectra (Figure 6-3b). When the emission is monitored at 391 nm, single band at 320 nm appears in the PLE spectra which corresponds to the transition from the 4*f* to 5*d* state of Ce^{3+}(I). However, the spectra consist of a band at 320 nm and a shoulder at 295 nm if the emission is fixed at 424 nm because the overlap of the 424 nm emission from Ce^{3+}(I) and Ce^{3+}(II). Therefore, the wavelength of 295 nm corresponds to the excitation of Ce^{3+}(II) and its lower intensity is due to fewer Ce^{3+}(II) than Ce^{3+}(I) in the material. In all the PL and PLE spectra of $Sr_2Y_{7.95}Ce_{0.05}(SiO_4)_6O_2$ (Figure 6-3c and d), the characteristic bands related to Ce^{3+}(II) become pronounced though the intensities still lower than those of Ce^{3+}(I). It indicates that the site preference of Ce^{3+} to A^I sites maintains and the amount of Ce^{3+} cations occupying A^{II} sites increases when the cerium doping concentration is increased. As the spectra are deconvoluted by two-peak Gaussian fitting, it is obvious that the characteristic bands from Ce^{3+}(I) and Ce^{3+}(II) are overlapped when the sample is excited at 320 nm or the emission is monitored at 391 nm. That is why the PL spectra at 320 nm and PLE at 391 nm exhibit both Ce^{3+}(I) and Ce^{3+}(II) features. However, it is difficult to explain the existence of the band related to Ce^{3+}(II) in PL spectra when the excitation wavelength was 320 nm as the overlap of Ce^{3+}(II) is very limited. Most reasonable explanation for the phenomenon is the existence of energy transfer from Ce^{3+}(I) to Ce^{3+}(II). Part of the energy absorbed by Ce^{3+}(I) is transferred to Ce^{3+}(II), leading to the appearance of Ce^{3+}(II) band in PL when only Ce^{3+}(I) are excited. For $Sr_2Y_{7.9}Ce_{0.1}(SiO_4)_6O_2$ ceramic (Figure 6-3e and f), the PLE spectra monitored at 391 and 424 nm are similar to those of $Sr_2Y_{7.95}Ce_{0.05}(SiO_4)_6O_2$, in line with the preference of Ce^{3+} to A^I. The band of Ce^{3+}(II) (424 nm) gain higher intensity than the one of Ce^{3+}(I) (391 nm) in the PL spectra excited at 320 nm, which substantiate the existence of the energy transfer from Ce^{3+}(I) to Ce^{3+}(II).

As Ce^{3+} concentration increases, the probability of the energy transfer is increased and a large amount of energy is transferred from Ce^{3+}(I) to Ce^{3+}(II), leading to higher intensity of Ce^{3+}(II) than that of Ce^{3+}(I).

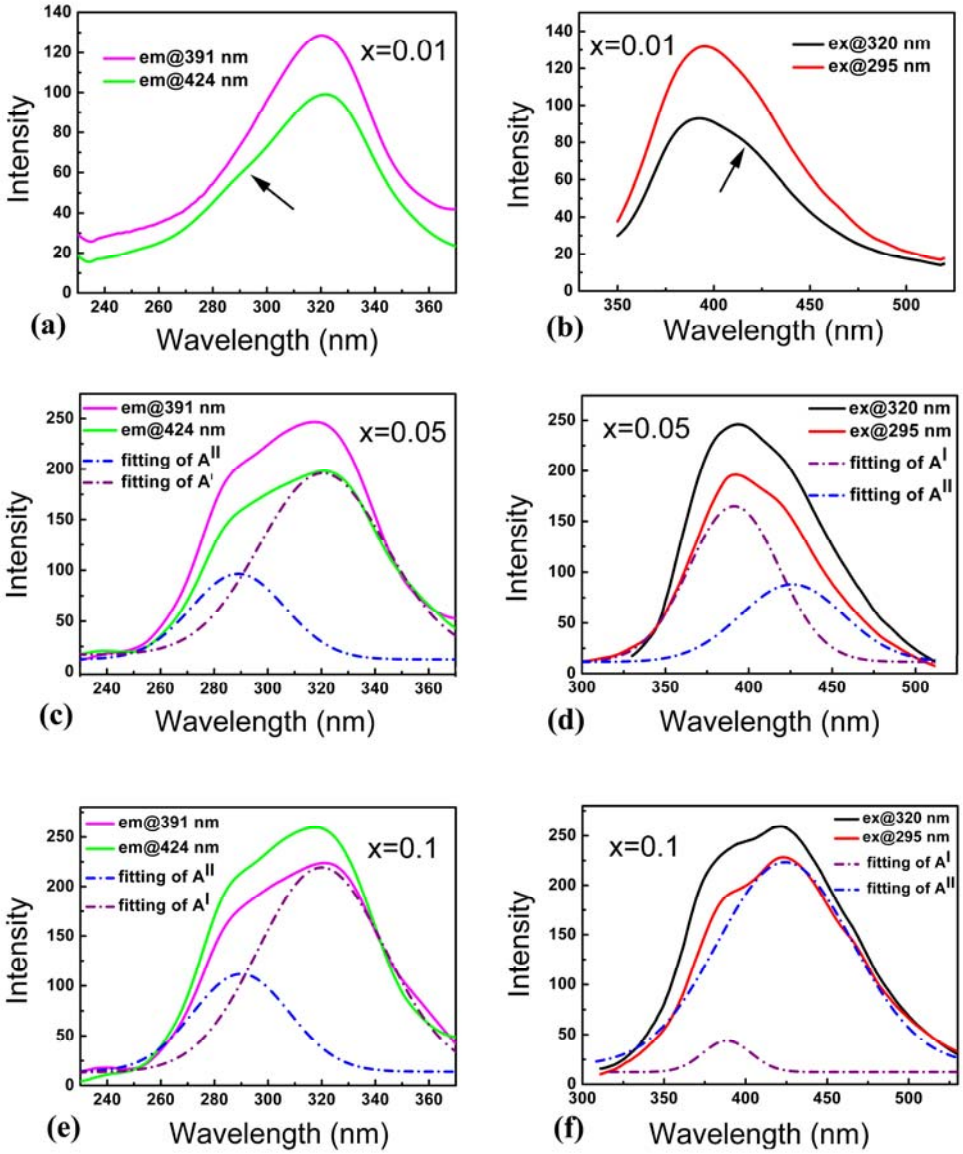

Figure 6-3 PL and PLE spectra and the results of Gaussian fittings. (a) PLE of $Sr_2Y_{7.99}Ce_{0.01}(SiO_4)_6O_2$; (b) PL and Gaussian fittings of $Sr_2Y_{7.99}Ce_{0.01}(SiO_4)_6O_2$; (c) PLE and Gaussian fittings of $Sr_2Y_{7.95}Ce_{0.05}(SiO_4)_6O_2$; (d) PL and Gaussian fittings of $Sr_2Y_{7.95}Ce_{0.05}(SiO_4)_6O_2$; (e) PLE and Gaussian fittings of $Sr_2Y_{7.9}Ce_{0.1}(SiO_4)_6O_2$; (d) PL and Gaussian fittings of $Sr_2Y_{7.9}Ce_{0.1}(SiO_4)_6O_2$. The shoulders corresponding to $Ce^{3+}(A^{II})$ site in (a) and (b) are indicated by arrows.

The appearance of $Sr_2Y_{7.9}Ce_{0.1}(SiO_4)_6O_2$ under 320 nm excitation is shown in Figure 6-4. The sample is placed in the PL machine and the emission source is indicated. Strong blue emission is observed from the ceramic pellet.

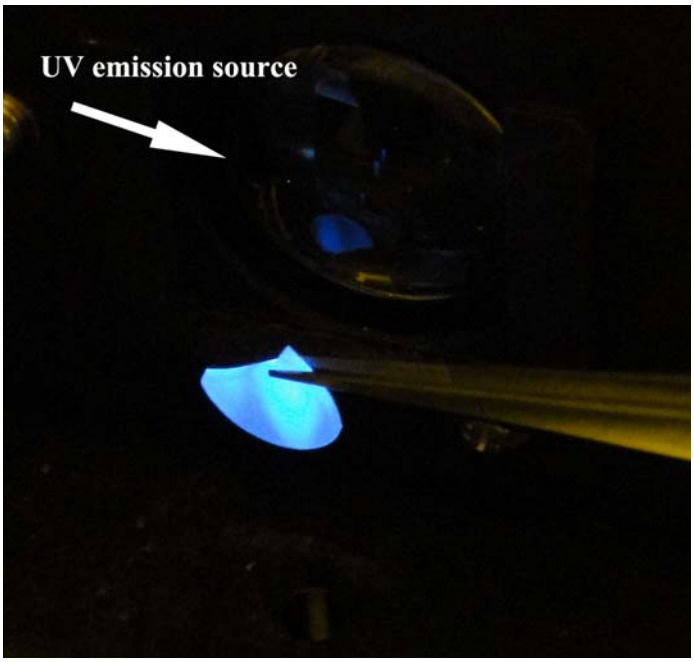

Figure 6-4 The appearance of $Sr_2Y_{7.9}Ce_{0.1}(SiO_4)_6O_2$ with excitation at 320 nm in the PL machine. The emission source is indicated.

According to the analysis of the PL and PLE spectra, the energy levels of Ce^{3+} at A^I and A^{II} sites are demonstrated by the configurational coordinate model (Figure 6-5). The parabolas stand for the lowest 5*d* states of Ce^{3+}(I) and Ce^{3+}(II) are different due to the coordination environments. The 4*f* states are well shielded by outer electrons and can be considered as constant in different environments.[9] Based on the PL and PLE spectra, the stokes shifts of Ce^{3+}(I) and Ce^{3+}(II) are 5675 and 10313 cm^{-1}. The larger stokes shift of Ce^{3+}(II) than Ce^{3+}(I) can be explained by the larger parabola offset ΔR for Ce^{3+}(II), which indicates that the environment around A^{II} site is less stiff than that around A^I. Moreover, the parabola of Ce^{3+}(II) lies at lower position than that of Ce^{3+}(I) due to the nephelauxetic effect and the crystal filed.[9] The free-oxygen closely bonded to A^{II} site not only increases the covalency of the Ce^{3+}−O bond but also enhances the crystal field at A^{II} site, both of which can lower the 5*d* levels of Ce^{3+}(II).

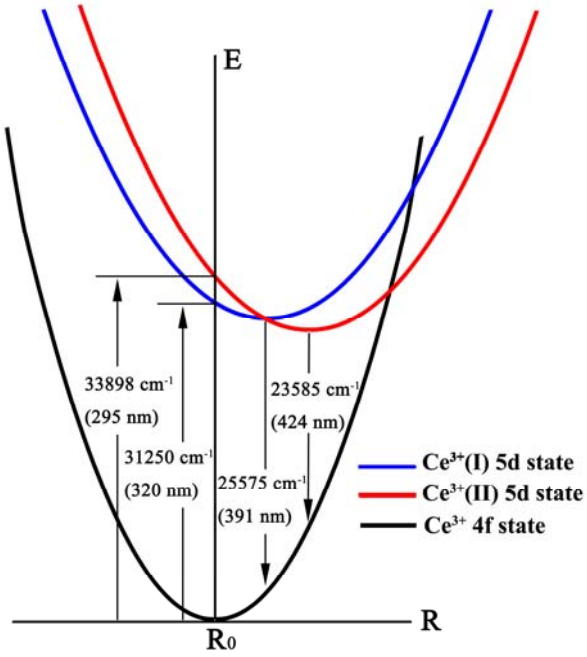

Figure 6-5 The configurational coordinate model of the energy levels for Ce^{3+}(I) and Ce^{3+}(II). Blue and red parabola represent the 5*d* states of Ce^{3+}(I) and Ce^{3+}(II) respectively. The 4*f* states (black parabola) of Ce^{3+}(I) and Ce^{3+}(II) are the same because 4*f* are well shielded by outer shell electrons.

6.3.3 Decay behaviors of Ce^{3+} cations in Ce: $Sr_2Y_8(SiO_4)_6O_2$ translucent ceramics

To further study the photoluminescence mechanisms, the time resolved decay profiles of $Sr_2Y_{8-x}Ce_x(SiO_4)_6O_2$ (x = 0.01, 0.05 and 0.1) ceramics are measured (Figure 6-6). The emissions related to Ce^{3+}(I) and Ce^{3+}(II) are monitored at 370 and 435 nm respectively, in order to minimize the spectra overlap between Ce^{3+}(I) and Ce^{3+}(II). Due to the energy transfer process as discussed above, the decay profiles are not single-exponential. Since the transition from Ce^{3+} 5*d* to 4*f* states is parity allowed and the emission of Ce^{3+}(I) overlaps in the excitation spectra of Ce^{3+}(I) and Ce^{3+}(II), the energy transfer is dipole-dipole interaction with Ce^{3+}(I) acting as the donors and both Ce^{3+}(I) and Ce^{3+}(II) as the acceptors. Moreover, these ceramics always contain some defects.[20,21] Assuming that the energy of Ce^{3+} cations near defects is totally vanished, the rate equation to describe the population change of the excited Ce^{3+}(I) and Ce^{3+}(II) can be expressed as:

$$\frac{dN_I}{dt} = -N_I/\tau_0 - \eta W_I N_I - W_{II} N_I \qquad \text{Equation 6-1}$$

$$\frac{dN_{II}}{dt} = -N_{II}/\tau_0' + W_{II} N_I \qquad \text{Equation 6-2}$$

where N_I and N_{II} are the populations of the excited Ce^{3+}(I) and Ce^{3+}(II), τ_0 and τ_0' are the corresponding radiative decay times, W_I and W_{II} are the energy transfer rates from Ce^{3+}(I) to Ce^{3+}(I) and Ce^{3+}(II) respectively, η is the fraction of the population of Ce^{3+}(I) near the defects over the total Ce^{3+}(I) population.

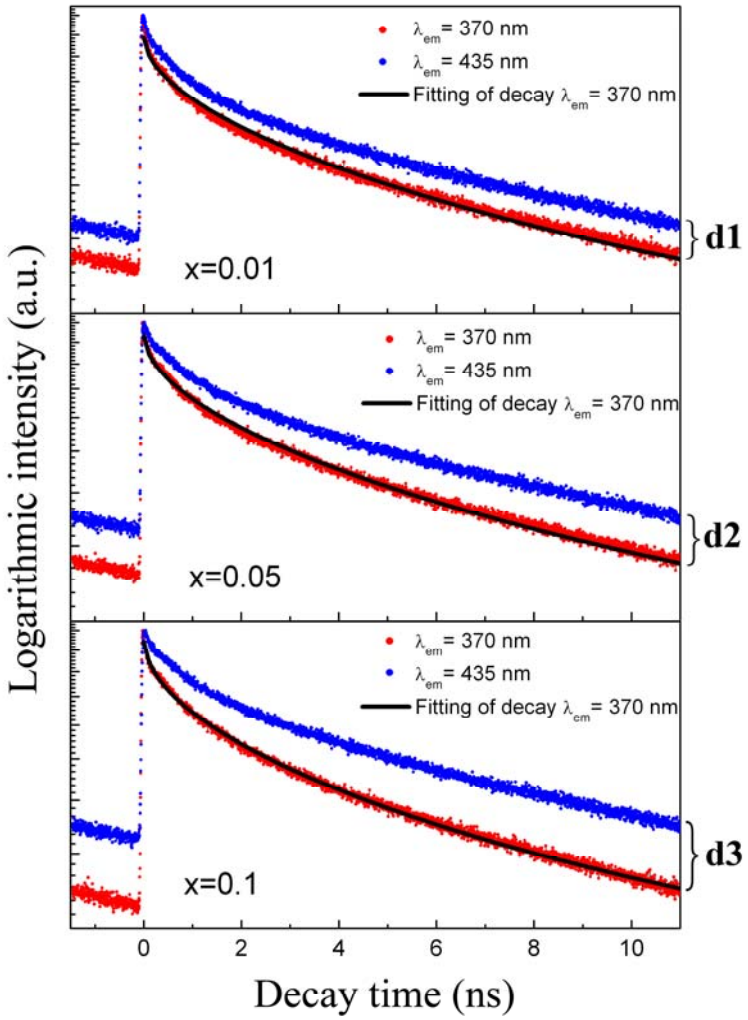

Figure 6-6 The decay profiles of the emission monitored at 370 nm (red) and 435 nm (blue) and the resulted curve from the global fitting of the decay profiles monitored the emission at 370 nm (black). The emissions of 435 nm decay slower than those of 370 nm in all the samples. The differences between the 435 nm and 370 nm decay profiles at 11 ns are indicated as d1, d2 and d3 for samples with x = 0.01, 0.05 and 0.1 respectively. The differences are enlarged when Ce^{3+} doping concentration increases.

Since τ is proportional to λ^2,[22] the relation between τ_0 and τ_0' can be estimated as $\tau_0' = 1.18\tau_0$ according to the emission wavelength relationships of Ce^{3+}(I) and Ce^{3+}(II). Therefore, the radiative decay time of excited Ce^{3+}(I) is shorter than that of Ce^{3+}(II) and the decay of Ce^{3+}(I) is even faster if taking the energy transfer process (Equation 3-1 and 3-2) into account (Figure 6-6). Moreover, the differences between the decay profiles at 370 and 435 nm are enlarged with the increase of the Ce^{3+} concentration, because the energy transfer process becomes more pronounced in higher Ce^{3+} concentration.

The decay monitored at 370 nm as related to Ce^{3+}(I) is further analyzed based on the Powell and Blasse's theory.[23, 24] The energy transfer rates W_I and W_{II} can be described as:

$$W_I = \frac{2}{3}\pi^{3/2} R_I^3 \, n_a^I / (\tau_0 t)^{1/2} \qquad \text{Equation 6-3}$$

$$W_{II} = \frac{2}{3}\pi^{3/2} R_{II}^3 \, n_a^{II} / (\tau_0 t)^{1/2} \qquad \text{Equation 6-4}$$

where n_a^I (or n_a^{II}) is the population density of acceptors (population of Ce^{3+}(I) or Ce^{3+}(II) in the unit volume), R_I and R_{II} are the critical distances for the energy transfer from Ce^{3+}(I) to Ce^{3+}(I) and Ce^{3+}(II) respectively. When the acceptor and the donor are separated with the critical distance, the energy transfer rate equals to the donor's radiative rate. In the case of electric-dipole interaction, the critical distance can be calculated as:[25]

$$R^6 = 0.63\times10^{28} \cdot Q_s \cdot \int f(E)F(E)E^{-4}\mathrm{d}E \qquad \text{Equation 6-5}$$

Where Q_s is the absorption strength of the donor, the integral represents the normalized spectra overlap of the emission of the donor and the excitation of the acceptor. The critical distance R_I for the energy transfer between Ce^{3+}(I) cations as estimated from the PL and PLE spectra is about 23.9 Å, which is in the reasonable range as compared to other studies.[26, 27] The critical distance for the energy transfer from Ce^{3+}(I) to Ce^{3+}(II) cations is about 6.7 Å due to smaller spectra overlap. By defining of a parameter C:

$$C = \frac{4}{3}\eta\pi^{3/2} R_I^3 \, n_a^I / (\tau_0)^{1/2} + \frac{4}{3}\pi^{3/2} R_{II}^3 \, n_a^{II} / (\tau_0)^{1/2} \qquad \text{Equation 6-6}$$

the solution of Equation 6-1 can be exhibited in a simplified form as:

$$N_{\mathrm{I}} = N_0^{\mathrm{I}} \exp(-t/\tau_0 - Ct^{1/2}) \qquad \text{Equation 6-7}$$

Therefore, the emission of Ce^{3+}(I) as a function of time can be expressed in the same way:

$$I_{\mathrm{I}} = I_0^{\mathrm{I}} \exp(-t/\tau_0 - Ct^{1/2}) \qquad \text{Equation 6-8}$$

I_0^{I} value equals to the emission intensity when t = 0. All the decay profiles are global fitted by Equation 6-8 with τ_0 as the shared value. Subsequently the radiative decay time and the parameter *C* for samples with different Ce^{3+} concentrations are obtained (Table 6-1). The radiative decay time turns out to be 31.6 ns which is comparable to the values of other Ce^{3+} doped apatites.[28,29] The *C* value increases with the Ce^{3+} concentration because the n_a^{I} and n_a^{II} are increased. Although it is difficult to accurately determine the value of n_a^{I} and n_a^{II}, they can be estimated by analyzing the Gaussian deconvoluted PL and PLE spectra (Figure 6-3). Both Ce^{3+}(I) and Ce^{3+}(II) cations can be excited at 295 nm and their radiative emissions intensities are designated as I_{PL}^{I} and I_{PL}^{II} respectively in the PL spectra. The energy supplies for the radiative emission of Ce^{3+}(II) come from two ways: one is excitation energy absorbed by Ce^{3+}(II) initially and the other is the energy transferred from Ce^{3+}(I). These two mechanisms are reflected in the PLE spectra as two bands with intensities of I_{PLE}^{I} and I_{PLE}^{II} when the Ce^{3+}(II) emission at 424 nm is monitored. Therefore the total contribution of the Ce^{3+}(I) to the PL is $I_{PL}^{I} + I_{PL}^{II} \times \frac{I_{PLE}^{I}}{I_{PLE}^{I} + I_{PLE}^{II}}$ and that of the Ce^{3+}(II) is $I_{PL}^{II} \times \frac{I_{PLE}^{II}}{I_{PLE}^{I} + I_{PLE}^{II}}$. The ratio of these two values approximates to the ratio of Ce^{3+}(I) and Ce^{3+}(II) populations contributing to the emission $N_{em}^{\mathrm{I}}/N_{em}^{\mathrm{II}}$:

$$\begin{aligned} N_{em}^{I}/N_{em}^{II} &= (I_{PL}^{I} + I_{PL}^{II} \times \frac{I_{PLE}^{I}}{I_{PLE}^{I} + I_{PLE}^{II}}) / (I_{PL}^{II} \times \frac{I_{PLE}^{II}}{I_{PLE}^{I} + I_{PLE}^{II}}) \\ &= (\frac{I_{PL}^{I}}{I_{PL}^{II}} + \frac{1}{1 + I_{PLE}^{II}/I_{PLE}^{I}}) / (\frac{1}{1 + I_{PLE}^{I}/I_{PLE}^{II}}) \end{aligned} \qquad \text{Equation 6-9}$$

Assuming that both Ce^{3+} (I) and Ce^{3+} (II) cation distributions are uniform, the total numbers of Ce^{3+} (A^I) and Ce^{3+} (A^{II}) are:

$N^I = N_{em}{}^I/(1-\eta)$, and Equation 6-10a

$N^{II} = N_{em}{}^{II}/(1-\eta)$ Equation 6-10b

respectively. According to the concept of $n_a{}^I$ and $n_a{}^{II}$, the ratio of them is:

$n_a{}^I/n_a{}^{II} = N^I/N^{II} = N_{em}{}^I/N_{em}{}^{II}$ Equation 6-11

which can be derived from the spectra intensities. Moreover, the total numbers of Ce^{3+} in the unit volume can be derived by:

$n = n_a{}^I + n_a{}^{II} = \rho x N_A/M$ Equation 6-12

where ρ is the density of the sample, x is the value in the formula $Sr_2Y_{8-x}Ce_x(SiO_4)_6O_2$ and M is the corresponding molecular weight. After obtaining the values of $n_a{}^I$ and $n_a{}^{II}$, the energy transfer rates and the values η of $Sr_2Y_{7.9}Ce_{0.1}(SiO_4)_6O_2$ and $Sr_2Y_{7.95}Ce_{0.05}(SiO_4)_6O_2$ are calculated subsequently by the Equation 6-3, 6-4 and 6-5 and listed in Table 6-2. The Ce^{3+}(I)→Ce^{3+}(II) energy transfer rate in $Sr_2Y_{7.9}Ce_{0.1}(SiO_4)_6O_2$ is about four times higher than that in $Sr_2Y_{7.95}Ce_{0.05}(SiO_4)_6O_2$, which supports the observation of high Ce^{3+}(II) intensity in $Sr_2Y_{7.9}Ce_{0.1}(SiO_4)_6O_2$ PL spectra when Ce^{3+}(I) is excited. Moreover, the η values show that about 20% of the excitation energy is absorbed by the defects and vanishes nonradiatively. As the Ce doping concentration is too low in $Sr_2Y_{7.99}Ce_{0.01}(SiO_4)_6O_2$ and the characteristics bands for Ce^{3+}(II) in PL and PLE spectra are weak, it is difficult to determine the population densities from its spectra.

Table 6-1 The global fitting results of the decay profiles

x	*C*	τ_0/ns	R^2
0.01	0.3644	31.6	0.9953
0.05	0.3721		
0.1	0.4237		

Table 6-2 Parameters used to analyze the decay profiles

x	$I^{I}_{PLE} / I^{II}_{PLE}$	I^{I}_{PL} / I^{II}_{PL}	N^{I}_{em}/N^{II}_{em}	n ($\times 10^{25}$)	ρ (g/cm^3)
0.05	2.06	1.87	7.27	9.6	4.671
0.1	1.96	0.20	2.55	19.1	4.673
	n_a^{I} ($\times 10^{25}$)	n_a^{II} ($\times 10^{25}$)	W_I (ns^{-1})	W_{II} (ns^{-1})	η (%)
0.05	8.45	1.09	0.7614 $t^{-1/2}$	0.0022 $t^{-1/2}$	24.2
0.1	13.69	5.38	1.2333 $t^{-1/2}$	0.0107 $t^{-1/2}$	16.3

The decay time is an important criterion for the scintillator materials because fast decay can increase the response and the resolution of scintillators. Normally scintillation decay under high energy irradiation such as X-ray and gamma-ray involve two processes: delivery of the absorbed energy to the luminescent centers and radiative emission from luminescent centers. Therefore, rapid luminescent decay is necessary for a fast-responding scintillator. The mean luminescent decay times at emission 370 nm for $Sr_2Y_{8-x}Ce_x(SiO_4)_6O_2$ (x = 0.01, 0.05 and 0.1) ceramics are estimated by:

$$\tau_m = \int_0^\infty tI(t)\mathrm{d}t \Big/ \int_0^\infty I(t)\mathrm{d}t \qquad \text{Equation 6-13}$$

The calculated results show that the mean photoluminescent decay times are 13.5, 13.28 and 11.9 ns for $Sr_2Y_{7.99}Ce_{0.01}(SiO_4)_6O_2$, $Sr_2Y_{7.95}Ce_{0.05}(SiO_4)_6O_2$ and $Sr_2Y_{7.9}Ce_{0.1}(SiO_4)_6O_2$ respectively. These values of decay time are shorter than Ce^{3+} doped single crystal scintillators such as $Ce:Lu_2Si_2O_7$ (38 ns),[30] $Ce:LuAlO_3$(17 ns) [31] and $Ce:Y_3Al_5O_{12}$ (60 ns) [32]. The decay times of commercialized scintillators $Bi_4Ge_3O_{12}$ and Tl:CsI are 300 ns and 550 ns respectively,[32,33] which are even longer comparing to those of Ce^{3+} doped $Sr_2Y_8(SiO_4)_6O_2$ ceramics. Therefore, fast decay behavior demonstrates that Ce^{3+} doped

$Sr_2Y_8(SiO_4)_6O_2$ ceramics are potential candidates as scintillators. Detailed studies with X-ray and gamma-ray irradiation are under going.

6.4 Conclusion

1. Ce^{3+} doped $Sr_2Y_8(SiO_4)_6O_2$ translucent ceramics are fabricated by solid state reaction and spark plasma sintering. The grains in the ceramics are closely compacted and the entrapped pores are invisible under SEM.

2. Ce^{3+} cations occupy two different sites A^I and A^{II} in $Sr_2Y_8(SiO_4)_6O_2$ crystal structure with the site preference to A^I. The different coordination environments of Ce^{3+} result in different photoluminescence features in the spectra. Ce^{3+} at A^I site can be excited with 320 nm radiation and the emission band peaks at 391 nm, while Ce^{3+} at A^{II} site can be excited at 295 nm and the emission band peaks at 420 nm. Based on the analysis of the photoluminescence, the energy levels of Ce^{3+} at A^I and A^{II} sites are demonstrated by the configurational coordinate model. Moreover, the energy transfer from Ce^{3+}(I) to Ce^{3+}(II) is revealed.

3. The energy transfer from Ce^{3+}(I) to Ce^{3+}(II) is electric-dipole interaction, which is faster in the ceramic with higher Ce^{3+} doping concentration due to the higher acceptor Ce^{3+}(II) population density. Quantitative analysis of ceramics $Sr_2Y_{7.95}Ce_{0.05}(SiO_4)_6O_2$ and $Sr_2Y_{7.9}Ce_{0.1}(SiO_4)_6O_2$ shows the radiative decay time for Ce^{3+}(I) is 31.6 ns and the Ce^{3+}(I)→Ce^{3+}(II) energy transfer rate in $Sr_2Y_{7.9}Ce_{0.1}(SiO_4)_6O_2$ is about four times higher than that in $Sr_2Y_{7.95}Ce_{0.05}(SiO_4)_6O_2$.

6.5 References

1. D. J. Wisniewski, L. A. Boatner, J. S. Neal, G. E. Jellison, J. O. Ramey, A. North, M. Wisniewska, A. E. Payzant, J. Y. Howe, A. Lempicki, C. Brecher & J. Glodo, (2008). Development of Novel Polycrystalline Ceramic Scintillators. *IEEE Transactions on Nuclear Science*, 55 (3), 1501-1508.
2. A. Lempicki, C. Brecher, P. Szupryczynski, H. Lingertat, V. V. Nagarkar, S. V. Tipnis & S. R. Miller, (2002). A New Lutetia-based Ceramic Scintillator for X-ray Imaging. *Nuclear Instruments & Methods in Physics Research Section A*, 488 (3), 579-590.
3. A. Lempicki, C. Brecher, H. Lingertat, S. R. Miller, J. Glodo & V. K. Sarin, (2008). A Ceramic Version of the LSO Scintillator. *IEEE Transactions on Nuclear Science*, 55 (3), 1148-1151.
4. G. Blasse, (1994). Scintillator Materials. *Chemistry of Materials*, 6 (9), 1465-1475.
5. H. H. Lin, H. B. Liang, B. Han, J. P. Zhong, Q. Su, P. Dorenbos, M. D. Birowosuto, G. B. Zhang, Y. B. Fu & W. Q. Wu, (2007). Luminescence and Site Occupancy of Ce^{3+} in $Ba_2Ca(BO_3)_2$. *Physical Review B*, 76 (3).
6. B. Francois, M. Navizet, J. Rebreyend & C. Won, (1991). Monocrystals of Silicates of Lanthanides Usable as Scintillators for the Detection of X and Gamma radiation. *US Patent*, 4988882.
7. L. van Pieterson, M. F. Reid, R. T. Wegh, S. Soverna & A. Meijerink, (2002). 4*f*(n)-> 4*f*(n)-(1)5*d* Transitions of the Light Lanthanides: Experiment and Theory. *Physical Review B*, 65 (4), 045114.
8. W. M. Yen, S. Shionoya & H. Yamamoto, (2006). *Phosphor Handbook*. Boca Raton: CRC Press.
9. G. Blasse & B. C. Grabmajer, (1994). *Luminescent Materials*. Berlin: Springer-Verlag.
10. G. Blasse & A. Bril, (1969). Energy Transfer between Eu^{2+} Ions in Nonequivalent Sites in Strontium-silicate-phosphate. *Physics Letters*, 28A (8), 527-528.
11. G. Blasse, (1986). Energy Transfer between Inequivalent Eu^{2+} Ions. *Journal of Solid State Chemistry*, 62, 207-211.
12. K. S. Sohn, B. Lee, R. J. Xie & N. Hirosaki, (2009). Rate-equation Model for Energy Transfer between Activators at Different Crystallographic Sites in $Sr_2Si_5N_8:Eu^{2+}$. *Optics Letters*, 34 (21), 3427-3429.
13. D. Ahn, N. Shin, K. D. Park & K. S. Sohn, (2009). Energy Transfer between Activators at Different Crystallographic Sites. *Journal of the Electrochemical Society*, 156 (9), 242-248.
14. H. H. Lin, H. B. Liang, Z. F. Tian, B. Han, J. Wang, Q. Su & G. B. Zhang, (2009). Luminescent of $Ba_2Ca(BO_3)_2:Ce^{3+}$-Influence of Charge Compensator, Energy Transfer and LED Application. *Journal of Physics D*, 42, 165409-165417.
15. W. P. Chen, H. B. Liang, H. Y. Ni, P. He & Q. Su, (2010). Chromaticity-tunable Emission of $Sr_3AlO_4F:Ce^{3+}$ Phosphor: Correlation with Matrix Structure and Application in LEDs. *Journal of the Electrochemical Society*, 157 (3), 159-163.
16. Y. Q. Shen, A. Tok, D. Y. Tang & Z. L. Dong, (2010). Synthesis and Crystal Structure Charactreization of Silicate Apatite $Sr_2Y_8(SiO_4)_6O_2$. *Journal of the American Ceramic Society*, 93 (4), 1176-1182.
17. M. J. J. Lammers & G. Blasse, (1987). Luminescence of Tb^{3+}-activated Rare-earth Silicates. *Journal of the Electrochemical Society*, 134 (8A), 2068-2072.
18. G. Blasse, (1975). Influence of Local Charge Compensation on Site Occupation and Luminescence of Apatites. *Journal of Solid State Chemistry*, 14 (2), 181-184.

19. J. Felsche, (1972). Rare-earth Silicates with Apatite Structure. *Journal of Solid State Chemistry*, 5 (2), 266-275.
20. E. Zych, C. Brecher & J. Glodo, (2000). Kinetics of Cerium Emission in a YAG:Ce Single Crystal: the Role of Traps. *Journal of Physics-Condensed Matter*, 12 (8), 1947-1958.
21. E. Zych, C. Brecher, A. J. Wojtowicz & H. Lingertat, (1997). Luminescence Properties of Ce-activated YAG Optical Ceramic Scintillator Materials. *Journal of Luminescence*, 75 (3), 193-203.
22. B. D. Bartolo, (1968). *Optical Interactions in Solids*. New York: Wiley.
23. R. C. Powell & G. Blasse, (1980). Energy Transfer in Concentrated Systems. *Structure and Bonding*, 42, 43-96.
24. K. B. Eisenthal & S. Siegel, (1964). Influence of Resonance Transfer on Luminescence Decay. *Journal of Chemical Physics*, 41 (3), 652-655.
25. G. Blasse, (1968). Energy Transfer in Oxidic Phosphors. *Physics Letters A*, 28 (6), 444-445.
26. A. A. Setlur, W. J. Heward, Y. Gao, A. M. Srivastava, R. G. Chandran & M. V. Shankar, (2006). Crystal Chemistry and Luminescence of Ce^{3+}-doped $(LuCaMg_2)Ca_2(Si, Ge)_3O_{12}$ and Its Use in LED Based Lighting. *Chemistry of Materials*, 18 (14), 3314-3322.
27. J. H. Zhang, H. B. Liang & Q. Su, (2009). Luminescence of Ce^{3+}-doped $Sr_{10}(PO_4)_6S$ Phosphors. *Journal of Physics D*, 42 (10) 105110.
28. Q. Zeng, H. B. Liang, G. B. Zhang, M. D. Birowosuto, Z. F. Tian, H. H. Lin, Y. B. Fu, P. Dorenbos & Q. Su, (2006). Luminescence of Ce^{3+} Activated Fluoro-apatites $M_5(PO_4)_3F$ (M = Ca, Sr, Ba) under VUV-UV and X-ray Excitation. *Journal of Physics-Condensed Matter*, 18 (42), 9549-9560.
29. J. H. Zhang, H. B. Liang, R. J. Yu, H. B. Yuan & Q. Su, (2009). Luminescence of Ce^{3+}-activated Chalcogenide Apatites $Ca_{10}(PO_4)_6Y$ (Y = S, Se). *Materials Chemistry and Physics*, 114 (1), 242-246.
30. L. Pidol, A. Kahn-Harari, B. Viana, B. Ferrand, P. Dorenbos, J. T. M. de Haas, C. W. E. van Eijk & E. Virey, (2003). Scintillation Properties of $Lu_2Si_2O_7:Ce^{3+}$, a Fast and Efficient Scintillator Crystal. *Journal of Physics-Condensed Matter*, 15, 2091-2102.
31. J. A. Mares, M. Nikl, J. Chval, I. Dafinei, P. Lecoq & J. Kvapil, (1995). Fluorescence and Scintillation Properties of $LuAlO_3$:Ce crystal. *Chemical Physics Letters*, 241, 311-316.
32. J. A. Mares, A. Beitlerova, M. Nikl, N. Solovieva, C. D'Ambrosio, K. Blazek, P. Maly, K. Nejezchleb & F. de Notaristefani, (2004). Scintillation Response of Ce-doped or Intrinsic Scintillating Crystals in the Range up to 1 Mev. *Radiation Measurements*, 38, 353-357.
33. M. Nikl, J. Hlinka, E. Mihokova, K. Polak & G. P. Pazzi, (1993). Decay Kinetics of CsI:Tl Luminescence Excited in the A-absorption Band. *Philosophical Magazine B*, 67, 627-649.

Chapter 7 Conclusions and future work

7.1 Conclusions

1. Pure $Sr_2Y_8(SiO_4)_6O_2$ powder has been synthesized by both solid state reaction and sol-gel method. In the solid state reaction, the starting materials play an important role in the purity of the final products. Homogeneous nano-sized Y_2O_3 powders obtained from the precipitation method demonstrate high reactivity and are helpful to synthesize pure $Sr_2Y_8(SiO_4)_6O_2$ powder materials. In the sol-gel method, the amount of water added to dissolve the reactants is crucial. Experimental results showed that 6 ml H_2O is an appropriate amount to synthesize pure $Sr_2Y_8(SiO_4)_6O_2$ materials. Less water is unable to dissolve the reactants and more water would induce impurities in the final product, probably due to the prevention of the condensation process.

2. The crystal structure of $Sr_2Y_8(SiO_4)_6O_2$ has been characterized. The symmetry of $Sr_2Y_8(SiO_4)_6O_2$ is $P6_3/m$ and the lattice constants $a = b = 9.3884$ Å, and $c = 6.8657$ Å. Half of A^I sites are occupied by Sr^{2+} while the other half of A^I sites and all the A^{II} sites are filled by Y^{3+}. The twist angle φ of this apatite is 25.04 °, and its structure is constructed by Si−O, A^I−O and A^{II}−O polyhedra. In each A^{II}−O polyhedron, there is a special oxygen atom called free oxygen O4, which is considerably underbonded.

3. Crystallographic features of the $Sr_2Y_8(SiO_4)_6O_2$ as well as other silicate oxyapatites are compared and summarized. A new parameter called effective ionic radius is introduced, which is able to distinguish different crystallographic sites. The lattice constants of each silicate oxyapatite group vary linearly with the effective ionic radius of A^I and A^{II} sites. The twist angles also exhibit linear relationship with respect to the effective ionic radius and larger ionic size results in smaller twist angle.

4. By using similar sol-gel process as synthesis of pure $Sr_2Y_8(SiO_4)_6O_2$, pure europium doped silicate oxyapatites $Sr_2Y_{8-x}Eu_x(SiO_4)_6O_2$ are synthesized. The XRD and Rietveld

refinement reveal that most Eu^{3+} cations enter A^{I} site in low europium concentration (x = 0~0.5). As the Eu^{3+} concentration increases (x > 0.5), Eu^{3+} also occupy A^{II} site but the preference to the A^{I} site is still maintained. As the increase of the europium concentration, the average bond length in A^{II}–O polyhedron and the bond length of A^{II}–O4 are elongated, but the average bond length in A^{I}–O polyhedron becomes smaller.

5. The photoluminescent properties are closely related to the crystal structures. Cationic sites with no inversion center result in intense emission of the $^5D_0$–$^7F_2$ transition. As Eu^{3+} enters A^{II} sites in higher doping concentration, the free oxygen O4 linking to the A^{II} site induces the shifting of CTB bands and relaxation of parity selection rule which leads to effective excitation of the $^7F_0$–$^5L_6$ transition at 393 nm. Moreover, the analysis of the $^5D_0$–$^7F_0$ transition confirms that Eu^{3+} occupies two different cationic sites in relative higher Eu^{3+} concentration.

6. $Sr_2Y_6Eu_2(SiO_4)_6O_2$ appears to be the one with the highest emission intensity. Further increase of the europium content leads to the concentration quenching. Comparison between the samples from solid state reaction and sol-gel method indicates that the sol-gel method is able to achieve more homogeneous microstructure with higher light output. The emission intensity of $Sr_2Y_6Eu_2(SiO_4)_6O_2$ excited at 393 nm is comparable to commercial fluorescent lamp phosphor Eu:Y_2O_3. The CIE coordinates for $Sr_2Y_6Eu_2(SiO_4)_6O_2$ are (0.63, 0.37) which is close to the pure red color. Therefore, the compounds Eu^{3+} doped $Sr_2Y_8(SiO_4)_6O_2$ is a promising red phosphor for the white LEDs.

7. The translucent silicate oxyapatite $Sr_2Y_8(SiO_4)_6O_2$ ceramic is successfully fabricated by employing the spark plasma sintering. The completely and incompletely condensed ceramic samples sintered by SPS are investigated. The densification process does not complete in the opaque ceramic sintered at 1400 °C. The ceramic sintered at 1500 °C is densified and appears translucent with the porosity as low as 0.7%. The total forward transmittance is about 52% but the in-line transmittance is much lower due to the

scattering effect of the residual pores and the birefringence. More quantitative calculation reveals that influence of residual pores on the in-line transmittance is more significant than that of the birefringence effect.

8. The translucent Ce^{3+} doped $Sr_2Y_8(SiO_4)_6O_2$ ceramics with different Ce^{3+} concentration has been fabricated by spark plasma sintering. Based on the analysis of the photoluminescence spectra, Ce^{3+} cations occupy two different sites A^I and A^{II} in $Sr_2Y_8(SiO_4)_6O_2$ crystal structure with the site preference to A^I. The different coordination environments of Ce^{3+} result in different photoluminescence features in the spectra. The energy levels of Ce^{3+}(I) and Ce^{3+}(II) are constructed by configurational coordinate model.

9. The energy transfer from Ce^{3+}(I) to Ce^{3+}(II) is revealed. It is an electric-dipole interaction, which is faster in the ceramic with higher Ce^{3+} doping concentration due to the higher acceptor population density. By quantitatively analysis of the decay curves, the radiative decay time for Ce^{3+}(I) derived from the global fitting turns out to be 31.6 ns and the energy transfer rates with different Ce^{3+} concentrations are also obtained. The Ce^{3+}(I)→Ce^{3+}(II) energy transfer rate in $Sr_2Y_{7.9}Ce_{0.1}(SiO_4)_6O_2$ is about four times higher than that in $Sr_2Y_{7.95}Ce_{0.05}(SiO_4)_6O_2$. The mean decay times for these ceramics apatite with different Ce^{3+} doping concentrations is in the range of 11.9 to13.5 ns when the emission is monitored at 370 nm.

7.2 Future work

Based on the results of present studies, some future work is proposed to further study the optical applications for silicate oxyapatite.

Firstly, since Eu^{3+} doped $Sr_2Y_8(SiO_4)_6O_2$ powders show potential as a red phosphor in white LED application, it will be of great interest to fabricate white LED devices based on near UV emission LED chips such as InGaN. This silicate oxyapatite red phosphor

with commercial blue (e.g. Eu^{2+}:$BaMgAl_{10}O_{17}$) and green (e.g. Cu^{+}/Al^{3+}:ZnS) phosphors will be coated on the LED chips followed by packaging. By varying the ratio between the three kinds of phosphors, the LED performance such as the luminous efficiency, color render and color temperature can be investigated and optimized.

As for the translucent ceramic fabrication, the results indicate that the light scattering effect by the residual pores is still considerable. Therefore, further elimination of the pores will be helpful to improve the light transmittance of the samples. Other advanced sintering techniques such as hot isostatic press and high vacuum sintering can be tried to achieve this purpose. Transparent ceramics such as YAG[1] have been fabricated in the way that raw powders are firstly vacuum sintered into a pellet with relative high density and then hot isostatic pressed to further minimize the porosity. Hence, hot isostatic press may be a suitable tool and the ceramics obtained from spark plasma sintering might be further condensed by a subsequent hot isostatic press. Moreover, the birefringence effect would be reduced by magnetic field assisted slip casting followed by sintering processes, as demonstrated in the fabrication of high transmittance Al_2O_3 ceramics,[2] which is also worth to try for the silicate oxyapatite ceramics.

Furthermore, the behaviors of the Ce^{3+} doped silicate oxyapatite ceramics under high energy irradiation such as gamma-ray can be studied by the spectra and the decay curves. The energy absorption and conversion is complicated under high energy irradiation. Therefore, the fundamental understandings of these processes are meaningful in both the theoretical physics explorations and the device development such as scintillators.

1. S. H. Lee, E. R. Kupp, A. J. Stevenson, J. M. Anderson, G. L. Messing, X. Li, E. C. Dickey, J. Q. Dumm, V. K. Simonaitis-Castillo & G. J. Quarles, (2009). Hot Isostatic Pressing of Transparent Nd:YAG Ceramics. *Journal of the American Ceramic Society*, 92 (7), 1456-1463.

2. X. J. Mao, S. W. Wang, S. Shimai & J. K. Guo, (2008). Transparent Polycrystalline Alumina Ceramics with Orientated Optical Axes. *Journal of the American Ceramic Society*, 91 (10), 3431-3433.

Publication List:

[1] **Shen, Y. Q.**; Tok, A.; Dong, Z. L.* Synthesis and Crystal Structure Characterization of Silicate Apatite $Sr_2Y_8(SiO_4)_6O_2$, ***Journal of the American Ceramic Society***, 2010, 93(4), 1176-1182.

[2] **Shen, Y. Q.**; Xu, J. L.; Tok, A; Tang, D. Y.; Khor, K. A.; Dong, Z. L.* Development of Translucent Oxyaptite Ceramics by Spark-plasma Sintering, ***Journal of the American Ceramic Society***, 2010, 93(10), 3060-3063.

[3] **Shen, Y. Q.**; Chen, R.; Xiao, F.; Sun, H. D.; Tok, A.; Dong, Z. L.* Study of the Cation Distributions in Eu Doped $Sr_2Y_8(SiO_4)_6O_2$ by X-ray Diffraction and Photoluminescent Spectra, ***Journal of Solid State Chemistry***, 2010, 183(12), 3093-3099

[4] **Shen, Y. Q.**; Chen, R.; Gurzadyan, G. G.; Xu, J. L.; Sun, H. D.; Khor, K. A.; Dong, Z. L.* Crystal Structures, Photoluminescence and Energy Transfer in Ce^{3+} Doped $Sr_2Y_8(SiO_4)_6O_2$ Translucent Ceramics, ***Optical Materials***, 2012, 34, 1155-1160.

[5] **Shen, Y. Q.**; Lian, J.; Dong, Z. L. * Prediction and Analysis of the 5*d*-state Energies of Ce^{3+} in Multiple Cationic Sites , submitted

[6] Chen, R.; **Shen, Y. Q.**; Xiao, F.; Gurzadyan, G. G.; Dong, Z. L.; Sun, X. W.; Sun, H. D.* Surface Eu-treated ZnO nanowires with efficient red emission, ***Journal of Physical Chemistry C***, 2010, 114, 18081-18084

[7] Xiao, F.; Chen, R.; **Shen, Y. Q.**; Liu, B.; Gurzadyan, G. G.; Dong, Z. L.; Zhang, Q. Y. * ; Sun, H. D.* Infrared Emission Properties and Energy Transfer in ZnO-SiO_2:Yb^{3+} Composites, ***Journal of Alloys and Compounds***, 2011, 509, 7794-7797.

[8] Guo, C. X.; Sheng, Z. M.; **Shen, Y. Q.**; Dong, Z. L.; Li, C. M.* Thin-Walled Graphitic Nanocages As a Unique Platform for Amperometric Glucose Biosensor, ***ACS Applied Materials & Interface***, 2010, 2 (9), 2481-2484.

[9] Wang, H. T.; Wu, J. C.; **Shen, Y. Q.**; Li, G. P.; Zhang, Z.; Xing, G. Z.; Guo, D. L.; Wang, D. D.; Dong, Z. L.; Wu, T.* $CrSi_2$ Hexagonal Nanowebs, ***Journal of the American Chemistry Society***, 2010, 192, 15975-15977.

[10] Ling, B.; Sun, S. W.* ; **Shen, Y. Q.**; Dong. Z. L. Hierarchical ZnO/Bi_2O_3 Nanostructures: Synthesis, Characterization, and Electron-beam Modification. ***Applied Physica A***, 2010, 98(1), 91-96.

[11] Sun, X. W.*; Ling, B.; Zhang, J. L.; Tan, S. T.; Yang, Y.; **Shen, Y. Q.**; Dong, Z. L.; Li, X. C. Ultraviolet Emission from a ZnO Rod Homojunction Light-emitting Diode, ***Applied Physics Letters***, 2010, 95(13), 133124-133126.

[12] Ling, B.; Sun, X. W.* ; Zhao, J. L.; **Shen, Y. Q.**; Dong, Z. L.; Sun, L. D.; Li, S. F.; Zhang, S. One-dimensional Single-crystalline Bismuth Oxide Micro/nanoribbons: Morphology-controlled Synthesis and Luminescent Propeties, ***Journal of Nanoscience and Nanotechnology***, 2010, 10(12), 8322-8327.